VERLAG DER TECHNISCHEN UNIVERSITÄT GRAZ

Douglas Ramalho Queiroz Pacheco

Stable and stabilised finite element methods for incompressible flows of generalised Newtonian fluids

CES 42

MONOGRAPHIC SERIES TU GRAZ
COMPUTATION IN ENGINEERING AND SCIENCE

Douglas Ramalho Queiroz Pacheco

Stable and stabilised finite element methods for incompressible flows of generalised Newtonian fluids

Monographic Series TU Graz

Computation in Engineering and Science

Monographic Series TU Graz

Computation in Engineering and Science Volume 42

Douglas Ramalho Queiroz Pacheco

Stable and stabilised finite element methods for incompressible flows of generalised Newtonian fluids

---

This work is based on the dissertation *"Stable and stabilised finite element methods for incompressible flows of generalised Newtonian fluids"*, presented at Graz University of Technology, Institute of Applied Mathematics in 2021.

Supervision / Assessment:

Olaf Steinbach (Graz University of Technology)
Gert Lube (Georg-August-Universität Göttingen)
Marek Behr (RWTH Aachen University)

Cover photo	Vier-Spezies-Rechenmaschine by courtesy of the Gottfried Wilhelm Leibniz Bibliothek – Niedersächsische Landesbibliothek Hannover
Cover layout	Verlag der Technischen Universität Graz
Print	DATAFORM Media Ges.m.b.H.

www.tugraz-verlag.at

Print
ISBN 978-3-85125-856-1

E-Book
ISBN 978-3-85125-857-8
DOI 10.3217/978-3-85125-856-1

Abstract

Many viscous materials of engineering, geophysical or biomedical interest can be accurately modelled as generalised Newtonian fluids, that is, with an apparent viscosity depending locally on the flow field. A few examples are polymer melts, dense granular materials and blood under certain flow regimes. Although these so-called quasi-Newtonian models may appear simple, their simulation imposes various challenges ranging from quite basic aspects such as boundary conditions, to more technical ones involving solver accuracy and efficiency. The focus of this work is to develop finite element methods for the accurate, efficient and reliable simulation of incompressible flows involving generalised Newtonian fluids – a class which also includes, of course, the Newtonian case. Within that field, our scope is rather broad, addressing topics that go from enforcing outflow boundary conditions to eliminating numerical artifacts; from flow simulations to inverse problems; from efficient time-stepping to parallelisable space-time solvers; from stable to stabilised finite element methods.

Our main contribution is devising a quasi-Newtonian finite element framework that can naturally enforce open boundary conditions, allows equal-order velocity-pressure pairs and eliminates the spurious pressure boundary layers typically arising from low-order discretisations. To accomplish that, we first devise a non-Newtonian version of an inverse technique typically used for estimating arterial pressure from hemodynamic velocities. We then insert this discrete velocity-pressure operator into the incompressible Navier–Stokes equations to consistently break their saddle-point structure. The resulting stabilisation method is assessed through extensive numerical testing, which confirms its improved accuracy with respect to classical methods.

Then, shifting the focus from the formulation to the solution process, we introduce two main contributions. The first is a family of split-step schemes consistently decoupling velocity and pressure into a series of scalar advection-diffusion, Poisson and mass matrix problems. These schemes are fairly similar to so-called projection or pressure-correction methods, but allow equal-order spaces without inducing artificial pressure boundary conditions. Finally, we present a space-time finite element tearing and interconnecting method to decompose the space-time domain and yield smaller, easily parallelisable subproblems.

It must be mentioned that this work is application-motivated, yet technique-driven. We have practical biomedical and engineering challenges as our main motivation, but the present focus lies on developing and testing advanced numerical methods. Although the

reader will not find, for instance, patient-specific simulations herein, most of our techniques are immediately applicable not only to such scenarios, but also to industrially relevant problems where complex Newtonian and non-Newtonian flows often feature.

Kurzfassung

Eine Vielzahl an viskosen Materialien in den Ingenieurwissenschaften, der Geophysik oder in der Biomedizin können als generalisierte Newtonsche Fluide modelliert werden. Diese Fluidmodelle berücksichtigen eine variable Viskosität abhängig von dem Strömungsfeld, eine Abhängigkeit, die beispielsweise bei Schmelzen von Polymeren, dichten granularen Materialien oder Blut unter bestimmten Strömungsbedingungen von zentraler Bedeutung ist. Obwohl diese sogenannten quasi-Newtonschen Modelle einfach erscheinen, ist deren numerische Erfassung mit einigen Schwierigkeiten verbunden, reichend von grundlegenderen Aspekten wie der Berücksichtigung von Randbedingungen zu komplexeren Problemstellungen im Zusammenhang mit Genauigkeit und Effizienz der Lösungsalgorithmen. Der Fokus dieser Arbeit liegt in der Entwicklung von Finite Elemente Methoden für die genaue, effiziente und zuverlässige Simulation inkompressibler Strömungen mit generalisierten Newtonschen Fluiden – eine Klasse von Fluiden, die den Newtonschen Fall mitberücksichtigt. In diesem Kontext ist das Spektrum an behandelten Themen breit gefächert. Die Betrachtungen befassen sich mit der Behandlung von Ausflussrandbedingungen bis zur Elimination von numerischen Artefakten; von der Strömungssimulation bis zu inversen Problemstellungen; von effizienten Zeitschrittverfahren zu parallelisierbaren Raum-Zeit Lösern; von stabilen zu stabilisierten Finite Elemente Methoden.

Der Hauptbeitrag ist die Herleitung eines quasi-Newtonschen Finite Elemente Lösers, der natürliche Ausflussrandbedingungen erzwingt, Interpolation gleicher Ordnung der involvierten Variablen erlaubt und künstliche Druckrandschichten eliminiert, die typischerweise bei Diskretisierung mit Elementen niedriger Ordnung auftreten. Um dies zu erreichen, wird zuerst eine nicht-Newtonsche Version eines inversen Verfahrens entwickelt, das typischerweise zur Berechnung des arteriellen Drucks basierend auf der Geschwindigkeit des Blutstromes verwendet wird. Dieser diskrete Operator wird anschließend in die inkompressiblen Navier–Stokes Gleichungen eingesetzt, um die Sattelpunktstruktur konsistent aufzulösen. Die resultierende Stabilisierung wird rigorosen numerischen Tests unterzogen, welche die verbesserte Genauigkeit mit klassischen Methoden zeigen.

In weiterer Folge wird der Fokus von der Finite Elemente Formulierung hin zum Lösungsprozess gelenkt, wo zwei Hauptbeiträge zu identifizieren sind: Erstens wird eine Familie von sogenannten split-step Methoden eingeführt, die Geschwindigkeit und Druck konsistent in eine Reihe von skalaren Advektions-Diffusions, Poisson und Masse-Matrix Problemen entkoppeln. Diese entwickelten Schemata sind Projektions- oder pressure-correction Methoden ähnlich, erlauben jedoch die Verwendung von Polynomialräumen selber Ordnung ohne künstliche Druckrandbedingungen hervorzurufen. Zweitens wird eine Raum-

Zeit tearing and interconnecting Finite Elemente Methode entwickelt, um das Raum-Zeit Gebiet in kleinere, leicht parallelisierbare Unterprobleme zu teilen.

An dieser Stelle ist zu betonen, dass die vorliegende Arbeit grundsätzlich durch Anwendungen motiviert ist, aber den Fokus auf numerische Techniken richtet. Demnach werden fortschrittliche Numerische Methoden entwickelt und getestet, deren Design durch Herausforderungen in der praktischen Anwendung motiviert ist. Obwohl der geschätzte Leser beispielsweise keine Patienten-spezifischen Simulationen finden wird, sind die meisten der vorgestellten Techniken und Algorithmen nicht nur auf solche, sondern auch auf relevante Problemstellungen aus der Industrie, wo komplexe Newtonsche und nicht-Newtonsche Strömungen oft auftreten, direkt anwendbar.

CONTENTS

1 INTRODUCTION

Many viscous materials may be perceived as simple fluids to the naked eye, while actually having much more complex composition and mechanical behaviour. Blood, for example, is not simply a liquid, but an organic tissue consisting of living and non-living components immersed in a liquid matrix. Therefore, modelling hemodynamic behaviour mathematically is by no means a trivial task. In most healthy arteries, blood flows basically as a Newtonian fluid with constant effective viscosity and density, whereas non-Newtonian effects such as shear thinning and viscoelasticity can play a major role in low-shear regions around stenoses and aneurysms [1]. In the presence of abnormalities in either blood composition or vascular morphology, it is often necessary to consider biochemical phenomena such as coagulation. In capillary vessels whose diameter is comparable to the dimensions of erythrocytes (red blood cells), even the single-phase-continuum assumption may no longer hold. Yet, as relevant and rewarding as constitutive modelling is, we herein direct our attention to another side of the mathematical problem: given the set of equations arising from a fluid model, how can we solve them accurately and efficiently? In particular, this work is dedicated to developing advanced finite element methods for incompressible flow problems, especially those involving non-Newtonian models of engineering and biomedical interest.

The non-Newtonian behaviour most frequently observed in hemodynamic or polymeric flows is shear thinning, characterised by decreasing viscosity in the presence of increasing shear rates. In blood, this is mostly due to the three-dimensional structures formed by the aggregation of red blood cells [1]. Since these structures can take several seconds to form and cannot withstand high shear rates, this non-Newtonian response is seen mainly in flow regions experiencing long-term low shear rates [2]. Also for this reason, viscoelasticity is not observed in most hemodynamic regimes [1, 3], since it is only significant in areas with enough aggregated erythrocytes to store a reasonable amount of elastic energy. Because such regions are quite scarce, and also due to the high computational cost related to viscoelastic flow simulations, Newtonian and quasi-Newtonian models are much more common in computational hemodynamics, and we also stick to these in the present work.

Generalised Newtonian models, often called quasi-Newtonian, allow for local variations of an *effective* or *apparent* viscosity, depending usually on shear rate levels. This approach can account for important non-Newtonian phenomena such as shear thinning and plug flow, while maintaining a similar mathematical and computational framework as used for

Newtonian fluids. Furthermore, several simple models provide excellent fits to experimental data [1, 4]. Such generalised models are used not only in hemodynamics, but also in polymeric flow simulations of industrial interest. Because both fields are highly applied, and also due to the apparent similarity between Newtonian and quasi-Newtonian equations, one is usually tempted to try using standard numerical methods originally conceived for Newtonian fluids. Although this is sometimes possible, it is usually not the ideal approach – neither physically nor mathematically. Yet, before commenting on the limitations of existing methods, we must briefly outline some typical numerical issues encountered in incompressible flow problems.

When employing Galerkin finite element methods for the simulation of incompressible flows, one must be careful in the selection of the approximation spaces for velocity and pressure. Using the same polynomial order for both spaces, for instance, violates the famous Ladyzhenskaya–Babuška–Brezzi (LBB) condition, thereby rendering the discretisation unstable. However, since the findings of Hughes, Franca and co-workers four decades ago [5, 6], it has become standard to employ stabilisation techniques to circumvent the LBB condition and allow equal-order shape functions for all unknowns. Such Petrov–Galerkin-like stabilisation methods are usually built upon relaxed incompressibility equations devised under classical Newtonian assumptions. Probably for that reason, the use of LBB-compatible finite elements is somewhat more frequent in the literature for quasi-Newtonian fluids [7–16]. Although such compatible spaces offer an ideal setting from a mathematical standpoint, combining stability and optimal convergence, they are not always a viable option. In particular, there is great practical appeal in the use of first-order elements, especially in the biomedical context. The main reasons are the simplicity in meshing, data structure and implementation, and the fact that patient-specific geometries are typically obtained from voxelated medical images leading to a first-order boundary description. Moreover, while higher-order methods are known to perform better for under-resolved flows [17, 18], the low-Reynolds, widely laminar flows typically encountered in hemodynamics can be satisfactorily handled by low-order elements.

Some stabilisation methods are based solely on pressure and can therefore be applied to generalised Newtonian problems rather straightforwardly. The most popular of them is probably the penalty method, which consists of relaxing incompressibility to decouple velocity and pressure. Despite being used quite often for quasi-Newtonian fluids [19–22], this approach was shown by Sobhani et al. [19] to attain poor pressure approximations, even when using higher-order elements. The pressure Poisson stabilisation of Brezzi and Pitkäranta [23] was reported by Knauf et al. [24] to also perform poorly in practice. The pressure projection method by Dohrmann and Bochev [25] was employed successfully by John et al. [26] and seems to be a good alternative. Time-related methods which can be applied straightforwardly to the quasi-Newtonian case are artificial compressibility [27, 28] and non-incremental fractional-step methods [29, 30]. Although residual-based stabilisations such as pressure-stabilised Petrov–Galerkin (PSPG) and variational multi-scale

(VMS) methods can also be used [31–33], their loss of consistency for linear elements can yield inaccurate results, as we shall discuss later on.

To the best of our knowledge, there are very few works in the literature dedicated to designing stabilisation techniques for generalised Newtonian problems. Some of them require introducing the viscous stress as an additional tensor-valued unknown [34, 35], resulting in prohibitive computational costs in practical scenarios. The VMS formulation proposed by Masud and Kwack [36] offers a viable alternative, but – as all residual-based stabilisations – can suffer from spurious pressure boundary layers and poor mass conservation in the low-order case. In this context, this work has, as its main contribution, the design of a new residual-based framework intended especially – but not exclusively – for low-order finite element approximations of incompressible generalised Newtonian flow problems. We aim to solve two inherent issues of standard methods: the loss of consistency when using linear elements and the arising of inappropriate natural boundary conditions for truncated domains. In doing so, we end up achieving relevant improvements in robustness and accuracy with respect to state-of-the-art residual-based stabilisations, not only for the non-Newtonian case, but also for the standard incompressible Navier–Stokes problem.

In the field of stable – rather than *stabilised* – methods, our main contribution is a continuous, mixed space-time finite element framework. The space-time approach handles time as an additional spatial coordinate and therefore allows for local-in-space temporal resolution, which is not possible in traditional time-stepping methods [37, 38]. It also provides a natural framework for efficient adaptivity and parallelisation in both space and time [39]. To further improve efficiency, we present a finite element tearing and interconnecting (FETI) method using direct solvers for the subproblems, while relying on an iterative solution of the global (interface) problem.

The first part of this dissertation focus on formulation aspects. In particular, on how to treat the troublesome viscous term in mixed and stabilised variational problems in order to yield physically and mathematically consistent formulations. In Chapter 2 we introduce useful concepts and notation, while Chapter 3 presents the equations we will be dealing with, in strong and weak forms. Also there we discuss common issues with outflow boundary conditions in internal flows, and present a formulation dealing with those shortcomings. The LBB-stable finite element discretisation of this and classical formulations is the topic of Chapter 4. In Chapter 5 we introduce a technique that can be used for imaging-based arterial pressure reconstruction, as well as for stabilisation of equal-order finite element solvers. Then, our sixth and longest chapter deals with stabilised equal-order methods, comparing our new techniques with classical ones and showcasing our improvements.

Until Chapter 6, we deliberately limit the discussion to stationary problems, simply for concision and because the transient terms play no role in the issues tackled there. Then, in Chapters 7 and 8 we turn our attention to the efficient solution of the time-dependent problem. More precisely, we introduce two very distinct approaches to solve the rather complex system of partial differential equations at hand. The first one is a split-step framework that

efficiently decouples the computation of pressure, velocity and viscosity into simple Poisson and heat-like problems. The second approach consists of a domain-decomposition-based space-time framework offering great flexibility in discretisation, adaptivity and parallelisation. Finally, in Chapter 9 we discuss open questions and outline the future directions that can be taken from here.

2 PRELIMINARIES

2.1 Basic definitions

We start by introducing some mathematical definitions and notations that will be used throughout this work. Let $\boldsymbol{u}$ and $\boldsymbol{x}$ be vectors in $\mathbb{R}^d$, $d = 2$ or 3 being the number of spatial dimensions considered. Four spatial differential operators will be used frequently: the gradient, divergence, curl and Laplacian of $\boldsymbol{u}$ will be denoted, respectively, by $\nabla \boldsymbol{u}$, $\nabla \cdot \boldsymbol{u}$, $\nabla \times \boldsymbol{u}$ and $\Delta \boldsymbol{u}$. The divergence is a scalar defined as

$$\nabla \cdot \boldsymbol{u} := \sum_{i=1}^{d} \frac{\partial u_i}{\partial x_i}, \tag{2.1}$$

where u_i denotes the i-th component of $\boldsymbol{u}$, and analogously for x_i. The curl is defined as a scalar for $d = 2$ and an $\mathbb{R}^3$ vector for $d = 3$:

$$\nabla \times \boldsymbol{u} := \begin{cases} \frac{\partial u_2}{\partial x_1} - \frac{\partial u_1}{\partial x_2}, & \text{if } d = 2, \\ \left(\frac{\partial u_3}{\partial x_2} - \frac{\partial u_2}{\partial x_3}, \frac{\partial u_1}{\partial x_3} - \frac{\partial u_3}{\partial x_1}, \frac{\partial u_2}{\partial x_1} - \frac{\partial u_1}{\partial x_2} \right)^\top, & \text{if } d = 3. \end{cases} \tag{2.2}$$

The spatial gradient of $\boldsymbol{u}$ is a second-order tensor in $\mathbb{R}^{d \times d}$ whose components are defined as

$$(\nabla \boldsymbol{u})_{ij} := \frac{\partial u_i}{\partial x_j}. \tag{2.3}$$

Mind that an alternative definition swapping the indices i and j is sometimes found in the literature. The symmetric gradient is then defined as

$$\nabla^s \boldsymbol{u} := \frac{1}{2} \left[\nabla \boldsymbol{u} + (\nabla \boldsymbol{u})^\top \right]. \tag{2.4}$$

The Laplacian of $\boldsymbol{u}$ is a vector in which the i-th component is the (scalar) Laplacian of u_i, that is,

$$\begin{aligned} \Delta \boldsymbol{u} &:= (\Delta u_1, \ldots, \Delta u_d)^\top \\ &= (\nabla \cdot \nabla u_1, \ldots, \nabla \cdot \nabla u_d)^\top \\ &\equiv \nabla (\nabla \cdot \boldsymbol{u}) - \nabla \times (\nabla \times \boldsymbol{u}). \end{aligned} \tag{2.5}$$

Notice that in two dimensions the curl-curl operator has the form

$$\nabla \times (\nabla \times \boldsymbol{u}) := \begin{pmatrix} \frac{\partial^2 u_2}{\partial x_1 \partial x_2} - \frac{\partial^2 u_1}{\partial x_2^2} \\ \frac{\partial^2 u_1}{\partial x_1 \partial x_2} - \frac{\partial^2 u_2}{\partial x_1^2} \end{pmatrix}. \tag{2.6}$$

In time-dependent problems, we shall further denote by $\partial_t \boldsymbol{u}$ the partial derivative of $\boldsymbol{u}$ with respect to time, t. The dyadic (or outer) product between two vectors $\boldsymbol{u}$ and $\boldsymbol{v}$ is the second-order tensor $\boldsymbol{u} \otimes \boldsymbol{v}$, and $|\cdot|$ denotes the Euclidian norm of a scalar, vector or second-order tensor. Considering a connected domain $\Omega \subset \mathbb{R}^d$ with Lipschitz boundary $\Gamma := \partial\Omega$, we denote by $\langle \cdot,\cdot \rangle_{L^2(\Omega)}$ and $\langle \cdot,\cdot \rangle_\Omega$ the $L^2(\Omega)$ inner product and duality pairing, respectively, and analogously for Γ.

2.2 Finite element discretisation

For the domain Ω, let us consider a sequence of admissible decompositions Ω_h into N_e shape-regular, non-overlapping elements Ω_e, such that

$$\overline{\Omega_h} = \bigcup_{e=1}^{N_e} \overline{\Omega_e} \, .$$

When using standard low-order finite element geometries, only polygonal/polyhedral domains will be exactly represented by Ω_h; in general, Ω_h will be an approximation of Ω, with $\partial\Omega_h$ being a piecewise polynomial interpolation of $\partial\Omega$. The element size is defined as $h_e := |\Omega_e|^{1/d}$, with $|\Omega_e|$ denoting the measure (area in two dimensions, volume in three) of Ω_e, while $h := \max\{h_e\}$. For a mesh consisting of simplicial elements (triangles for $d = 2$ or tetrahedra for $d = 3$), we denote by $S_h^m(\Omega_h)$ the space of continuous Lagrangian basis functions of degree m in Ω_h, i.e.,

$$S_h^m(\Omega_h) := \left\{ q_h \in C^0\left(\overline{\Omega_h}\right) \, : \, q_h|_{\Omega_e} \in \mathcal{P}_m(\Omega_e), \forall\, \Omega_e \subset \Omega_h \right\}, \tag{2.7}$$

where $\mathcal{P}_m(\Omega_e)$ is the space of polynomials of degree m in Ω_e. As usual, Lagrangian basis functions have the Kronecker property, i.e., each function ψ_i takes value 1 on node i, and 0 on the other nodes. Note that for $m = 0$ we relax the global C^0 continuity assumption so as to have the space of piecewise constants: each basis function ψ_e takes value 1 inside Ω_e, and 0 elsewhere.

When tackling incompressible flow problems, our main unknowns will be the velocity $\boldsymbol{u}$ and the pressure p, whose finite element approximations will be denoted by $\boldsymbol{u}_h$ and p_h, respectively – not necessarily in the same finite element spaces. We will denote by $P_m P_n$ the simplicial finite elements with $(\boldsymbol{u}_h, p_h) \in [S_h^m(\Omega_h)]^d \times S_h^n(\Omega_h)$. Similarly, $Q_m Q_n$ denotes the finite element pairs defined on tensor-product-based isoparametric elements (quadrilaterals for $d = 2$ and hexahedra for $d = 3$). Of course, given a time interval $t \in (0,T)$, the finite element spaces can be straightforwardly extended to the space-time setting, with a suitable triangulation Q_h of the space-time domain $\mathrm{Q} := \Omega \times (0,T)$.

In problems with known analytical solution, the estimated orders of convergence (eoc) will be in most cases measured through a normalised L^2 norm:

$$\|\boldsymbol{v} - \boldsymbol{v}_h\|_0 := \frac{\|\boldsymbol{v} - \boldsymbol{v}_h\|_{L^2(D)}}{\|\boldsymbol{u}\|_{L^2(D)}}, \tag{2.8}$$

where $D = \Omega$ for stationary problems and $D = \mathrm{Q}$ in the space-time context.

3 STRONG AND VARIATIONAL PROBLEMS

3.1 Problem statement

Let us consider a splitting of the boundary Γ into two non-overlapping parts Γ_D and Γ_N. In the most general case where both convective and diffusive nonlinearities are allowed, the incompressible Navier–Stokes system reads

$$\rho[\partial_t \boldsymbol{u} + (\nabla \boldsymbol{u})\boldsymbol{u}] - \nabla \cdot \mathbb{S} + \nabla p = \boldsymbol{f} \qquad \text{in } \Omega \times (0,T], \tag{3.1}$$

$$\nabla \cdot \boldsymbol{u} = 0 \qquad \text{in } \Omega \times (0,T], \tag{3.2}$$

$$\boldsymbol{u} = \boldsymbol{g} \qquad \text{on } \Gamma_D \times (0,T], \tag{3.3}$$

$$\mathbb{T}\boldsymbol{n} = \boldsymbol{h} \qquad \text{on } \Gamma_N \times (0,T], \tag{3.4}$$

$$\boldsymbol{u} = \boldsymbol{u}_0 \qquad \text{at } t = 0, \tag{3.5}$$

where ρ is the fluid's density, $\mathbb{S}$ is the viscous stress tensor, μ is the dynamic viscosity, $\boldsymbol{n}$ is the unit outward normal vector on Γ, and $\mathbb{T}$ can be either the full Cauchy stress tensor or a modified version, depending on the variational problem considered (*cf.* Section 3.4); the right-hand side vectors are given quantities. Equations (3.1) and (3.2) state, respectively, the balance of linear momentum and the conservation of mass (often called *continuity*). To close the system, we need a stress-strain relationship, which for a generalised Newtonian fluid is given by

$$\mathbb{S} = 2\mu \nabla^s \boldsymbol{u}\,. \tag{3.6}$$

The viscosity is most commonly modelled through a nonlinear dependence on the shear rate $\dot{\gamma} := \sqrt{2\nabla^s \boldsymbol{u} : \nabla^s \boldsymbol{u}}$ by a map $\eta : \mathbb{R}_+ \to \mathbb{R}_+ \setminus \{0\}$, that is,

$$\mu = \eta(\dot{\gamma}),$$

bounded below by zero and above by a finite value. Most rheological models of industrial and biomedical interest can be written in the generic form

$$\eta(\dot{\gamma}) = \eta_1 + \eta_2 \left[\kappa + (\lambda\dot{\gamma})^a\right]^b,$$

where $a, b, \kappa, \lambda, \eta_1, \eta_2$ are fitting parameters depending on rheological properties. The choice $\kappa = \eta_1 = 0$ gives the so-called power-law model, whereas $\kappa = 1$ leads to the Carreau–Yasuda model (or simply *Carreau model* when $a = 2$). The standard (Newtonian) Navier–Stokes equations have $\eta_2 = 0$ (so that $\nabla\mu \equiv \boldsymbol{0}$), and the linear Stokes system is recovered

by further dropping the nonlinear convective term $(\rho\nabla\boldsymbol{u})\boldsymbol{u}$. All these versions will be considered herein.

For the pure Dirichlet problem ($\Gamma_N = \emptyset$), two additional conditions are needed to guarantee unique solvability of the incompressible flow system. First, *solvability* requires that the Dirichlet datum (3.3) satisfy

$$\int_\Gamma \boldsymbol{n}\cdot\boldsymbol{g}\ \mathrm{d}\Gamma = 0\,,$$

which is needed for global conservation of mass, since

$$0 = \int_\Omega \nabla\cdot\boldsymbol{u}\ \mathrm{d}\Gamma = \int_\Gamma \boldsymbol{n}\cdot\boldsymbol{u}\ \mathrm{d}\Gamma = \int_\Gamma \boldsymbol{n}\cdot\boldsymbol{g}\ \mathrm{d}\Gamma\,.$$

For *uniqueness*, we must set a pressure scaling such as $\langle p,1\rangle_{L^2(\Omega)} = 0\ \forall\, t$ or $\langle p,1\rangle_\Gamma = 0\ \forall\, t$, as otherwise the pressure will only be defined up to an arbitrary function in time.

We shall for now stick to the stationary system:

$$(\rho\nabla\boldsymbol{u})\boldsymbol{u} - \nabla\cdot(2\mu\nabla^s\boldsymbol{u}) + \nabla p = \boldsymbol{f} \qquad \text{in } \Omega\,, \tag{3.7}$$

$$\nabla\cdot\boldsymbol{u} = 0 \qquad \text{in } \Omega\,, \tag{3.8}$$

$$\boldsymbol{u} = \boldsymbol{g} \qquad \text{on } \Gamma_D\,, \tag{3.9}$$

$$\mathbb{T}\boldsymbol{n} = \boldsymbol{h} \qquad \text{on } \Gamma_N\,, \tag{3.10}$$

since most of the issues we aim to discuss herein – and their corresponding solutions – are related to viscous and not inertial effects. Chapters 7 and 8 deal with the efficient solution of time-dependent problems.

3.2 Standard elasticity formulation

For the stationary problem, the standard variational formulation reads: for $\boldsymbol{f}\in[H_D^{-1}(\Omega)]^d$, find $(\boldsymbol{u},p)\in[H^1(\Omega)]^d\times L^2(\Omega)$, with $\boldsymbol{u}|_{\Gamma_D}=\boldsymbol{g}$, such that for all $(\boldsymbol{w},q)\in[H_D^1(\Omega)]^d\times L^2(\Omega)$ we have

$$\langle\boldsymbol{w},(\rho\nabla\boldsymbol{u})\boldsymbol{u}\rangle_\Omega + \langle\nabla^s\boldsymbol{w},2\mu(\nabla^s\boldsymbol{u})\nabla^s\boldsymbol{u}\rangle_{L^2(\Omega)} - \langle\nabla\cdot\boldsymbol{w},p\rangle_{L^2(\Omega)} = \langle\boldsymbol{w},\boldsymbol{f}\rangle_\Omega + \langle\boldsymbol{w},\boldsymbol{t}\rangle_{\Gamma_N}\,, \tag{3.11}$$

$$\langle q,\nabla\cdot\boldsymbol{u}\rangle_{L^2(\Omega)} = 0\,, \tag{3.12}$$

where $\boldsymbol{t} = \mathbb{S}\boldsymbol{n} - p\boldsymbol{n}$ are the normal boundary tractions and $H_D^{-1}(\Omega)$ is the dual of the space $H_D^1(\Omega) := \left\{w\in H^1(\Omega)\ :\ w|_{\Gamma_D}=0\right\}$. While prescribing the real traction $\boldsymbol{t}$ as natural boundary condition (BC) is crucial in fluid-structure interaction (FSI) for an accurate interface

coupling, simulating outflow conditions for truncated domains requires using the pseudo-traction $\tilde{\boldsymbol{t}} = (\mu\nabla\boldsymbol{u})\boldsymbol{n} - p\boldsymbol{n}$, see Refs. [40–42]. In fact, for the Newtonian case this is the standard setting, with the weak momentum equation (3.11) rewritten as

$$\langle \boldsymbol{w}, (\rho\nabla\boldsymbol{u})\boldsymbol{u}\rangle_\Omega + \langle \nabla\boldsymbol{w}, \mu\nabla\boldsymbol{u}\rangle_{L^2(\Omega)} - \langle \nabla\cdot\boldsymbol{w}, p\rangle_{L^2(\Omega)} = \langle \boldsymbol{w}, \boldsymbol{f}\rangle_\Omega + \langle \boldsymbol{w}, \tilde{\boldsymbol{t}}\rangle_{\Gamma_N}\,.$$

This is called the Laplacian formulation of the momentum equation, as it is derived from the fact that (for a homogeneous Newtonian fluid)

$$\nabla\cdot\mathbb{S} = \mu\nabla\cdot\left[\nabla\boldsymbol{u} + (\nabla\boldsymbol{u})^\top\right] = \mu\left[\Delta\boldsymbol{u} + \nabla(\nabla\cdot\boldsymbol{u})\right] = \mu\Delta\boldsymbol{u}\,,$$

since $\nabla\cdot\boldsymbol{u} = 0$. Therefore, when integration by parts is used in the reduced stress divergence $\mu\Delta\boldsymbol{u}$, the normal pseudo-traction $\tilde{\boldsymbol{t}}$ arises as natural BC. However, in the generalised Newtonian case, one is somewhat forced to use integration by parts on the full viscous term $\nabla\cdot\mathbb{S}$ to avoid second-order differentiation of the velocity field. This leaves us with the so-called *stress-divergence* (SD) or *elasticity* formulation (3.11), having natural BCs given in terms of *real* tractions $\boldsymbol{t}$. In Section 3.4 we show how for the generalised Newtonian case it is also possible to devise an appropriate variational formulation with pseudo-tractions as natural BC.

3.3 Outflow boundary conditions

Strictly speaking, the only flow boundary conditions that can be modelled with very high certainty are those of a confined flow: any viscous fluid in contact with a solid wall will have, at each contact point, the same local velocity as the wall – the so-called *no-slip* condition. Therefore, a fluid completely confined in an immovable container will satisfy the homogeneous Dirichlet condition $\boldsymbol{u}|_\Gamma = \boldsymbol{0}$. Unfortunately, in practical situations one is seldom in position to work with pure Dirichlet problems. Most engineering and biomedical flow applications consider a domain which has been truncated from a larger system. Let us take for example the domain shown in Figure 3.1, which illustrates the aorta, the largest artery in the human body. Since there is an incoming blood flow pumped by the heart, it is possible to estimate an inflow profile which varies periodically in time. The velocity on the vessel walls can either be given in terms of clinical imaging data or included as an unknown in an FSI context (or even be neglected, if we are only interested in a pure flow simulation). So, the remaining question is what to do on the truncated outlets.

Ideally, we should know either the outflow velocity profile or the normal boundary tractions, but this is seldom the case. On a section Γ_j of the outflow boundary Γ_N, one can at best estimate mean ouflow pressures $\bar{p}_j(t)$ via lumped (reduced-order) flow models based on measured data [43]. However, enforcing only pressure data is not an option, since natural BCs include velocity contributions. Therefore, a question which has long kept the (computational) fluid dynamics community busy is how to *best* enforce such outflow data

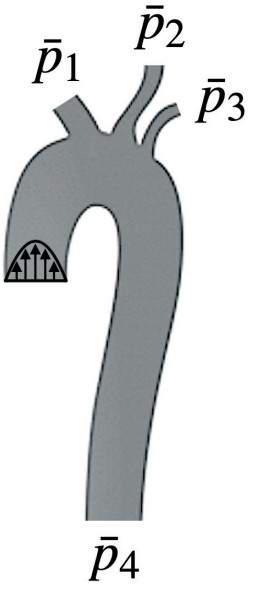

Figure 3.1: Illustration of an aortic domain with one inlet and four outlets.

on a truncated boundary while minimising the resulting upstream perturbation to the flow field. It is nowadays widely accepted that using pseudo-tractions for such a purpose can attain the desired results. For a planar outlet Γ_j, the condition

$$(\mu\nabla\boldsymbol{u})\boldsymbol{n} - p\boldsymbol{n} = -\bar{p}_j\boldsymbol{n} \tag{3.13}$$

is not only satisfied by Womersley and Poiseuille flows, but also allows vortices to leave the computational domain with minimal upstream perturbation (we refer the reader to the works of Gresho and Sani [44] and Rannacher [40] for an excellent discussion on outflow BCs). Nevertheless, in standard formulations for generalised Newtonian fluids, the natural BC is expressed in terms of real tractions, that is, we are somewhat forced to impose

$$(2\mu\nabla^s\boldsymbol{u})\boldsymbol{n} - p\boldsymbol{n} = -\bar{p}_j\boldsymbol{n} \quad \text{on} \quad \Gamma_j\,, \tag{3.14}$$

which is known to induce nonphysical flow behaviour around Γ_N, even for the simplest case of laminar Newtonian flow through a straight channel [42]. Such spurious behaviours for the non-Newtonian case are also found (but rarely discussed) in the literature [45, 46]. This has motivated us to search for a variational formulation for the generalised problem with pseudo-tractions as natural BC, as discussed in Section 3.4.

Remark 3.1. *For highly convective flows (large Reynolds numbers), possible flow inversion on the boundary can lead to numerical instabilities [47, 48]. This can be remedied by augmenting the natural boundary data with artificial terms penalising inward flow components. A comprehensive review on such backflow stabilisation methods can be found in Ref. [49].*

For now, we wish to show some simple yet useful results for non-Newtonian problems with natural BCs. If the computational domain has only one outlet, any value can be set for the mean outflow pressure, since all the flow coming from the inlet has to necessarily leave through that outlet. The only difference between setting $\tilde{\boldsymbol{t}}$ as zero or another constant (proportional to $\boldsymbol{n}$) is a constant (in space) shift on the pressure field, which is not relevant for incompressible flows. Therefore, one normally sets $\tilde{\boldsymbol{t}} = \boldsymbol{0}$ simply to get rid of the boundary integral. On the other hand, when multiple outlets are considered, as often happens in hemodynamics, appropriate mean values must be prescribed at each of the outlets. The variation of such spatial means throughout time are either measured or obtained through a reduced approach such as Windkessel and porous-media-based models [43, 50]. For the two-dimensional, homogeneous Newtonian case, Heywood et al. [41] showed that setting $\tilde{\boldsymbol{t}} = -\bar{p}\boldsymbol{n}$ on a straight outlet leads to an implicit enforcement of the value $\bar{p}$ as the mean pressure on that outlet. What we present now is a generalisation of that result to the inhomogeneous case ($\nabla\mu \not\equiv \boldsymbol{0}$). Let Γ_j be an outflow portion of the boundary Γ where the mean pressure $\bar{p}_j$ is known. We wish to enforce this condition by setting $\tilde{\boldsymbol{t}}_j = -\bar{p}_j\boldsymbol{n}_j$, i.e.,

$$(\mu\nabla\boldsymbol{u})\boldsymbol{n} - p\boldsymbol{n} = -\bar{p}_j\boldsymbol{n}_j \ \text{ on } \ \Gamma_j\,, \tag{3.15}$$

with $\boldsymbol{n}_j := \boldsymbol{n}|_{\Gamma_j}$. We are going to show that this condition enforces the mean pressure exactly for homogeneous Newtonian fluids, and approximately for quasi-Newtonian ones. The proof considers a three-dimensional setting, but the results hold also for the two-dimensional case. Two assumptions are needed:

- Γ_j is generated from a planar cut, so that $\boldsymbol{n}_j$ is constant.
- The line $s_j := \partial\Gamma_j$ enclosing Γ_j belongs to a wall, so that $\boldsymbol{u}|_{s_j} = \boldsymbol{0}$.

Figure 3.2 depicts an example of an aortic domain with multiple outlets, one of which is shown in close-up to illustrate the discussion. Without loss of generality, let us assume that direction x_3 is parallel to $\boldsymbol{n}_j$ and directions x_1 and x_2 are parallel to Γ_j. We wish to show that

$$\tilde{\boldsymbol{t}}_j = -\bar{p}_j\boldsymbol{n}_j \ \Rightarrow \int_{\Gamma_j} \left(p - \bar{p}_j\right) \mathrm{d}\Gamma \approx 0\,. \tag{3.16}$$

We begin by dotting both sides of Eq. (3.15) by $\boldsymbol{n}_j$ and integrating the result over Γ_j, yielding

$$\int_{\Gamma_j} p \,\mathrm{d}\Gamma = \bar{p}_j \int_{\Gamma_j} \mathrm{d}\Gamma + \int_{\Gamma_j} \mu\boldsymbol{n}_j \cdot \left[(\nabla\boldsymbol{u})\boldsymbol{n}_j\right] \mathrm{d}\Gamma\,. \tag{3.17}$$

Since $\boldsymbol{n}_j$ is constant, we can write

$$\begin{aligned}\boldsymbol{n}_j \cdot \left[(\nabla \boldsymbol{u})\boldsymbol{n}_j\right] &= \boldsymbol{n}_j \cdot \nabla\left(\boldsymbol{u} \cdot \boldsymbol{n}_j\right) \\ &= \frac{\partial u_3}{\partial x_3} = -\left(\frac{\partial u_1}{\partial x_1} + \frac{\partial u_2}{\partial x_2}\right),\end{aligned}$$

due to incompressibility. Hence:

$$\begin{aligned}\int_{\Gamma_j} \mu \boldsymbol{n}_j \cdot \left[(\nabla \boldsymbol{u})\boldsymbol{n}_j\right] \mathrm{d}\Gamma &= -\int_{\Gamma_j} \left(\frac{\partial u_1}{\partial x_1} + \frac{\partial u_2}{\partial x_2}\right) \mu \, \mathrm{d}x_1 \mathrm{d}x_2 \\ &= \int_{\Gamma_j} \left(u_1 \frac{\partial \mu}{\partial x_1} + u_2 \frac{\partial \mu}{\partial x_2}\right) \mathrm{d}x_1 \mathrm{d}x_2 - \int_{s_j} \mu \boldsymbol{n}_{s_j} \cdot \boldsymbol{u} \, \mathrm{d}s \\ &= \int_{\Gamma_j} \nabla_\tau \mu \cdot \boldsymbol{u}_\tau \, \mathrm{d}\Gamma - \int_{s_j} \mu \boldsymbol{n}_{s_j} \cdot \boldsymbol{u} \, \mathrm{d}s,\end{aligned} \tag{3.18}$$

where $\boldsymbol{n}_{s_j}$ is the outward unit normal vector on s_j, $\boldsymbol{u}_\tau$ is the velocity component tangential to Γ_j and ∇_τ denotes the tangential derivative on Γ_j. The last integral in Eq. (3.18) is zero, since $\boldsymbol{u}|_{s_j} = \boldsymbol{0}$, by assumption (no slip). Thus, from Eq. (3.17) we finally get

$$\int_{\Gamma_j} p \, \mathrm{d}\Gamma - \bar{p}_j \int_{\Gamma_j} \mathrm{d}\Gamma = \int_{\Gamma_j} \nabla_\tau \mu \cdot \boldsymbol{u}_\tau \, \mathrm{d}\Gamma. \tag{3.19}$$

If the viscosity is constant, then the right-hand side vanishes and the mean pressure is enforced exactly, which is a known result for Newtonian fluids [41]. For the generalised case this is not always true, but if the flow is hydraulically developed at the outlet and Γ_j is normal to the main flow direction (*cf.* Figure 3.2), then $\boldsymbol{u}_\tau = \boldsymbol{0}$ and the additional term will vanish (mind that developed flows need not be stationary). In practice, non-zero tangential flow components may exist and lead to slight differences between $\bar{p}_j$ and the actual mean pressure on Γ_j. It is possible to show that, when such a discrepancy exists, it will be twice as large if the mean pressure is enforced via real tractions $\boldsymbol{t}$. This offers an additional reason for working with pseudo-tractions.

In the light of what we have presented regarding outflow boundary conditions, a question that naturally arises is: can pseudo-tractions be enforced, even though they are not the natural data for the stress-divergence formulation? The answer is yes, and this can be done using a boundary term. We first notice the splitting

$$\boldsymbol{t} = \tilde{\boldsymbol{t}} + (\mu \nabla \boldsymbol{u})^\top \boldsymbol{n}.$$

The first term on the right-hand side is the quantity we want to enforce, so it can be replaced by the appropriate data. The second part is brought to the left-hand side and handled as an

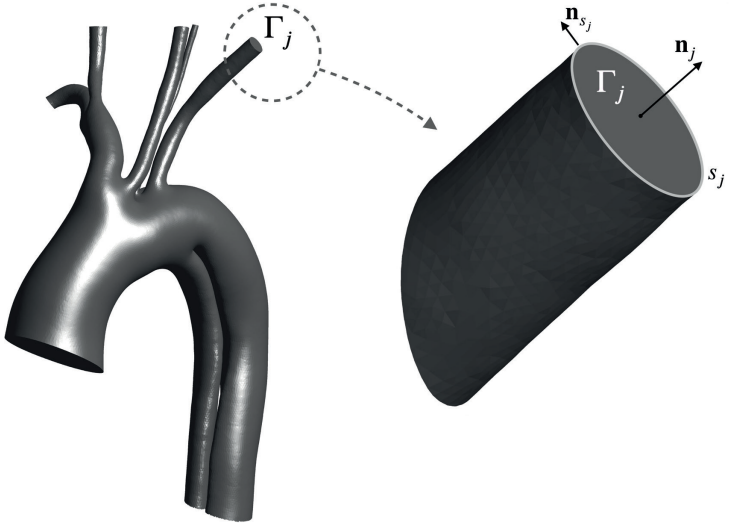

Figure 3.2: Illustration of planar outlet regions in an aortic domain.

unknown term. Therefore, the momentum equation is modified to

$$\langle \boldsymbol{w}, (\rho \nabla \boldsymbol{u}) \boldsymbol{u} \rangle_{\Omega} + \langle \nabla^s \boldsymbol{w}, 2\mu \nabla^s \boldsymbol{u} \rangle_{L^2(\Omega)} - \langle \nabla \cdot \boldsymbol{w}, p \rangle_{L^2(\Omega)} - \left\langle \boldsymbol{w}, (\mu \nabla \boldsymbol{u})^{\top} \boldsymbol{n} \right\rangle_{\Gamma} = \langle \boldsymbol{w}, \boldsymbol{f} \rangle_{\Omega} + \langle \boldsymbol{w}, \tilde{\boldsymbol{t}} \rangle_{\Gamma_N} . \tag{3.20}$$

Although this formulation, to the best of our knowledge, has not been presented or applied before – especially not for non-Newtonian fluids –, a similar idea was used by Huber et al. [51] for two-phase flows, but exactly the other way around: augmenting the Laplacian form with a boundary integral to force real traction BCs. That is necessary for the interface coupling between two immiscible fluids in the presence of surface tension.

3.4 A generalised Laplacian formulation

The second question we aim to answer is: is it possible to devise a formulation for generalised Newtonian fluids having pseudo-tractions as *natural* data? Or, in other words, can the Laplacian form of the Navier–Stokes variational problem be generalised to fluids with variable viscosity? One reason to look for such a formulation as an alternative to the one just presented is avoiding boundary integrals, since they require a data structure which is not always available in finite element codes. In problems with a single outlet, as often appearing in engineering applications with non-Newtonian fluids (e.g., polymer extrusion

[52, 53]), we could simply set $\tilde{\boldsymbol{t}} = \boldsymbol{0}$ on the outlet and eliminate the boundary term on the right-hand side. In this context, our motivation here is to reformulate the variational problem for quasi-Newtonian fluids so as to yield the same natural boundary conditions as in the Newtonian Laplacian formulation. The first step is to rewrite the viscous term as

$$\nabla \cdot (2\mu\nabla^s \boldsymbol{u}) = 2\nabla^s \boldsymbol{u}\nabla\mu + \mu\Delta\boldsymbol{u} + \mu\nabla(\nabla\cdot\boldsymbol{u}) = 2\nabla^s \boldsymbol{u}\nabla\mu + \mu\Delta\boldsymbol{u}\,. \tag{3.21}$$

Hence, the stress term in the variational formulation reads

$$\int_\Omega \boldsymbol{w}\cdot\left[\nabla p - \mu\Delta\boldsymbol{u} - (\nabla\boldsymbol{u})^\top\nabla\mu - \nabla\boldsymbol{u}\nabla\mu\right]\mathrm{d}\Omega\,. \tag{3.22}$$

As in the Newtonian case, the natural boundary condition is obtained through integration by parts of the terms containing the velocity Laplacian and the pressure gradient:

$$\int_\Omega \boldsymbol{w}\cdot(\nabla p - \mu\Delta\boldsymbol{u})\,\mathrm{d}\Omega = \int_\Omega \nabla\boldsymbol{u} : \nabla(\mu\boldsymbol{w})\,\mathrm{d}\Omega - \int_\Omega p\nabla\cdot\boldsymbol{w}\,\mathrm{d}\Omega - \int_\Gamma \boldsymbol{w}\cdot\left[(\mu\nabla\boldsymbol{u})\boldsymbol{n} - p\boldsymbol{n}\right]\mathrm{d}\Gamma\,, \tag{3.23}$$

where the same natural BC as in the Laplacian formulation for Newtonian fluids can be identified. Moreover,

$$\int_\Omega \nabla\boldsymbol{u} : \nabla(\mu\boldsymbol{w})\,\mathrm{d}\Omega = \int_\Omega \nabla\boldsymbol{u} : (\mu\nabla\boldsymbol{w} + \boldsymbol{w}\otimes\nabla\mu)\,\mathrm{d}\Omega \equiv \int_\Omega \mu\nabla\boldsymbol{u} : \nabla\boldsymbol{w}\,\mathrm{d}\Omega + \int_\Omega \boldsymbol{w}\cdot(\nabla\boldsymbol{u}\nabla\mu)\,\mathrm{d}\Omega\,. \tag{3.24}$$

Since the last integrals in Eqs. (3.24) and (3.22) cancel out, the weak form of the momentum equation reduces to

$$\langle\boldsymbol{w},(\rho\nabla\boldsymbol{u})\boldsymbol{u}\rangle_\Omega + \langle\nabla\boldsymbol{w},\mu\nabla\boldsymbol{u}\rangle_{L^2(\Omega)} - \left\langle\boldsymbol{w},(\nabla\boldsymbol{u})^\top\nabla\mu\right\rangle_\Omega - \langle\nabla\cdot\boldsymbol{w},p\rangle_{L^2(\Omega)} = \langle\boldsymbol{w},\boldsymbol{f}\rangle_\Omega + \langle\boldsymbol{w},\tilde{\boldsymbol{t}}\rangle_{\Gamma_N}\,, \tag{3.25}$$

which will henceforth be denoted as *generalised* Laplacian (GL) formulation. Note that, if μ is a constant, the term containing $\nabla\mu$ vanishes and the Laplacian form for Newtonian fluids is recovered. When that is not the case, we will show in Chapter 4 that such a term must be handled carefully at the discrete level to avoid higher-order regularity requirements on the velocity space.

4 STABLE FINITE ELEMENT FORMULATIONS FOR STATIONARY FLOWS

When it comes to finite element methods for incompressible flow problems, the most infamous troublemaker is the saddle-point structure of the underlying system of equations. Since the pressure does not feature in the continuity equation, the finite element spaces used for discretising the mixed variational problem are subject to the LBB compatibility condition. Alternatively, perturbing the continuity equation to appropriately include the pressure can flexibilise the choice of finite element spaces. We shall henceforth denote the former formulations as *stable* ones, whereas the latter will be denoted as *stabilised* formulations. For concision and simplicity of presentation, the next chapters will focus on stationary cases, whereas discretisation methods for time-dependent problems are presented in Chapters 7 and 8.

The original results presented in this chapter, as well as the theoretical discussion on outflow boundary conditions from the previous chapter, have been published as a research article [54].

4.1 Stress-divergence formulation

Let $X_h^u \subset [H^1(\Omega)]^d$ and $X_h^p \subset L^2(\Omega)$ be conforming velocity and pressure finite element spaces, respectively. The finite-dimensional variational problem reads: find $(\boldsymbol{u}_h, p_h) \in X_h^u \times X_h^p$, with $\boldsymbol{u}_h|_{\Gamma_D} = \boldsymbol{g}_h$, such that for all $(\boldsymbol{w}_h, q_h) \in X_h^u \times X_h^p$, $\boldsymbol{w}_h|_{\Gamma_D} = \boldsymbol{0}$, we have

$$\begin{aligned} \langle \boldsymbol{w}_h, (\rho \nabla \boldsymbol{u}_h)\boldsymbol{u}_h \rangle_\Omega + \langle \nabla^s \boldsymbol{w}_h, 2\mu(\nabla^s \boldsymbol{u}_h)\nabla^s \boldsymbol{u}_h \rangle_{L^2(\Omega)} - \langle \nabla \cdot \boldsymbol{w}_h, p_h \rangle_{L^2(\Omega)} &= \langle \boldsymbol{w}_h, \boldsymbol{f} \rangle_\Omega + \langle \boldsymbol{w}_h, \boldsymbol{t} \rangle_{\Gamma_N}, \\ \langle q_h, \nabla \cdot \boldsymbol{u}_h \rangle_{L^2(\Omega)} &= 0, \end{aligned} \tag{4.1}$$

with $\boldsymbol{g}_h$ being an X_h^u-compatible approximation/interpolation of the Dirichlet data $\boldsymbol{g}$. In the simplest case where $X_h^u = [X_h^p]^d$ (equal-order velocity-pressure pairs), the variational formulation is unstable, i.e., not uniquely solvable. Hood and Taylor [55] discovered the first stable pair, which consisted of serendipity elements (second-order quadrilateral elements with no internal nodes) for the velocity, combined with bilinear quadrilaterals for the pressure. The stability and optimal convergence of the generalised Taylor–Hood elements $P_{k+1}P_k$ and $Q_{k+1}Q_k$, $k \in \mathbb{N}$, was later shown by Brezzi and Falk [56]. The $Q_{k+1}Q_k^{dc}$ pairs, with superscript dc denoting discontinuous basis functions, are also stable [57]. These

pairs have the advantage of providing element-wise mass conservation, but obviously increase the number of pressure degrees of freedom. Another stable pair with discontinuous pressure is the $P_d P_0$ element, but its convergence is only linear [58]. There are also several non-Lagrangian pairs which are LBB-stable, such as the MINI, Crouzeix-Raviart and Rannacher-Turek elements (see Refs. [57–59] for a comprehensive description of stable and unstable pairs).

4.2 Generalised Laplacian formulation

In our generalised Laplacian formulation, the viscous term in the weak form reads

$$\langle \nabla \boldsymbol{w}, \mu \nabla \boldsymbol{u} \rangle_{L^2(\Omega)} - \left\langle \boldsymbol{w}, (\nabla \boldsymbol{u})^\top \nabla \mu \right\rangle_\Omega ,$$

which brings a practical issue for the discretisation: when the viscosity is not only variable but also a function of the velocity gradient, the presence of the term $\nabla\mu$ implies second-order differentiation of the velocity field, prohibiting the use of standard Lagrangian elements for $\boldsymbol{u}_h$. To circumvent the need for C^1-conforming finite element spaces, we apply to the viscosity field the well known idea of L^2 projection onto a continuous space, as done for the stress tensor in least-squares finite element methods [60–62]. In our case, this corresponds to introducing μ as a continuous additional unknown and recovering it weakly through the rheological law. The resulting discrete problem looks for $(\boldsymbol{u}_h, p_h, \mu_h) \in X_h^u \times X_h^p \times X_h^\mu$, with $\boldsymbol{u}_h|_{\Gamma_D} = \boldsymbol{g}_h$, such that

$$\begin{aligned} \left\langle \boldsymbol{w}_h, (\rho \nabla \boldsymbol{u}_h)\boldsymbol{u}_h - (\nabla \boldsymbol{u}_h)^\top \nabla \mu_h - \boldsymbol{f} \right\rangle_\Omega + \langle \nabla \boldsymbol{w}_h, \mu_h \nabla \boldsymbol{u}_h \rangle_{L^2(\Omega)} - \langle \nabla \cdot \boldsymbol{w}_h, p_h \rangle_{L^2(\Omega)} &= \langle \boldsymbol{w}_h, \tilde{\boldsymbol{t}} \rangle_{\Gamma_N} , \\ \langle q_h, \nabla \cdot \boldsymbol{u}_h \rangle_{L^2(\Omega)} &= 0 , \\ \langle \upsilon_h, \eta(\dot{\gamma}(\nabla^s \boldsymbol{u}_h)) - \mu_h \rangle_{L^2(\Omega)} &= 0 \end{aligned} \tag{4.2}$$

for all $(\boldsymbol{w}_h, q_h, \upsilon_h) \in X_h^u \times X_h^p \times X_h^\mu$, with $\boldsymbol{w}_h|_{\Gamma_D} = \boldsymbol{0}$, where X_h^μ is a continuous finite element space. For stability and optimal convergence, we can use first-order elements for pressure and viscosity, and second-order elements for the velocity. It is important to remark that a generalised Newtonian model is essentially a homogenisation approach: the concept of an apparent viscosity μ is a simplifying assumption to account for multi-scale effects and inhomogeneities (e.g., the different components of blood) within a single-phase fluid model. In this context, introducing the viscosity as a continuous field in (4.2) is consistent with the single-phase assumption. In Section 6.4 we show a two-phase flow example where the viscosity is actually *not* continuous and the stress-divergence formulation is thus recommended.

The last equation in (4.2) corresponds to a mass matrix problem, so that if we use an appropriate linearisation for the overall system, we can minimise the extra cost due to

treating the viscosity as an additional variable. A quick choice of iterative method to solve the present nonlinear problem would be Newton–Raphson. Yet, by naively doing so, one would spoil the simple coupling between velocity and viscosity in the projection step, thereby generating a fully-coupled system and increasing the computational cost. Conversely, Picard-like methods are an attractive option here. In fact, an iterative method can be specifically devised so as to exploit the particular features of the nonlinear system at hand here. The viscous term in the momentum equation has two distinct terms, one being the usual weak Laplacian arising in the Navier–Stokes problem, which is normally incorporated into the velocity-velocity block of the system. The main question is then how to handle the additional part due to $\nabla\mu$, as it can be incorporated into either the velocity-velocity block or the velocity-viscosity block. We propose the following: given a previous iterate $\left(\boldsymbol{u}_h^k, p_h^k\right)$, we first compute μ_h^k via

$$\left\langle \upsilon_h, \mu_h^k \right\rangle_{L^2(\Omega)} = \left\langle \upsilon_h, \eta_h^k \right\rangle_{L^2(\Omega)}, \tag{4.3}$$

with $\eta_h^k := \eta\left(\dot{\gamma}\left(\nabla^s \boldsymbol{u}_h^k\right)\right)$, then the next iterate $\left(\boldsymbol{u}_h^{k+1}, p_h^{k+1}\right)$ via

$$\begin{aligned}\left\langle \boldsymbol{w}_h, (\rho\nabla\boldsymbol{u}_h^k)\boldsymbol{u}_h^{k+1}\right\rangle_\Omega + \left\langle \nabla\boldsymbol{w}_h, \mu_h^k\nabla\boldsymbol{u}_h^{k+1}\right\rangle_{L^2(\Omega)} - \left\langle \nabla\cdot\boldsymbol{w}_h, p_h^{k+1}\right\rangle_{L^2(\Omega)} &= \left\langle \boldsymbol{w}_h, (\nabla\boldsymbol{u}_h^k)^\top\nabla\mu_h^k + \boldsymbol{f}\right\rangle_\Omega \\ &\quad + \langle \boldsymbol{w}_h, \tilde{\boldsymbol{t}}\rangle_{\Gamma_N}, \\ \left\langle q_h, \nabla\cdot\boldsymbol{u}_h^{k+1}\right\rangle_{L^2(\Omega)} &= 0,\end{aligned} \tag{4.4}$$

The iterations proceed until convergence, according to a preset tolerance. In fact, such fixed point iterations are known to have generally a larger convergence radius than the Newton–Raphson method [57]. The corresponding matrix system has the form

$$\mathbf{M}\underline{\mu}^k = \underline{r}(\boldsymbol{u}_h^k), \tag{4.5}$$

$$\begin{bmatrix} \mathbf{C}(\boldsymbol{u}_h^k) + \mathbf{K}(\mu_h^k) & -\mathbf{B}^\top \\ \mathbf{B} & \mathbf{0} \end{bmatrix} \begin{pmatrix} \underline{\boldsymbol{u}}^{k+1} \\ \underline{p}^{k+1} \end{pmatrix} = \begin{pmatrix} \underline{\boldsymbol{b}} + \mathbf{S}(\boldsymbol{u}_h^k)\underline{\mu}^k \\ \underline{0} \end{pmatrix}, \tag{4.6}$$

where the underlined quantities stand for vectors of nodal values, $\mathbf{K}$, $\mathbf{C}$ and $\mathbf{B}$ are the usual diffusion, convection and divergence matrices from the Navier–Stokes problem [57], $\mathbf{M}$ is a standard mass matrix and $\underline{\boldsymbol{b}}$ is a vector accounting for BCs and body forces. Matrix $\mathbf{S}(\boldsymbol{u}_h)$ has d blocks with the following structure:

$$\mathbf{S} = \begin{bmatrix} \mathbf{S}^1 \\ \vdots \\ \mathbf{S}^d \end{bmatrix}, \text{ with } S_{ij}^m(\boldsymbol{u}_h) = \left\langle \psi_i^u \frac{\partial \boldsymbol{u}_h}{\partial x_m}, \nabla\psi_j^\mu \right\rangle_{L^2(\Omega)}, \tag{4.7}$$

in which $(\psi^u, \psi^p, \psi^\mu)$ denotes the basis functions used in the velocity, pressure and viscosity spaces. In this way, it is possible to recover the viscosity separately from the rest of the

system, which keeps the computational overhead from introducing an additional unknown to a minimum. Besides, the additional viscous term introduced by the present formulation can be treated simply as a right-hand side instead of contributing to the coefficient matrix. The system matrix left to be inverted in Eq. (4.6) is thus a classical Laplacian matrix, which allows a variety of well known efficient incompressible flow solvers and preconditioners to be readily applied here. A simple Aitken relaxation step is then added after each iteration, resulting in quadratic convergence for the overall iterative scheme [63], as we show in our numerical examples. Details on the implementation of Aitken acceleration can be found in Refs. [64, 65].

Remark 4.1. *The block structure in* (4.7) *assumes that* $\underline{\boldsymbol{u}}$ *is organised component-wise: first all the nodal values of the first velocity component* u_1*, then the same for* u_2*, and so on.*

4.3 Numerical examples

This section presents various two-dimensional numerical examples with different rheological models. We aim to verify the convergence of our generalised Laplacian formulation, as well as illustrate the impact of considering appropriate outflow conditions. Unless where otherwise stated, the generalised Laplacian formulation is being employed.

Channel flow of a power-law fluid

One of the simplest models used for blood and polymer flows is the power-law relation

$$\eta(\dot{\gamma}) = \kappa \dot{\gamma}^{n-1}, \tag{4.8}$$

where $\kappa > 0$ and $n < 1$ for a shear-thinning fluid such as blood. It has the physical inconsistency of yielding infinite viscosity for $\dot{\gamma} = 0$, but is used quite often in practice. In a straight channel $\Omega = (0, L) \times \left(-\frac{H}{2}, \frac{H}{2}\right)$, the analytical solution for the hydraulically developed flow reads

$$p = \frac{4\kappa}{H}\left[\left(\frac{2n+1}{n}\right)\frac{Q}{H^2}\right]^n (L - x_1), \quad u_1 = \left(\frac{2n+1}{n+1}\right)\frac{Q}{H}\left(1 - \left|\frac{2x_2}{H}\right|^{\frac{n+1}{n}}\right), \tag{4.9}$$

where Q is the volumetric flow rate per unit width. We will use this solution to verify the order of approximation of the present formulation. The following BCs are considered for the simulation: no slip ($\boldsymbol{u} = \boldsymbol{0}$) on the walls ($x_2 = \pm H/2$), the analytical profile with $Q = 100$ mm^2/s on the inlet ($x_1 = 0$), and the do-nothing condition ($\tilde{\boldsymbol{t}} = \boldsymbol{0}$) on the outlet ($x = L$). We use hemodynamic parameters [4] $\rho = 1050$ kg/m^3, $\kappa = 0.035$ Pa.s$^{0.6}$ and $n = 0.6$, with the geometric parameters $L = 3H = 3$ mm. A convergence study is carried out with Q_2Q_1 rectangular elements: the coarsest mesh is created by dividing both L and

H by five; then, four levels of uniform refinement are considered. Figure 4.1 shows the velocity and pressure errors with respect to the mesh size h. Optimal convergence rates can be verified: cubic for velocity and quadratic for pressure, in the L^2 norm. To assess the iterative convergence, we define the iteration residual as

$$\varepsilon_{k+1} := \frac{\left|\underline{\boldsymbol{q}}^{k+1} - \underline{\boldsymbol{q}}^{k}\right|}{\left|\underline{\boldsymbol{q}}^{k+1}\right|}, \quad \text{with} \quad \underline{\boldsymbol{q}}^{k} = \begin{pmatrix} \underline{\boldsymbol{u}}^{k} \\ \underline{p}^{k} \\ \underline{\mu}^{k} \end{pmatrix}. \tag{4.10}$$

The residual evolution for the coarsest mesh and the finest mesh are depicted in Figure 4.2, where the expected quadratic convergence of the iterative scheme can be clearly verified.

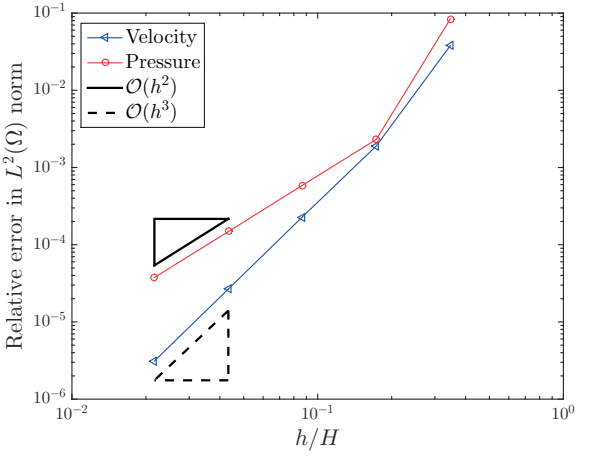

Figure 4.1: Power-law channel flow: uniform refinement study showing optimal convergence for the Taylor–Hood discretisation of the generalised Laplacian formulation.

Channel flow of a Bingham plastic

Another important type of non-Newtonian fluid is the Bingham plastic. Such materials only start flowing when a minimum shear stress level is reached, after which they behave as Newtonian fluids [1]. To avoid the need for tracking yield surfaces, Papanastasiou [66] proposed a smoothened version fitting the generalised Newtonian framework:

$$\eta(\dot{\gamma}) = \mu_\infty + \frac{\left(1 - e^{-m\dot{\gamma}}\right)\tau_0}{\dot{\gamma}}, \tag{4.11}$$

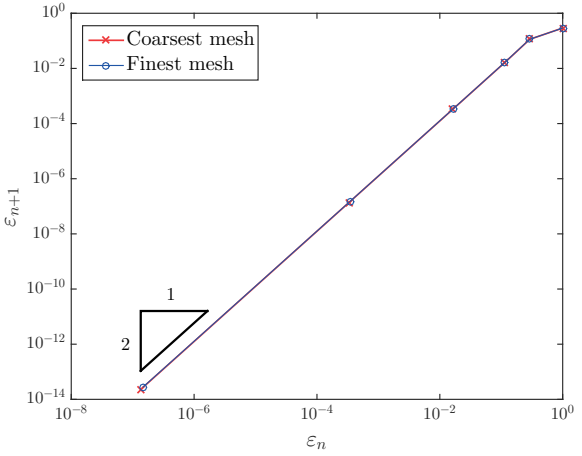

Figure 4.2: Power-law channel flow: evolution of the iteration residual confirming the quadratic convergence of the Aitken-accelerated Picard scheme.

where μ_∞ is the Newtonian viscosity, τ_0 is the yield stress and m is a positive regularisation parameter. The exact Bingham model is recovered when $m \to \infty$. The analytical expression for the fully developed Bingham flow profile in a straight channel is

$$u_1 = \begin{cases} -\frac{k}{2\mu_\infty}\left(\frac{H-D}{2}\right)^2 + \frac{kD^2}{8\mu_\infty}\left(1-\left|\frac{2x_2}{D}\right|\right)^2, & \text{if } \frac{D}{2} < |x_2| \le \frac{H}{2}, \\ -\frac{k}{2\mu_\infty}\left(\frac{H-D}{2}\right)^2, & \text{if } 0 \le |x_2| \le \frac{D}{2}, \end{cases} \tag{4.12}$$

where D is the width of the unyielded region, given by [66]

$$D = 2\tau_0/|k|\,, \tag{4.13}$$

and k is the pressure gradient in the x_1 direction. When an inflow velocity profile is prescribed instead of a pressure drop, one must first compute k in terms of the inflow rate Q. From Eqs. (4.12) and (4.13) and the definition of Q, it is possible to derive a polynomial expression to find k in terms of the input parameters:

$$k^3 + \frac{3}{H}\left(\frac{4\mu_\infty Q}{H^2} + \tau_0\right)k^2 - 4\left(\frac{\tau_0}{H}\right)^3 = 0\,. \tag{4.14}$$

For this example, we prescribe $\tilde{\boldsymbol{t}} = \mathbf{0}$ at the outlet $x_1 = L$ and a parabolic velocity profile at the inlet $x_1 = 0$. The outflow velocity profile attained through the generalised Laplacian formulation is then compared to the analytical one. We set $\rho = 1050$ kg/m^3, $\mu_\infty = 3.45$

mPa.s, $\tau_0 = 0.2$ Pa, $m = 100$ s and $L = 10H = 10$ mm. The domain is divided uniformly into 300×300 square elements. We calculate the Reynolds number from the mean inflow velocity $\bar{u}$ as

$$\mathrm{Re} := \frac{\bar{u}H}{\nu_\infty} = \frac{\rho Q}{\mu_\infty},$$

and three values are considered: Re = 1, 10 and 100. The comparison between numerical and analytical results, depicted in Figure 4.3, reveals excellent agreement for all three cases considered. Note that the non-Newtonian behaviour is stronger for low Reynolds numbers, while hardly noticeable for Re = 100.

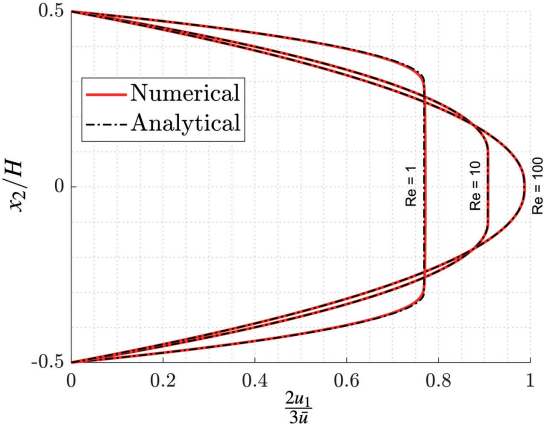

Figure 4.3: Comparison between numerical (GL) and analytical Bingham profiles.

Channel flow of a Carreau–Yasuda fluid

We now compare our generalised Laplacian formulation with the other two ones presented in Chapter 3, namely, the classical SD formulation with real traction natural BCs and the SD formulation augmented with a boundary term to enforce pseudo-tractions as outflow BCs (see Eq. (3.20)). For this example we consider the popular Carreau–Yasuda model

$$\eta(\dot{\gamma}) = \eta_\infty + (\eta_0 - \eta_\infty)\left[1 + (\lambda\dot{\gamma})^a\right]^{\frac{n-1}{a}}, \tag{4.15}$$

with the rheological parameters [36] $\rho = 1060$ kg/m^3, $\mu_\infty = 3.45$ mPa.s, $\mu_0 = 56$ mPa.s, $n = 0.22$, $\lambda = 3.804$ s and $a = 1.25$. The developed flow has a semi-analytical solution:

$$p = |k|(L - x_1), \;\; u = \int_{H/2}^{|x_2|} f(\tilde{y})\, \mathrm{d}\tilde{y},$$

where $|k|$ is the pressure drop per unit length and f is the solution of the nonlinear equation

$$\left\{\mu_\infty + (\mu_0 - \mu_\infty)\left[1 + (\lambda f)^a\right]^{\frac{n-1}{a}}\right\} f = -|k|y, \;\; y \in [0, H/2]\,. \tag{4.16}$$

We will use this known solution to assess numerical errors, setting $L = 3H = 3$ mm and $k = -3$ kPa/m. Instead of prescribing an inflow profile, this time we consider a pressure-driven flow by setting $\tilde{\boldsymbol{t}}|_{x_1=0} = (9,0)^\top$ Pa and $\tilde{\boldsymbol{t}}|_{x_1=L} = \boldsymbol{0}$, and analogously with real tractions $\boldsymbol{t}$ for the standard SD formulation. For the convergence study, the coarsest mesh has twelve square elements, and successive uniform refinements are applied. Bilinear basis functions are used now for all quantities, in combination with the parameter-free stabilisation method by Dohrmann and Bochev [25] (details on stabilised formulations will be addressed in Chapter 6). The error plot in Figure 4.4 reveals that, although the SD formulation with "forced" pseudo-tractions converges to the exact solution, it does so considerably slower than the GL formulation. The latter's pressure approximation is orders of magnitude more accurate than the former's. It is also clear that the classical SD formulation with traction BCs does not converge to the exact solution, and the reason for that can be seen in Figure 4.5: as well known for the Newtonian case, using real tractions to enforce mean pressures leads to spurious behaviour around traction boundaries.

Carreau–Yasuda fluid past a backward–facing step

The main reason for using pseudo-traction BCs is their ability to preserve accurate flow behaviours in truncated domains [1, 41, 42]. To illustrate this property in a non-Newtonian framework, we consider the classical backward-facing step (BFS) problem. Starting from a basic full-domain setup, we set up different test cases by truncating the domain at different positions, as illustrated in Figure 4.6. For each case we set zero mean outflow pressure, which is enforced by pseudo-tractions or real tractions, depending on the formulation (SD or GL). The remaining boundary conditions are a parabolic profile with volumetric flow rate Q at the inlet $x_1 = 0$, and no-slip elsewhere. We use the Carreau model

$$\eta(\dot{\gamma}) = \eta_\infty + (\eta_0 - \eta_\infty)\left[1 + (\lambda\dot{\gamma})^2\right]^{\frac{n-1}{2}}, \tag{4.17}$$

with representative hemodynamic parameters [4] $\rho = 1050$ kg/m^3, $\mu_\infty = 3.45$ mPa.s, $\mu_0 = 56$ mPa.s, $n = 0.3568$, $\lambda = 1.6565$ s. The domain is uniformly divided into square elements

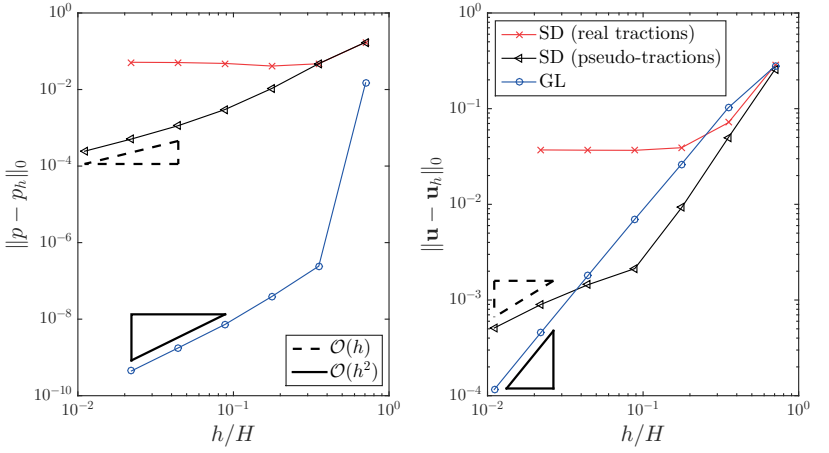

Figure 4.4: Carreau–Yasuda channel flow: convergence study for different formulations using first-order elements.

of length $H/50$, with $H = 1$ mm. We present the comparison in terms of the normalised viscosity

$$\bar{\mu} := \frac{\eta(\dot{\gamma}) - \mu_\infty}{\mu_0 - \mu_\infty}. \tag{4.18}$$

In the SD formulation, the viscosity field is discontinuous. Therefore, to allow a fair comparison, the viscosity is post-processed using the same continuous L^2 projection as for the GL formulation. Figure 4.7 depicts the normalised viscosity field computed from both formulations at Re = 1. The importance of using appropriate outflow BCs is also evident here. The GL formulation with $\tilde{\boldsymbol{t}} = \mathbf{0}$ yields physically consistent solutions all the way up to the outflow boundary, even when the domain is truncated before the flow is fully developed. The solution produced by the classical SD approach, conversely, is highly dependent on the position of the cut and yields clearly unphysical behaviour around the outlet region.

Carreau fluid through bifurcating channel

We now investigate the effect of pseudo-traction BCs in domains with more than one outlet. As a reference case, we consider a two-dimensional symmetric flow in the T-shaped domain depicted in Fig. 4.8. This can be viewed as a model problem for blood flows in bifurcating vessels or polymeric flows in pipe systems, and allows us to illustrate the

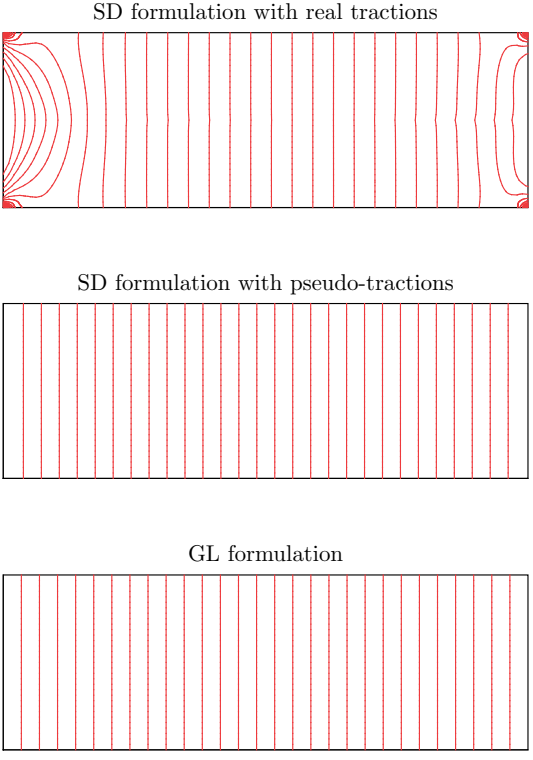

Figure 4.5: Carreau–Yasuda channel flow: pressure isolines for different formulations.

theoretical discussion of Subsection 3.3. A developed Carreau profile corresponding to Re = 15 is imposed at the inlet. The material parameters are as in the previous example and the dimensions are $L = 2H = 2$ mm. First, we impose $\tilde{\boldsymbol{t}} = \boldsymbol{0}$ on both outlets of the full domain. Then, we truncate one of the branches and enforce $\tilde{\boldsymbol{t}} = -\bar{p}_{\text{cut}}\boldsymbol{n}$, considering two different scenarios: first setting $\bar{p}_{\text{cut}} = 0$, then using the actual mean value obtained at that position from the full-domain simulation ($\bar{p}_{\text{cut}} \approx 10$ Pa). For this example, we use square bilinear elements of edge length $H/100$. The results are shown in Figure 4.9; the isolines are uniformly spaced (40 in total) and the velocity results are given in terms of the

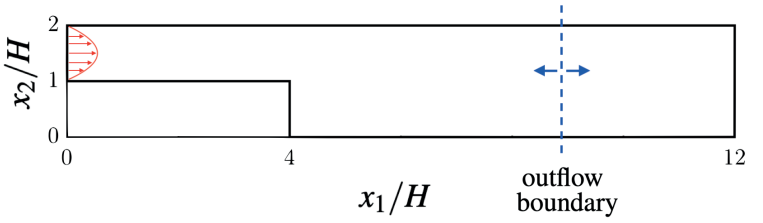

Figure 4.6: Problem setup for the BFS problem considering truncated domains.

normalised quantity

$$u^* := \frac{\sqrt{\boldsymbol{u} \cdot \boldsymbol{u}}}{Q/H} .$$

Setting the appropriate pseudo-traction allows us to recover the correct solution in spite of the asymmetric domain, while the simple "do-nothing" approach ($\bar{p}_{\text{cut}} = 0$) leads to a completely different flow behaviour.

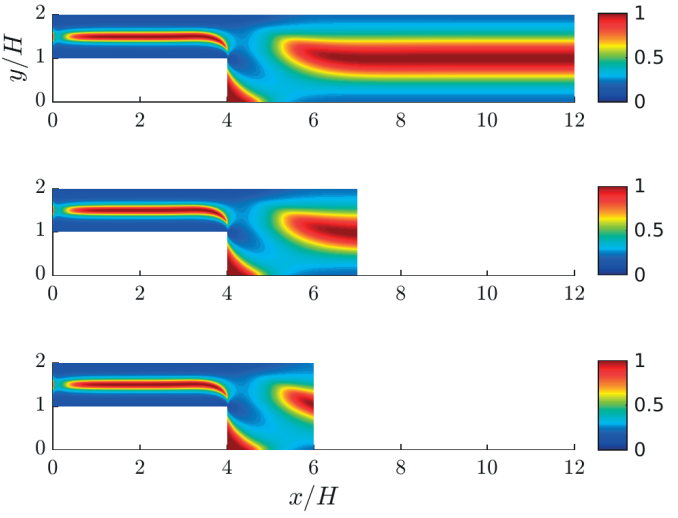

(a) Generalised Laplacian formulation with $\tilde{\boldsymbol{t}}|_{\Gamma_N} = \mathbf{0}$.

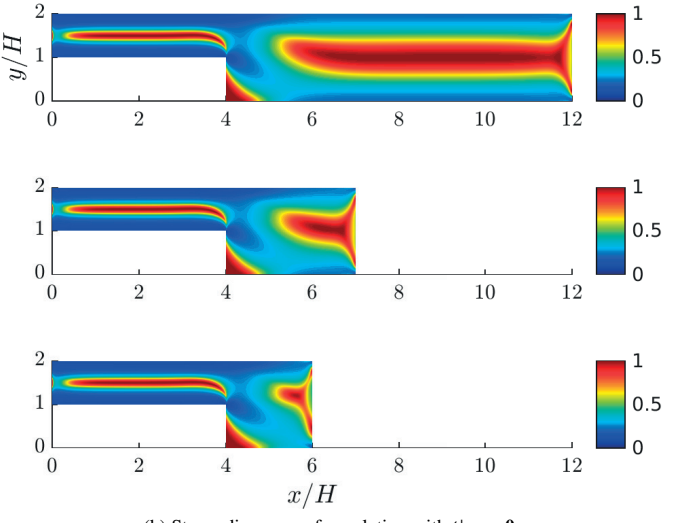

(b) Stress-divergence formulation with $\boldsymbol{t}|_{\Gamma_N} = \mathbf{0}$.

Figure 4.7: Normalised viscosity field for different outflow BCs in truncated domains.

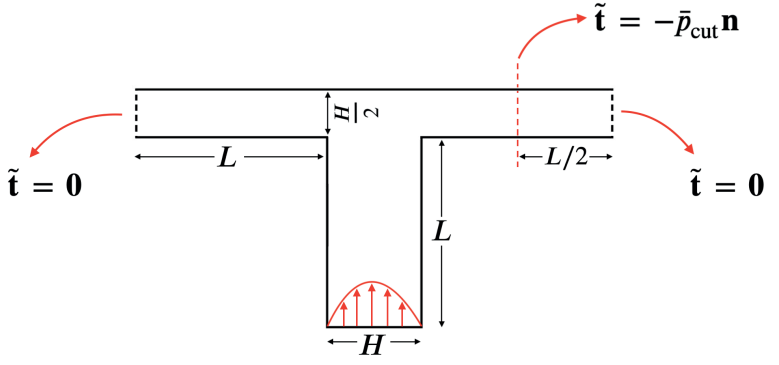

Figure 4.8: Problem setup for the Carreau fluid in a T-shaped domain.

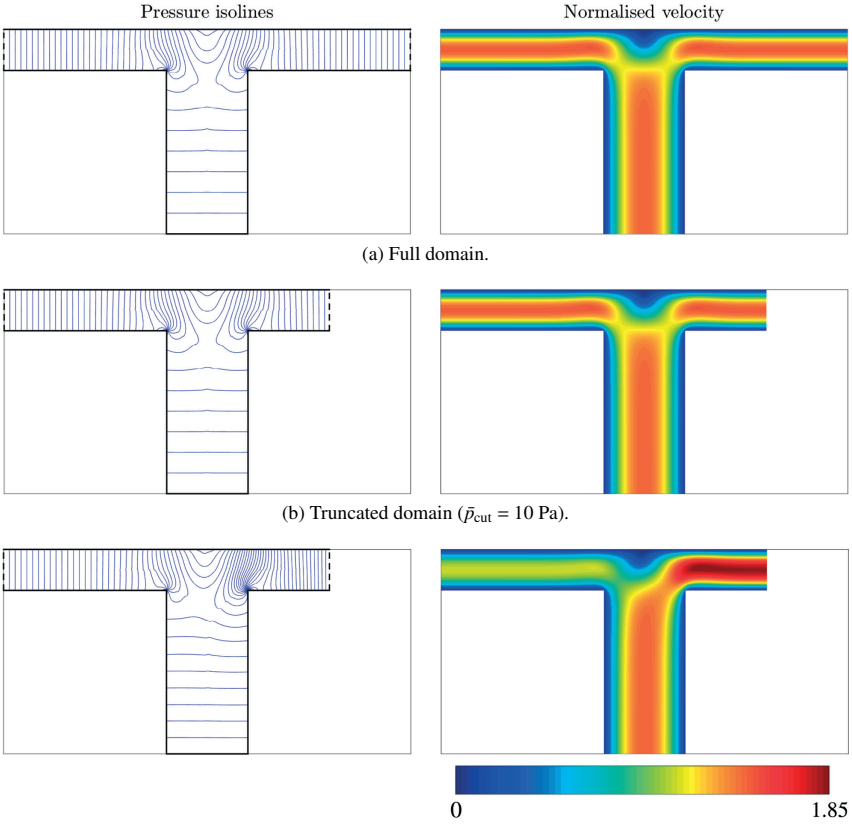

(a) Full domain.

(b) Truncated domain ($\bar{p}_{\text{cut}} = 10$ Pa).

(c) Truncated domain ($\bar{p}_{\text{cut}} = 0$).

Figure 4.9: Effect of mean pressure values in a domain with two outlets.

5 THE PRESSURE POISSON EQUATION

Before shifting the discussion from stable to *stabilised* flow solvers, we dedicate a chapter to the pressure Poisson equation (PPE), which is the main ingredient for the stabilisation methods we will later introduce. The original results presented in this chapter have been partially published: the weak pressure Poisson formulation for non-Newtonian fluids and corresponding numerical results are published in Ref. [67], while first numerical results on the ultra-weak formulation are reported in Ref. [68], with the complete analysis currently in preparation [69].

5.1 Strong problem

For concision, we restrict the presentation to the stationary setting, for which the momentum equation can be written as

$$\nabla p = \boldsymbol{r}(\boldsymbol{u}) := \boldsymbol{f} - (\rho \nabla \boldsymbol{u})\boldsymbol{u} + \nabla \cdot \mathbb{S}\,. \tag{5.1}$$

When $\boldsymbol{u}$ is known (e.g., from clinical imaging), we are left with what can be seen as an inverse problem to find the pressure field. In that case, (5.1) is an overdetermined system, as we have d equations and only one scalar unknown. Depending on the technique employed to solve this problem, different so-called *pressure estimators* arise [70]. The most popular one is the pressure Poisson equation, which we obtain by taking minus the divergence of both sides in (5.1), assuming enough regularity of all quantities involved. This yields

$$-\Delta p = -\nabla \cdot \boldsymbol{r} \;\text{ in }\; \Omega\,. \tag{5.2}$$

Pressure BCs are somewhat unnatural to incompressible flow problems and are usually not available. Fortunately, we can obtain an artificial (but consistent!) Neumann BC by dotting Eq. (5.1) by the normal $\boldsymbol{n}$ and restricting the result to Γ, giving us

$$\frac{\partial p}{\partial n} = \boldsymbol{n} \cdot \boldsymbol{r} \;\text{ on }\; \Gamma\,. \tag{5.3}$$

The Neumann problem (5.2)–(5.3) is solvable [44] because the right-hand side $f := -\nabla \cdot \boldsymbol{r}$ and the boundary datum $g := \boldsymbol{n} \cdot \boldsymbol{r}$ satisfy the compatibility condition

$$\int_{\Omega} f \,\mathrm{d}\Omega + \int_{\partial\Omega} g \,\mathrm{d}\Gamma = 0\,.$$

Thus, with the addition of a pressure scaling such as $\langle p,1\rangle_{L^2(\Omega)} = 0$, for uniqueness, we have a well-posed problem to write pressure in terms of velocities – whether they are given or part of the problem. Since the PPE is generated by differentiating a PDE which already had second-order velocity derivatives, the main underlying challenge is devising finite-element-suitable formulations without higher continuity requirements.

5.2 Weak formulation

Testing the PPE (5.2) with a function q and using Green's first formula on both sides leads to

$$\langle \nabla q, \nabla p\rangle_{L^2(\Omega)} - \langle q, \boldsymbol{n}\cdot\nabla p\rangle_{\Gamma} = \langle \nabla q, \boldsymbol{r}\rangle_{L^2(\Omega)} - \langle q, \boldsymbol{n}\cdot\boldsymbol{r}\rangle_{\Gamma}\,.$$

Substituting the Neumann boundary condition (5.3) leads to the weak form

$$\langle \nabla q, \nabla p\rangle_{L^2(\Omega)} = \langle \nabla q, \boldsymbol{f} - (\rho\nabla\boldsymbol{u})\boldsymbol{u} + \nabla\cdot\mathbb{S}\rangle_{L^2(\Omega)}\,, \tag{5.4}$$

which can be alternatively derived from the least-squares minimisation of $\|\nabla p - \boldsymbol{r}(\boldsymbol{u})\|_{L^2(\Omega)}$.

Notice that (5.4) is still not an "entirely weak" form, as we are left with the term $\nabla\cdot\mathbb{S}$ containing second-order derivatives of $\boldsymbol{u}$. However, it is possible to reduce the order of differentiation by using appropriate relations. Since $\Delta\boldsymbol{u} \equiv \nabla(\nabla\cdot\boldsymbol{u}) - \nabla\times(\nabla\times\boldsymbol{u})$ and $\nabla\cdot\boldsymbol{u} = 0$, we can write

$$\nabla\cdot\mathbb{S} = \mu[\Delta\boldsymbol{u} + \nabla(\nabla\cdot\boldsymbol{u})] + \left[\nabla\boldsymbol{u} + (\nabla\boldsymbol{u})^{\top}\right]\nabla\mu = \left[\nabla\boldsymbol{u} + (\nabla\boldsymbol{u})^{\top}\right]\nabla\mu - \mu\nabla\times(\nabla\times\boldsymbol{u})\,.$$

Integration by parts yields

$$-\langle \nabla q, \mu\nabla\times(\nabla\times\boldsymbol{u})\rangle_{L^2(\Omega)} = \langle \boldsymbol{n}\times\nabla q, \mu\nabla\times\boldsymbol{u}\rangle_{\Gamma} - \langle \nabla\times(\mu\nabla q), \nabla\times\boldsymbol{u}\rangle_{L^2(\Omega)}\,,$$

and for $q \in H^1(\Omega)$ we have

$$\begin{aligned}
-\langle \nabla\times(\mu\nabla q), \nabla\times\boldsymbol{u}\rangle_{L^2(\Omega)} &= \langle \nabla q\times\nabla\mu - \mu\overbrace{\nabla\times(\nabla q)}^{=\,\boldsymbol{0}}, \nabla\times\boldsymbol{u}\rangle_{L^2(\Omega)} \\
&= \langle \nabla q, \nabla\mu\times(\nabla\times\boldsymbol{u})\rangle_{L^2(\Omega)} \equiv \left\langle \nabla q, \left[(\nabla\boldsymbol{u})^{\top} - \nabla\boldsymbol{u}\right]\nabla\mu\right\rangle_{L^2(\Omega)}\,.
\end{aligned}$$

Therefore, the weak form of the PPE simplifies to

$$\langle \nabla q, \nabla p\rangle_{L^2(\Omega)} = \left\langle \nabla q, \boldsymbol{f} - (\rho\nabla\boldsymbol{u})\boldsymbol{u} + 2(\nabla\boldsymbol{u})^{\top}\nabla\mu\right\rangle_{L^2(\Omega)} + \langle \boldsymbol{n}\times\nabla q, \mu\nabla\times\boldsymbol{u}\rangle_{\Gamma}\,. \tag{5.5}$$

For a Newtonian fluid with $\nabla\mu \equiv \boldsymbol{0}$, only first-order derivatives remain and standard finite element spaces for both $\boldsymbol{u}$ and p can thus be employed [71]. When μ depends on $\nabla\boldsymbol{u}$, we proceed as in Chapter 4 and first project the viscosity onto a continuous space.

Sufficient regularity requirements

To guarantee unique solvability of (5.5), we can take test and trial functions in $H^1(\Omega) \cap L^2_0(\Omega)$, and accordingly $\boldsymbol{f} \in [L^2(\Omega)]^d$, with $L^2_0 := \{q \in L^2(\Omega) : \langle p, 1\rangle_{L^2(\Omega)} = 0\}$. As for the velocity, note that having $\boldsymbol{u} \in [H^1(\Omega)]^d$ does not guarantee $(\nabla \boldsymbol{u})\boldsymbol{u} \in [L^2(\Omega)]^d$. In fact, due to Hölder's inequality and the Sobolev embedding [57]

$$[H^1(\Omega)]^d \subset \left[L^m(\Omega)\right]^d, \text{ with } m \in [1,\infty) \text{ for } d = 2 \text{ and } m \in [1,6] \text{ for } d = 3,$$

this requirement is trivially satisfied by $\boldsymbol{u} \in [H^1(\Omega)]^d$ for $d = 2$, whereas for $d = 3$ we need additionally $\nabla \boldsymbol{u} \in [L^3(\Omega)]^{d\times d}$. Boundedness of the boundary term in (5.5) requires $\nabla \times \boldsymbol{u}|_\Gamma \in [H^{1/2}(\Gamma)]^{2d-3}$. Thus, for the Newtonian case, sufficient regularity is attained by choosing the velocity space X as

$$X = \begin{cases} \left\{\boldsymbol{u} \in \left[H^1(\Omega)\right]^2 \,:\, (\nabla \times \boldsymbol{u})|_\Gamma \in H^{1/2}(\Gamma)\right\}, & \text{if } d = 2, \\ \left\{\boldsymbol{u} \in \left[H^1(\Omega)\right]^3 \,:\, (\nabla \times \boldsymbol{u})|_\Gamma \in \left[H^{1/2}(\Gamma)\right]^3 \text{ and } \nabla \boldsymbol{u} \in \left[L^3(\Omega)\right]^{3\times 3}\right\}, & \text{if } d = 3. \end{cases}$$

For the non-Newtonian case, we further need $(\nabla \boldsymbol{u})^\top \nabla \mu \in [L^2(\Omega)]^d$. Since $\mu \in H^1(\Omega)$ by construction of the projected rheological law, we have $\nabla \mu \in [L^2(\Omega)]^d$, with the Hölder conjugate $(\nabla \boldsymbol{u})^\top \in [L^\infty(\Omega)]^{d\times d}$. Hence, an appropriate velocity space in that case is

$$X = \left\{\boldsymbol{u} \in \left[H^1(\Omega)\right]^d \,:\, (\nabla \times \boldsymbol{u})|_\Gamma \in \left[H^{1/2}(\Gamma)\right]^{2d-3} \text{ and } \nabla \boldsymbol{u} \in \left[L^\infty(\Omega)\right]^{d\times d}\right\}.$$

All the above requirements are fulfilled, say, by $\boldsymbol{u} \in [H^2(\Omega)]^d$. Fortunately, in the discrete case it suffices to use standard (continuous) Lagrangian finite elements [72], since the related gradients are piecewise polynomial and thus integrable to any positive power, including on $\partial\Omega$.

5.3 Ultra-weak formulations

A natural question arising from the discussion on sufficient regularity is: can we formulate the pressure Poisson problem with more standard regularity requirements on the flow quantities, in particular $p \in L^2(\Omega)$? The answer is *yes*, but, as we shall see, this comes at a price.

5.3.1 Unique solvability

To introduce the concept of *ultra-weak variational formulations*, let us consider the Poisson problem

$$-\Delta p = -\nabla \cdot \boldsymbol{r} \ \text{ in } \ \Omega, \tag{5.6}$$

$$\frac{\partial p}{\partial n} = \boldsymbol{n} \cdot \boldsymbol{r} \ \text{ on } \ \Gamma, \tag{5.7}$$

$$\int_\Omega p \, \mathrm{d}\Omega = 0\,. \tag{5.8}$$

We wish to obtain an ultra-weak solution $p \in L^2_0(\Omega)$ by solving the variational problem to find $p \in X := L^2(\Omega)$ such that

$$-\int_\Omega p\Delta\varphi \, \mathrm{d}\Omega + \int_\Omega p \, \mathrm{d}\Omega \int_\Omega \varphi \, \mathrm{d}\Omega = \int_\Omega \boldsymbol{r} \cdot \nabla\varphi \, \mathrm{d}\Omega \tag{5.9}$$

for all test functions φ in the space

$$Y = \left\{ q \in H^1_\Delta(\Omega) : \ \boldsymbol{n} \cdot \nabla q = 0 \ \text{ on } \ \partial\Omega \right\},$$

where $H^1_\Delta(\Omega) := \left\{ q \in H^1(\Omega) : \ \Delta q \in L^2(\Omega) \right\}$. The unique solvability of this ultra-weak variational formulation is based on an inf-sup stability condition for the bilinear form

$$a(p,\varphi) := -\int_\Omega p\Delta\varphi \, \mathrm{d}\Omega + \int_\Omega p \, \mathrm{d}\Omega \int_\Omega \varphi \, \mathrm{d}\Omega, \quad p \in X, \varphi \in Y.$$

While the norm for $p \in X$ is obvious, for $\varphi \in H^1(\Omega)$ an equivalent norm is given by

$$\|\varphi\|^2_{H^1(\Omega),\Omega} := \|\nabla\varphi\|^2_{L^2(\Omega)} + \frac{1}{|\Omega|}\left(\int_\Omega \varphi \, \mathrm{d}\Omega \right)^2 .$$

For $\varphi \in H^1_\Delta(\Omega)$ we therefore define the norm

$$\|\varphi\|^2_{H^1_\Delta(\Omega)} := \|\nabla\varphi\|^2_{L^2(\Omega)} + \frac{1}{|\Omega|}\left(\int_\Omega \varphi \, \mathrm{d}\Omega \right)^2 + \|\Delta\varphi\|^2_{L^2(\Omega)}\,.$$

Recalling Poincaré's inequality, for all $u \in H^1(\Omega)$ we have

$$\int_\Omega (u - u_\Omega)^2 \, \mathrm{d}\Omega \le c_P \int_\Omega |\nabla u|^2 \, \mathrm{d}\Omega, \ \text{ with } \ u_\Omega := \frac{1}{|\Omega|}\int_\Omega u \, \mathrm{d}\Omega, \tag{5.10}$$

which is equivalent to

$$\|u\|^2_{L^2(\Omega)} \le \frac{1}{|\Omega|}\left(\int_\Omega u \,\mathrm{d}\Omega\right)^2 + c_P\|\nabla u\|^2_{L^2(\Omega)}. \tag{5.11}$$

Now we can state an equivalent norm in $Y \subset H^1_\Delta(\Omega)$, namely,

$$\|\varphi\|^2_Y := \|\Delta\varphi\|^2_{L^2(\Omega)} + \frac{1}{|\Omega|}\left(\int_\Omega \varphi \,\mathrm{d}\Omega\right)^2.$$

Lemma 5.1. *For $\varphi \in Y \subset H^1_\Delta(\Omega)$ there hold the norm equivalence inequalities*

$$c_{\mathrm{eq}}\,\|\varphi\|^2_{H^1_\Delta(\Omega)} \le \|\varphi\|^2_Y \le \|\varphi\|^2_{H^1_\Delta(\Omega)}, \;\; \textit{with} \;\; c_{\mathrm{eq}} := \frac{1}{\max\left\{1 + c_P, 1 + c_P^{-1}\right\}}.$$

Proof. While the upper estimate is trivial, it remains to prove the lower bound. For $\varphi \in Y$ we have, when applying Green's first formula and using $\boldsymbol{n}\cdot\nabla\varphi = 0$ on Γ,

$$\begin{aligned}\|\nabla\varphi\|^2_{L^2(\Omega)} &= \int_\Omega \nabla\varphi\cdot\nabla\varphi \,\mathrm{d}\Omega = -\int_\Omega \varphi\Delta\varphi \,\mathrm{d}\Omega \\ &\le \|\Delta\varphi\|_{L^2(\Omega)}\|\varphi\|_{L^2(\Omega)}.\end{aligned}$$

Now, using Young's and Poincaré's (5.11) inequalities gives

$$\begin{aligned}\|\nabla\varphi\|^2_{L^2(\Omega)} \le \|\Delta\varphi\|_{L^2(\Omega)}\|\varphi\|_{L^2(\Omega)} &\le \frac{1}{2}c_P\,\|\Delta\varphi\|^2_{L^2(\Omega)} + \frac{1}{2c_P}\,\|\varphi\|^2_{L^2(\Omega)} \\ &\le \frac{1}{2}c_P\,\|\Delta\varphi\|^2_{L^2(\Omega)} + \frac{1}{2c_P}\left[\frac{1}{|\Omega|}\left(\int_\Omega \varphi \,\mathrm{d}\Omega\right)^2 + c_P\int_\Omega |\nabla\varphi|^2 \,\mathrm{d}\Omega\right],\end{aligned}$$

that is,

$$\|\nabla\varphi\|^2_{L^2(\Omega)} \le c_P\,\|\Delta\varphi\|^2_{L^2(\Omega)} + \frac{1}{c_P\,|\Omega|}\left(\int_\Omega \varphi \,\mathrm{d}\Omega\right)^2.$$

Hence,

$$\begin{aligned}
\|\varphi\|^2_{H^1_\Delta(\Omega)} &= \|\nabla\varphi\|^2_{L^2(\Omega)} + \frac{1}{|\Omega|}\left(\int_\Omega \varphi \,\mathrm{d}\Omega\right)^2 + \|\Delta\varphi\|^2_{L^2(\Omega)} \\
&\le \left(1+\frac{1}{c_P}\right)\frac{1}{|\Omega|}\left(\int_\Omega \varphi \,\mathrm{d}\Omega\right)^2 + (1+c_P)\,\|\Delta\varphi\|^2_{L^2(\Omega)} \\
&\le \max\left\{1+c_P, 1+\frac{1}{c_P}\right\}\left[\frac{1}{|\Omega|}\left(\int_\Omega \varphi \,\mathrm{d}\Omega\right)^2 + \|\Delta\varphi\|^2_{L^2(\Omega)}\right]
\end{aligned}$$

follows. □

For $(p,\varphi) \in X \times Y$ we now have

$$\begin{aligned}
a(p,\varphi) &= -\int_\Omega p\Delta\varphi \,\mathrm{d}\Omega + \int_\Omega p \,\mathrm{d}\Omega \int_\Omega \varphi \,\mathrm{d}\Omega \\
&\le \|p\|_{L^2(\Omega)}\|\Delta\varphi\|_{L^2(\Omega)} + \int_\Omega p \,\mathrm{d}\Omega \int_\Omega \varphi \,\mathrm{d}\Omega \\
&\le \sqrt{\|p\|^2_{L^2(\Omega)} + |\Omega|\left(\int_\Omega p \,\mathrm{d}\Omega\right)^2}\sqrt{\|\Delta\varphi\|^2_{L^2(\Omega)} + \frac{1}{|\Omega|}\left(\int_\Omega \varphi \,\mathrm{d}\Omega\right)^2} \\
&\le \|\varphi\|_Y \sqrt{\|p\|^2_{L^2(\Omega)} + |\Omega|^2 \int_\Omega p^2 \,\mathrm{d}\Omega} \\
&= \sqrt{1+|\Omega|^2}\,\|p\|_X\|\varphi\|_Y \,. \qquad (5.12)
\end{aligned}$$

We are now in position to state the unique solvability of the variational problem (5.9).

Theorem 5.2. *The function $p \in L^2(\Omega)$ is the unique solution of the extended variational formulation* (5.9) *satisfying the scaling condition* (5.8)*, i.e., $p \in L^2_0(\Omega)$.*

Proof. For $p \in L^2(\Omega)$ we consider the splitting

$$p = p_0 + \varrho, \;\text{ with }\; \varrho := \frac{1}{|\Omega|}\int_\Omega p \,\mathrm{d}\Omega \;\text{ and }\; \int_\Omega p_0 \,\mathrm{d}\Omega = 0\,,$$

where we have

$$\|p\|^2_{L^2(\Omega)} = \int_\Omega p^2 \,\mathrm{d}\Omega = \int_\Omega (p_0+\varrho)^2 \,\mathrm{d}\Omega = \int_\Omega {p_0}^2 \,\mathrm{d}\Omega + 2\varrho\int_\Omega p_0 \,\mathrm{d}\Omega + |\Omega|\,\varrho^2,$$

that is,

$$\|p\|^2_{L^2(\Omega)} = \|p_0\|^2_{L^2(\Omega)} + \frac{1}{|\Omega|}\left(\int_\Omega p \, \mathrm{d}\Omega\right)^2 .$$

Let $\varphi \in H^1(\Omega)$ be the unique weak solution of the Neumann boundary value problem

$$\begin{aligned} -\Delta\varphi &= p_0 \ \text{ in } \ \Omega, \\ \frac{\partial\varphi}{\partial n} &= 0 \ \text{ on } \ \Gamma, \\ \int_\Omega \varphi \, \mathrm{d}\Omega &= \varrho . \end{aligned}$$

Then,

$$\begin{aligned} a(p,\varphi) &= -\int_\Omega p\Delta\varphi \, \mathrm{d}\Omega + \int_\Omega p \, \mathrm{d}\Omega \int_\Omega \varphi \, \mathrm{d}\Omega \\ &= \int_\Omega (p_0 + \varrho)\, p_0 \, \mathrm{d}\Omega + \frac{1}{|\Omega|}\left(\int_\Omega p \, \mathrm{d}\Omega\right)^2 \\ &= \int_\Omega {p_0}^2 \, \mathrm{d}\Omega + \frac{1}{|\Omega|}\left(\int_\Omega p \, \mathrm{d}\Omega\right)^2 \\ &= \|p\|^2_{L^2(\Omega)} \end{aligned}$$

and

$$\begin{aligned} a(p,\varphi) &= \int_\Omega {p_0}^2 \, \mathrm{d}\Omega + \frac{1}{|\Omega|}\left(\int_\Omega p \, \mathrm{d}\Omega\right)^2 \\ &= \int_\Omega (-\Delta\varphi)^2 \, \mathrm{d}\Omega + |\Omega| \left(\int_\Omega \varphi \, \mathrm{d}\Omega\right)^2 \\ &\geq \min\{1, |\Omega|^2\} \, \|\varphi\|^2_Y \end{aligned}$$

imply $a(p,\varphi) \geq \min\{1,|\Omega|\} \, \|p\|_X \|\varphi\|_Y$, and therefore the inf-sup condition

$$\min\{1,|\Omega|\} \, \|p\|_X \leq \sup_{0\neq\varphi\in Y} \frac{a(p,\varphi)}{\|\varphi\|_Y} \quad \text{for all } p \in L^2(\Omega) \tag{5.13}$$

follows. On the other hand, for $0 \neq \varphi \in Y \subset H^1_\Delta(\Omega)$ we first compute

$$\alpha = \frac{1}{|\Omega|^2} \int_\Omega \varphi \, \mathrm{d}\Omega ,$$

and define $p = -\Delta\varphi + \alpha \in L^2(\Omega)$. For this particular choice we obtain

$$\begin{aligned} a(p,\varphi) &= \int_\Omega -p\Delta\varphi \,\mathrm{d}\Omega + \int_\Omega p \,\mathrm{d}\Omega \int_\Omega \varphi \,\mathrm{d}\Omega \\ &= \int_\Omega (-\Delta\varphi+\alpha)(-\Delta\varphi) \,\mathrm{d}\Omega + \int_\Omega (-\Delta\varphi+\alpha) \,\mathrm{d}\Omega \int_\Omega \varphi \,\mathrm{d}\Omega \\ &= \int_\Omega (\Delta\varphi)^2 \,\mathrm{d}\Omega + \frac{1}{|\Omega|}\left(\int_\Omega \varphi \,\mathrm{d}\Omega\right)^2 \\ &= \|\varphi\|_Y^2 > 0, \end{aligned}$$

where we have used

$$\int_\Omega \Delta\varphi \,\mathrm{d}\Omega = \int_\Gamma \frac{\partial\varphi}{\partial n} \,\mathrm{d}\Gamma = 0 \quad \text{for } \varphi \in Y.$$

Hence we have that all assumptions of the Babuška–Brezzi theorem are satisfied [73], and therefore unique solvability of (5.9) follows. In particular for $\varphi \equiv 1$ we finally conclude the scaling condition (5.8). □

5.3.2 Generalised Newtonian fluids

Now that the unique solvability of the ultra-weak Poisson problem has been shown, we can return to the particular problem of the PPE. In that case, we have the ultra-weak Petrov–Galerkin problem to find $p \in L^2(\Omega)$ such that

$$\begin{aligned} -\langle \Delta q, p\rangle_{L^2(\Omega)} + \langle q,1\rangle_{L^2(\Omega)}\langle p,1\rangle_{L^2(\Omega)} = \\ \left\langle \nabla q, \boldsymbol{f} - (\rho\nabla\boldsymbol{u})\boldsymbol{u} + 2(\nabla\boldsymbol{u})^\top\nabla\mu\right\rangle_\Omega + \langle \boldsymbol{n}\times\nabla q, \mu\nabla\times\boldsymbol{u}\rangle_\Gamma \end{aligned} \tag{5.14}$$

for all $q \in Y = \left\{q \in H^1_\Delta(\Omega) : \ \boldsymbol{n}\cdot\nabla q = 0 \ \text{ on } \ \partial\Omega\right\}$. Shifting all derivatives from p to q allows discontinuous pressure but leads to a higher regularity requirement for the test space. In practice, we will need to construct test functions with continuous derivatives. While this is not a simple task in complex geometries, constructing C^1 *test* functions is somewhat simpler than doing it for *trial* functions, since in principle no approximation properties are needed of test spaces. When appropriately handled, the pressure Poisson equation can be a highly versatile tool in computational fluid dynamics. It can be used to compute pressure directly from given velocity fields, as is the focus of this chapter, but also to design accurate stabilisation methods and highly efficient solvers for incompressible flow problems, as presented in Chapters 6 and 7.

5.3.3 Compressible flows

Although our focus lies on incompressible flows, we briefly present now an extension of the PPE to compute pressure from compressible flow velocities. In that case, we have

$$\mathbb{S} = 2\mu\nabla^s \boldsymbol{u} - (2\mu\nabla\cdot\boldsymbol{u}/3)\,\mathbb{I}, \tag{5.15}$$

where $\mathbb{I}$ denotes the $d \times d$ identity tensor. Hence,

$$\begin{aligned}
\langle \nabla q, \nabla\cdot\mathbb{S}\rangle_\Omega &= \left\langle \mu\boldsymbol{n}\otimes\nabla q, 2\nabla^s\boldsymbol{u} - \left(\frac{2}{3}\nabla\cdot\boldsymbol{u}\right)\mathbb{I}\right\rangle_\Gamma - \left\langle \mu\nabla(\nabla q), 2\nabla^s\boldsymbol{u} - \left(\frac{2}{3}\nabla\cdot\boldsymbol{u}\right)\mathbb{I}\right\rangle_{L^2(\Omega)} \\
&= \langle \nabla q, (2\mu\nabla^s\boldsymbol{u})\boldsymbol{n}\rangle_\Gamma - \frac{2}{3}\left\langle \frac{\partial q}{\partial n}, \mu\nabla\cdot\boldsymbol{u}\right\rangle_\Gamma - \left\langle \mu\nabla(\nabla q), 2\nabla^s\boldsymbol{u} - \left(\frac{2}{3}\nabla\cdot\boldsymbol{u}\right)\mathbb{I}\right\rangle_{L^2(\Omega)} \\
&= \langle \nabla q, (2\mu\nabla^s\boldsymbol{u})\boldsymbol{n}\rangle_\Gamma - \langle \nabla(\nabla q), 2\mu\nabla^s\boldsymbol{u}\rangle_{L^2(\Omega)} - \frac{2}{3}\langle \Delta q, \mu\nabla\cdot\boldsymbol{u}\rangle_{L^2(\Omega)},
\end{aligned}$$

since we take test functions with zero normal derivative on Γ. So, compressibility basically adds an extra term to the right-hand side of the PPE. The key difference lies actually on the density, which for a compressible flow is no longer a given parameter, but one of the flow variables. In fact, we can compute the density from the velocities through the continuity equation $\nabla\cdot(\rho\boldsymbol{u}) = 0$, which is a linear hyperbolic equation requiring the inflow density as boundary condition [58]. The computed density field is then used as input for the PPE.

5.3.4 Discretisation

As already mentioned, the main challenge in ultra-weak methods is constructing test functions with continuous derivatives. We now give a few examples of appropriate test spaces for piecewise constant as well as continuous, piecewise linear pressure discretisations. Of course, the test and trial spaces must fulfill a discrete inf-sup condition to guarantee unique solvability of the finite element formulation. This is discussed in Ref. [69].

Discontinuous pressure spaces

When using piecewise constant functions for the pressure approximation, it is sensible to seek quadratic or d-quadratic test functions with local support and continuous derivatives. Let us consider an interval $\Omega \subset \mathbb{R}$ divided into N segments $s_i = [x_i, x_{i+1}]$. We can construct modified B-splines $B_i(x)$ by assuming a second-order polynomial expression within each segment s_i, local support and the conditions

- $B_i(x)$ and $[B_i(x)]'$ continuous at all knots x_j,
- $[B_i(x)]' = 0$ on $\partial\Omega$,

- $\sum_{i=1}^{N} B_i(x) \equiv 1$.

Figure 5.1 illustrates the resulting functions for $N = 4$. The discrete inf-sup condition for the ultra-weak Poisson formulation with these modified one-dimensional B-splines and piecewise constant *Ansatz* is provided in Ref. [69]. For $d = 2$ or 3, the actual test functions are formed by the tensor product of the one-dimensional splines, as illustrated in Figure 5.2 for the two-dimensional case. Since the trial space consists of functions that take a constant unit value within one element and zero elsewhere, the entries of the stiffness matrix $\mathbf{K}$ become

$$K_{ij} = -\int_{\Omega_j} \Delta q_i \, \mathrm{d}\Omega + |\Omega_j| \int_{\Omega} q_i \, \mathrm{d}\Omega . \tag{5.16}$$

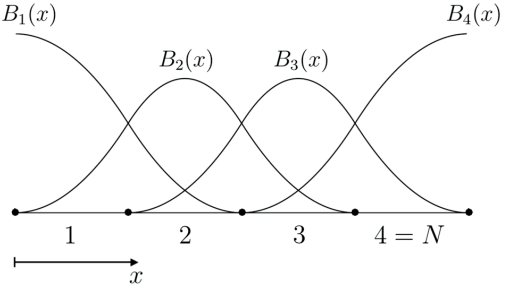

Figure 5.1: Modified one-dimensional B-splines with zero Neumann trace.

If a tensor-product discretisation is only possible patch-wise, one can relax the global C^1 continuity of the test functions. This can be done by considering separate subproblems in each patch, with possible interface conditions weakly enforced. To illustrate that, let us consider a problem with two subdomains Ω_L and Ω_R and two Poisson subproblems:

$$\begin{aligned} -\Delta p_L &= -\nabla \cdot \boldsymbol{r} \ \text{ in } \ \Omega_L, \\ \frac{\partial p_L}{\partial n_L} &= \boldsymbol{n}_L \cdot \boldsymbol{r} \ \text{ on } \ \partial\Omega_L \cap \partial\Omega, \\ p_L &= p_R \ \text{ on } \ \partial\Omega_L \cap \partial\Omega_R, \end{aligned} \qquad \left| \qquad \begin{aligned} -\Delta p_R &= -\nabla \cdot \boldsymbol{r} \ \text{ in } \ \Omega_R, \\ \frac{\partial p_R}{\partial n_R} &= \boldsymbol{n}_R \cdot \boldsymbol{r} \ \text{ on } \ \partial\Omega_R, \\ \int_{\Omega_R} p_R \, \mathrm{d}\Omega &= 0. \end{aligned} \right.$$

Note that, for the left subdomain Ω_L, the PPE is no longer a pure Neumann problem. Therefore, on the interface $\partial\Omega_L \cap \partial\Omega_R$ the test functions of Ω_L will have a zero Dirichlet (rather than Neumann) trace. The interface continuity ($p_L = p_R$ on $\partial\Omega_L \cap \partial\Omega_R$) will then

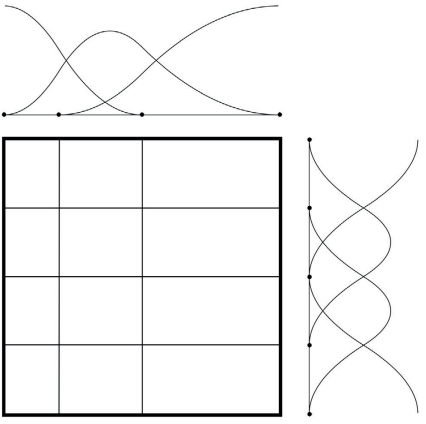

Figure 5.2: Example of the tensor-product test space in a 3×4 rectangular mesh.

be enforced weakly and naturally. In other words, the ultra-weak subproblems are to find $(p_L,p_R) \in L^2(\Omega_L) \times L^2(\Omega_R)$ such that for all $(q_L,q_R) \in Y_L \times Y_R$ we have

$$-\langle \Delta q_L, p_L \rangle_{L^2(\Omega_L)} + \left\langle \frac{\partial q_L}{\partial n_L}, p_R \right\rangle_{\partial\Omega_L \cap \partial\Omega_R} = \langle \nabla q_L, \boldsymbol{f} - (\rho \nabla \boldsymbol{u})\boldsymbol{u} \rangle_{\Omega_L} + \langle \boldsymbol{n}_L \times \nabla q_L, \mu \nabla \times \boldsymbol{u} \rangle_{\partial\Omega_L},$$
$$-\langle \Delta q_R, p_R \rangle_{L^2(\Omega_R)} + \langle q_R, 1 \rangle_{\Omega_R} \langle p_R, 1 \rangle_{\Omega_R} = \langle \nabla q_R, \boldsymbol{f} - (\rho \nabla \boldsymbol{u})\boldsymbol{u} \rangle_{\Omega_R} + \langle \boldsymbol{n}_R \times \nabla q_R, \mu \nabla \times \boldsymbol{u} \rangle_{\partial\Omega_R},$$

where

$$Y_L = \left\{ q \in H^1_\Delta(\Omega_L) : \boldsymbol{n}_L \cdot \nabla q = 0 \text{ on } \partial\Omega_L \cap \partial\Omega \text{ and } q = 0 \text{ on } \partial\Omega_L \cap \partial\Omega_R \right\},$$
$$Y_R = \left\{ q \in H^1_\Delta(\Omega_R) : \boldsymbol{n}_R \cdot \nabla q = 0 \text{ on } \partial\Omega_R \right\}.$$

Note that the boundary term on the left-hand side of the first variational problem comes from the second integration by parts, enforcing the interface continuity (Dirichlet BC) weakly. At the discrete level, the test functions q_L must be modified to have zero Dirichlet trace and *nonzero* Neumann trace on the interface. Figure 5.3 illustrates the corresponding test functions for an example with $\Omega_L = (0,1/2) \times (1/2,1)$ and $\Omega_R = (1/2,1) \times (0,1)$.

Continuous pressure spaces

As seen in Section 5.2, for incompressible Newtonian flows it is possible to use a reduced (curl-curl) form of the stress divergence to obtain

$$\int_\Omega \nabla q \cdot \nabla p \, \mathrm{d}\Omega = \int_\Omega \nabla q \cdot [\boldsymbol{f} - (\rho \nabla \boldsymbol{u})\boldsymbol{u}] \, \mathrm{d}\Omega + \int_{\partial\Omega} (\boldsymbol{n} \times \nabla q) \cdot (\mu \nabla \times \boldsymbol{u}) \, \mathrm{d}\Gamma.$$

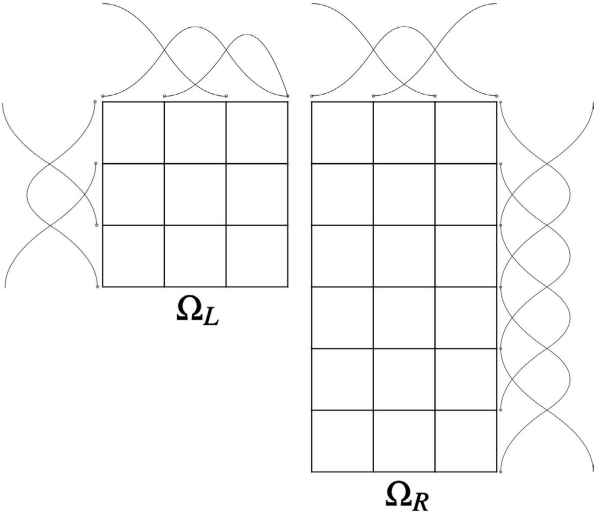

Figure 5.3: Example of the decomposition and discretisation of an L-shaped domain.

Thus, using an ultra-weak formulation in this case is only needed if discontinuous pressure spaces (or a less regular right-hand side) are desired. However, when either compressibility or non-uniform viscous behaviour is present, the curl-curl form of the viscous term no longer holds, so that it may be necessary to employ an ultra-weak formulation even when assuming continuous pressure. In fact, the most general form of the viscous term is

$$\langle \nabla q, (2\mu\nabla^s \boldsymbol{u})\boldsymbol{n}\rangle_\Gamma - \langle \nabla(\nabla q), 2\mu\nabla^s \boldsymbol{u}\rangle_{L^2(\Omega)} - \frac{2}{3}\langle \Delta q, \mu\nabla\cdot\boldsymbol{u}\rangle_{L^2(\Omega)} + \frac{2}{3}\left\langle \frac{\partial q}{\partial n}, \mu\nabla\cdot\boldsymbol{u}\right\rangle_\Gamma , \quad (5.17)$$

which contains second-order derivatives of the test function q. The question is then how to construct a discrete test space for continuous pressure spaces such as with piecewise linear or d-linear shape functions. For a d-linear tensor-product mesh, tensor-product Hermite polynomials can be used for the test space. Their support is the same as that of the trial space, and C^1 mappings can be constructed for non-Cartesian grids [74, 75].

A more interesting case is that of linear simplicial elements, since they allow more flexibility in meshing. Let us consider triangular elements with continuous, piecewise linear basis functions for the pressure trial space. Then, at the element level, we need three linearly independent test functions. Furthermore, zero Neumann trace is desirable for the test functions in order to get rid of the boundary terms arising from the second integration by parts. As a matter of fact, in the context of bi-harmonic plate problems there is a well-known fam-

ily of functions satisfying these properties. The so-called Argyris triangle has twenty-one C^1-conforming basis functions related to vertex displacements, vertex first- and second-order derivatives and mid-edge normal derivatives. These twenty-one functions form a basis of the space of fifth-order polynomials in each triangle. Fortunately, in our case we only need three of those, namely, the displacement basis functions. Apart from C^1 continuity, they fulfil the partition of unit and nodal delta Kronecker property, besides having zero normal derivatives on element edges, which eliminates the last term in Eq. (5.17). In the next section we provide an example considering such test functions, whose efficient implementation can be constructed according to Ref. [76]. Unfortunately, to the best of our knowledge there is no natural extension of the Argyris space to three dimensions, and the robust construction of C^1 finite element spaces in general three-dimensional meshes is still focus of intense investigation [75].

5.4 Numerical examples

The accuracy of different PPE versions will now be assessed via various numerical examples. In all cases, the given velocities are interpolated by standard finite element spaces.

Power-law fluid through straight channel

We start with the power-law flow benchmark (see Subsection 4.3), now in a square channel with a 1 mm edge. The pressure spaces for the weak and ultra-weak methods are taken as Q_1 and Q_0, respectively, whereas the analytical velocity profile from Eq. (4.9) is interpolated using bilinear (Q_1) or biquadratic (Q_2) elements. The coarsest mesh is composed by 4×4 identical squares, and five levels of uniform refinement are applied. The convergence plot in Figure 5.4 provides important results. When using a first-order interpolation for the given velocity, the convergence is linear regardless of the order of the pressure space. Therefore, the ultra-weak formulation can reduce the computational cost by allowing piecewise constant pressures and eliminating the need for the viscosity projection step.

Carreau–Yasuda fluid past a backward-facing step

We consider once again the classical backward-facing step benchmark. The domain has the same proportions as in Figure 4.6, with inflow channel height $H = 5$ mm. As done by Masud and Kwack [36], we use the Carreau–Yasuda model (4.15) with representative hemodynamic parameters $\rho = 1060$ kg/m^3, $\mu_\infty = 3.45$ mPa·s, $\mu_0 = 56$ mPa·s, $n = 0.22$, $\lambda = 1.902$ s and $a = 1.25$. Since no analytical solution is known, we perform a full flow simulation at Re = 25 using a stabilised solver (see Chapter 6) on a uniform mesh with

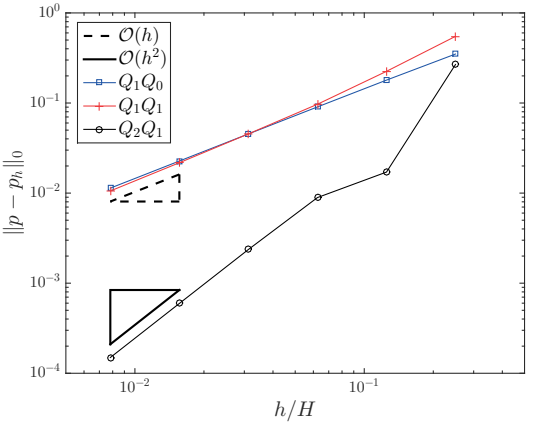

Figure 5.4: Pressure Poisson equation: convergence for different velocity-pressure pairs.

5×10^4 bilinear square elements. The resulting velocity field is then used to feed the ultra-weak PPE with constant pressure elements. The comparison between pressures yielded by the full simulation and the PPE is shown in Figure 5.5. Very good agreement is observed, and in particular the PPE with piecewise constant pressure approximation seems to capture the corner-induced discontinuity more accurately than the continuous pressure elements, where some oscillation can be seen upstream of the corner ($x_1 = 4H$).

Manufactured compressible flow solution

We now test the compressible version of the ultra-weak PPE by considering a compressible flow accelerating through a straight channel $\Omega = (0,3) \times (0,1)$ due to a body force

$$\boldsymbol{f} = \begin{pmatrix} e^{x_1}\left[x_2\left(1-x_2\right)\right]^2 \\ \left(4x_1 - 1\right)\left(1 - 2x_2\right)/3 \end{pmatrix}.$$

Setting a constant dynamic viscosity $\mu \equiv 1$, a mass flow rate per unit width equal to $1/6$ and an inlet density $\rho(0,x_2) \equiv 1$ results in

$$\boldsymbol{u} = \begin{pmatrix} x_2(1-x_2)e^{x_1} \\ 0 \end{pmatrix}, \quad p = \frac{20 - x_1\left(4{x_2}^2 - 4x_2 + 6\right)}{3} \quad \text{and} \quad \rho = e^{-x_1}.$$

Two types of discretisation are considered: quadrilateral elements with piecewise constant pressure and blinear velocity, and triangular elements with linear pressure and quadratic

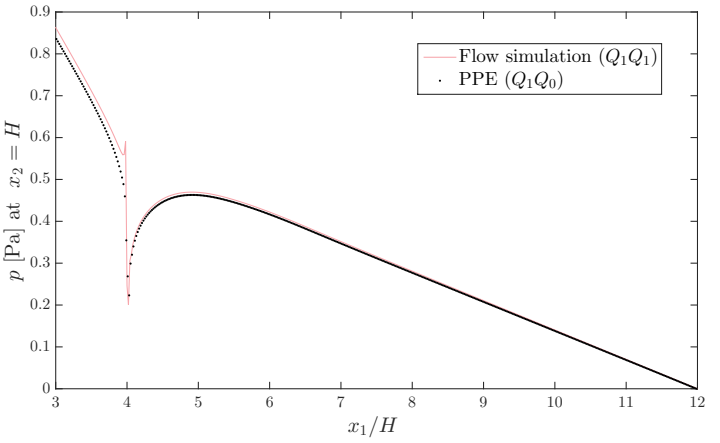

Figure 5.5: Backward-facing step: pressure computed by the PPE with Q_1Q_0 elements.

velocity (and quintic Argyris test functions). First-order spaces are used for the density in both cases. The coarsest mesh for each case is shown in Figure 5.6. The uniform refinement study depicted in Figure 5.7 reveals optimal convergence for both element types.

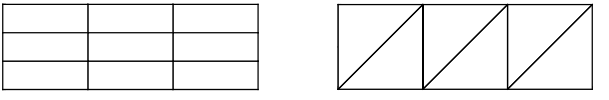

Figure 5.6: Coarsest meshes used for the compressible PPE test case.

In vitro flow in intracranial aneurysm phantom

As a last example, we consider a typical biomedical application of the PPE: reconstructing pressure from magnetic resonance imaging (MRI) flow measurements. For this test, we use the data obtained by Amili et al. [77] considering a giant aneurysm phantom that was 3D-printed from a patient-specific geometry. The data are originally voxelated: at each acquisition time, the velocity field is given at nodes forming a uniform tensor-product grid in space. So, we must first eliminate the grid points lying outside the aneurysm to retain only the ones with valid acquisitions. Then, from the remaining nodes (i.e., inside

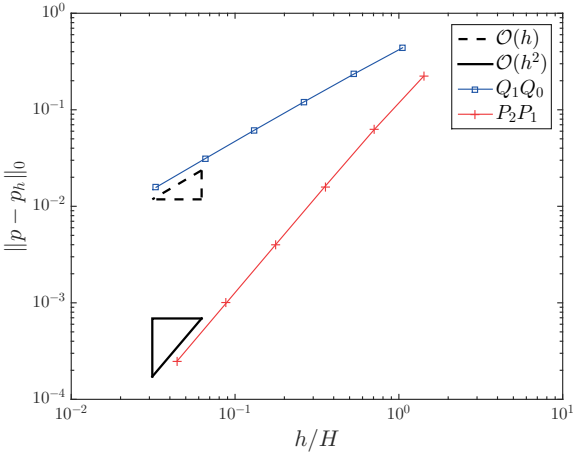

Figure 5.7: Error plot for the pressure computed through the ultra-weak compressible PPE.

the aneurysm), we create a hexahedral mesh (see Figure 5.8). Amili et al. [77] used a Newtonian fluid with $\rho = 1060$ kg/m^3 and $\mu = 2.12$ mPa·s, and 16 velocity samples within a pulsation period of $T = 7.92$ s. The cycle-averaged velocity magnitude is shown in Figure 5.8, where we see a high-speed region due to a proximal stenosis at the parent artery (refer to the original work [77] for geometric details). From the velocity measurements, we reconstruct the pressure field using the weak Q_1Q_1 pressure Poisson equation, then compute the mean pressure drop

$$\delta p(t) := \frac{1}{|\Gamma_{\text{in}}|} \int_{\Gamma_{\text{in}}} p \, \mathrm{d}\Gamma - \frac{1}{|\Gamma_{\text{out}}|} \int_{\Gamma_{\text{out}}} p \, \mathrm{d}\Gamma .$$

We compare our results to those by Amili et al. [77], who used finite differences to compute second-order derivatives [78]. Figure 5.9 shows a good agreement between the computations, especially in estimating the peak systolic pressure. The cycle-averaged pressure field is depicted in Figure 5.10, which allows the identification of critical high-pressure regions.

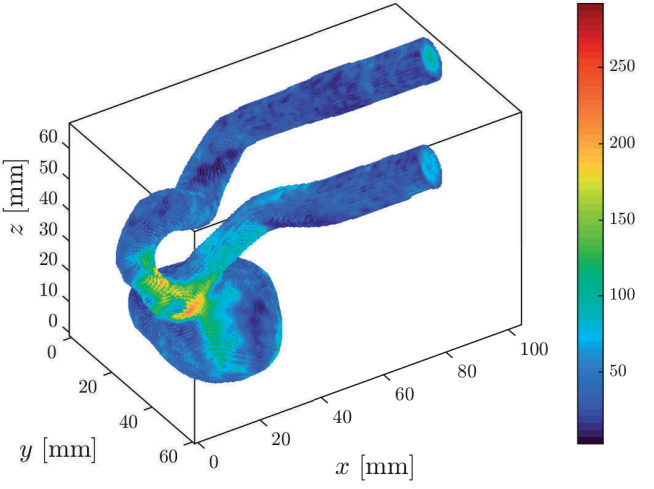

Figure 5.8: Giant intracranial aneurysm: cycle-averaged velocity magnitude (mm/s) from the *in vitro* experiment by Amili et al. [77] (phase-contrast MRI).

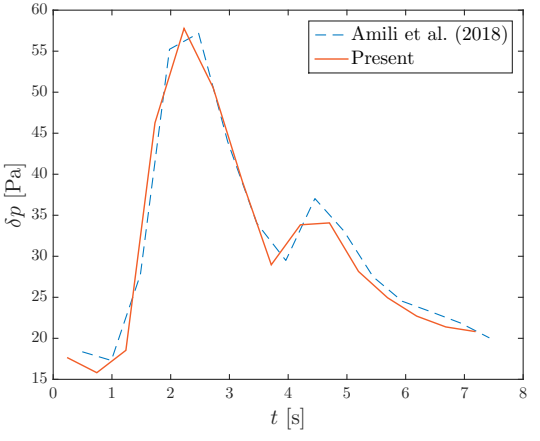

Figure 5.9: Giant intracranial aneurysm: mean pressure drop from inlet to outlet.

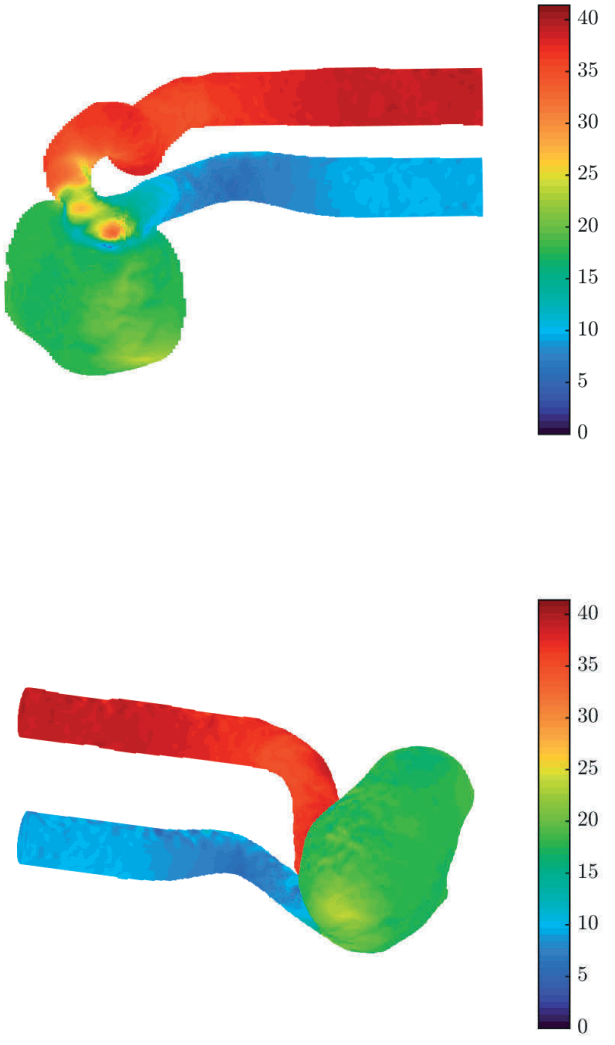

Figure 5.10: Giant intracranial aneurysm: cycle-averaged pressure field (in Pa) reconstructed using the weak PPE with Q_1Q_1 elements.

6 STABILISED FINITE ELEMENT FORMULATIONS

In this chapter, we devise a stabilised finite element framework based on the pressure Poisson formulation presented in the previous chapter. The corresponding results have been partially published: the stabilisation method for stationary Newtonian flows is published in Ref. [79], whereas the extension to non-Newtonian, time-dependent flows is reported in Ref. [80]. A report on the initial higher-order convergence in equal-order methods, as well as corresponding numerical results, is currently in preparation [81].

6.1 Some classical methods and their limitations

As already mentioned, the standard mixed finite element problem for the incompressible Navier–Stokes equations, Newtonian or not, is unstable when the pressure and velocity spaces are the same. The first stabilisation method allowing equal-order pairs was presented by Brezzi and Pitkäranta [23] and consists of relaxing the continuity equation as

$$\int_\Omega q_h \nabla\cdot\boldsymbol{u}_h \,\mathrm{d}\Omega + \alpha \sum_{e=1}^{N_e} \int_{\Omega_e} \frac{{h_e}^2}{\mu} \nabla q_h \cdot \nabla p_h \,\mathrm{d}\Omega = 0\,, \tag{6.1}$$

where α is a positive parameter. This breaks the saddle-point structure of the Navier–Stokes system and therefore eliminates the need for LBB compatibility. The stabilisation factor α must be selected within an appropriate range to guarantee the coercivity of the overall discrete problem and lead to stable and convergent approximations. Notice that Eq. (6.1) is the weak form of the problem

$$\begin{aligned} -\alpha\nabla\cdot\left(h^2\mu^{-1}\nabla p\right) + \nabla\cdot\boldsymbol{u} &= 0 \ \text{ in } \ \Omega\,, \\ \frac{\partial p}{\partial n} &= 0 \ \text{ on } \ \Gamma\,, \end{aligned}$$

that is, the stabilisation can be seen as constructed from a completely artificial Poisson problem for the pressure. While this is not an issue for stability, the accuracy is definitely compromised. In particular, the artificial Neumman condition induces spurious pressure boundary layers that degrade the order of approximation close to the boundary [82]. This can be fixed if the stabilisation term is made *consistent* by using the residual of the momentum equation, as proposed by Hughes et al. [5] in their so-called pressure-stabilised

Petrov–Galerkin (PSPG) formulation:

$$\int_\Omega q_h \nabla \cdot \boldsymbol{u}_h \, \mathrm{d}\Omega + \sum_{e=1}^{N_e} \int_{\Omega_e} \delta_h \nabla q_h \cdot \{\nabla p_h + \rho[\partial_t \boldsymbol{u}_h + (\nabla \boldsymbol{u}_h)\boldsymbol{u}_h] - \nabla \cdot \mathbb{S}_h - \boldsymbol{f}\} \, \mathrm{d}\Omega = 0, \quad (6.2)$$

in which δ_h can be taken as proportional to ${h_e}^2$ or h_e in low- or high-Reynolds flows, respectively [83]. This is in principle a consistent formulation, since the added stabilisation term should vanish for the exact solution. However, when using linear elements, the velocity gradient and the viscous stress are piecewise constant, so that

$$\sum_{e=1}^{N_e} \int_{\Omega_e} \delta_h \nabla q_h \cdot (\nabla \cdot \mathbb{S}_h) \, \mathrm{d}\Omega = \sum_{e=1}^{N_e} \int_{\Omega_e} \delta_h \nabla q_h \cdot \mathbf{0} \, \mathrm{d}\Omega = 0,$$

that is, the viscous part of the residual is completely lost. This means that the residual itself will never vanish, so the consistency of the method relies solely on the stabilisation parameter δ_h being proportional to some positive power of h_e. This incomplete residual can spoil coarse grid accuracy and restrict the choice of the stabilisation parameter [84, 85], especially for diffusion-dominated flows. In fact, this is an issue appearing not only in PSPG, but also in most residual-based stabilisation techniques such as Galerkin-least-squares (GLS) [6], VMS [33] and others [86, 87]. It is thus common practice to use projection-based techniques such as the ones proposed by Jansen et al. [85] and Bochev and Gunzburger [88] to reconstruct the viscous term [32, 89].

Another simple technique to eliminate the inconsistency of low-order residual-based methods was proposed by Codina and Blasco [90, 91]. Their method is similar to the original one by Brezzi and Pitkäranta [23], but replaces the full pressure gradient in the stabilisation term by gradient fluctuations [92]:

$$\int_\Omega q_h \nabla \cdot \boldsymbol{u}_h \, \mathrm{d}\Omega + \alpha \sum_{e=1}^{N_e} \int_{\Omega_e} \frac{{h_e}^2}{\mu} \nabla q_h \cdot \left(\nabla p_h - \overline{\nabla p_h}\right) \mathrm{d}\Omega, \quad (6.3)$$

where $\overline{\nabla p_h}$ is the L^2 projection of the pressure gradient onto the unconstrained velocity space. The perturbation added to the continuity equation is consistent, as the fluctuation $\nabla p - \overline{\nabla p}$ is zero for smooth solutions of the continuous problem. Hence, this method eliminates spurious pressure boundary layers, but at the rather high cost of a global vector projection. More efficient stabilisation methods can be constructed by employing local projection operators [25, 93, 94]. Another family of stabilisation techniques requiring only first-order derivatives are continuous interior penalty methods using jump-based stabilisation terms [82, 95]. The main shortcoming of such methods is the need for face-based data structures and implementation, which are not always available.

It is important to note that the type of stabilisation to which we herein refer is not to be confused with other residual-based techniques such as streamline upwind Petrov–Galerkin (SUPG) [96], grad-div [97, 98] or artificial diffusion [99]. Those methods aim to remedy other sources of instability and can be appropriately combined with the present one for specific flow problems and regimes. As a matter of fact, the SUPG technique employed for stabilising convective effects also suffers from an incomplete residual evaluation in the lowest-order case. Nonetheless, in the flow regimes for which SUPG is actually important, the viscous terms typically have a minor contribution in the residual, so that the vanishing stress divergence is not a critical issue. Therefore, the present work focuses on – while not being limited to – the diffusion-dominated case. To get a broader overview of finite element pressure stabilisations for incompressible flow problems, see Refs. [100, 101].

6.2 A fully consistent stabilisation method for elements with continuous pressure

Given the limitations of standard pressure stabilisations and the typical pressure-Poisson-like structure of most of them, it is quite natural to wonder whether consistent pressure Poisson formulations such as the ones introduced in Chapter 5 can be used for stabilising equal-order incompressible flow solvers. To answer that, and inspired by ideas often present in split-step methods [71, 72, 102–109], we propose replacing the standard momentum-mass system by an equivalent one. For concision, we stick to the stationary case and drop body forces, but the extension to the general setting is straightforward. The proposed system reads

$$(\rho\nabla\boldsymbol{u})\boldsymbol{u} - \mu\Delta\boldsymbol{u} - 2\nabla^s\boldsymbol{u}\nabla\mu + \nabla p = \boldsymbol{0} \quad \text{in } \Omega, \tag{6.4}$$

$$-\Delta p = \nabla\cdot\left[(\rho\nabla\boldsymbol{u})\boldsymbol{u} - 2\nabla^s\boldsymbol{u}\nabla\mu\right] + \left[\nabla\times(\nabla\times\boldsymbol{u})\right]\cdot\nabla\mu - \beta\nabla\cdot\boldsymbol{u} \quad \text{in } \Omega, \tag{6.5}$$

$$\frac{\partial p}{\partial n} = \boldsymbol{n}\cdot\left[2\nabla^s\boldsymbol{u}\nabla\mu - (\rho\nabla\boldsymbol{u})\boldsymbol{u} - \mu\nabla\times(\nabla\times\boldsymbol{u})\right] \quad \text{on } \Gamma, \tag{6.6}$$

where β is some given positive function to be defined later. The velocity BCs were omitted because they play no role in the following discussion.

Lemma 6.1. *System* (6.4)–(6.6) *implies the standard momentum-mass system* (3.1)–(3.2).

Proof. The first step is to apply the divergence operator to Eq. (6.4), leading to

$$\begin{aligned}\Delta p &= \nabla\cdot\left[\mu\Delta\boldsymbol{u} + 2\nabla^s\boldsymbol{u}\nabla\mu - (\rho\nabla\boldsymbol{u})\boldsymbol{u}\right]\\ &= \nabla\cdot\left[2\nabla^s\boldsymbol{u}\nabla\mu - (\rho\nabla\boldsymbol{u})\boldsymbol{u}\right] + \nabla\mu\cdot\Delta\boldsymbol{u} + \mu\nabla\cdot(\Delta\boldsymbol{u}),\end{aligned} \tag{6.7}$$

which when added to Eq. (6.5) gives

$$\begin{aligned}0 &= \left[\nabla\times(\nabla\times\boldsymbol{u})\right]\cdot\nabla\mu - \beta\nabla\cdot\boldsymbol{u} + \nabla\mu\cdot\Delta\boldsymbol{u} + \mu\nabla\cdot(\Delta\boldsymbol{u})\\ &= \mu\nabla\cdot(\Delta\boldsymbol{u}) + \nabla\mu\cdot\left[\Delta\boldsymbol{u} + \nabla\times(\nabla\times\boldsymbol{u})\right] - \beta\nabla\cdot\boldsymbol{u},\end{aligned} \tag{6.8}$$

but $\Delta\boldsymbol{u} + \nabla\times(\nabla\times\boldsymbol{u}) \equiv \nabla(\nabla\cdot\boldsymbol{u})$ and $\nabla\cdot(\Delta\boldsymbol{u}) \equiv \Delta(\nabla\cdot\boldsymbol{u})$. Therefore, introducing $\phi := \nabla\cdot\boldsymbol{u}$, we get the diffusion-reaction equation

$$-\nabla\cdot(\mu\nabla\phi) + \beta\phi = 0\,. \tag{6.9}$$

We can obtain Neumann BCs for this equation by dotting Eq. (6.4) with $\boldsymbol{n}$, restricting the result to Γ and substracting it from (6.6), which gives

$$\begin{aligned} 0 &= \boldsymbol{n}\cdot[\Delta\boldsymbol{u} + (\nabla\times\nabla\times\boldsymbol{u})] \\ &= \boldsymbol{n}\cdot[\nabla(\nabla\cdot\boldsymbol{u})] \\ &= \frac{\partial\phi}{\partial n} \;\text{ on }\; \Gamma\,. \end{aligned} \tag{6.10}$$

The solution of Eq. (6.9) is thus $\phi \equiv 0$, that is, $\nabla\cdot\boldsymbol{u} = 0$ in Ω, as we wanted. Now that incompressibility has been proved, the equivalence between Eqs. (6.4) and (3.1) is straightforward. □

Proving the other side of the equivalence is simpler, since the PPE is directly constructed from the Navier–Stokes equations assuming $(\boldsymbol{u},p) \in [H^2(\Omega)]^d \times H^1(\Omega)$ [110, 111]. These requirements can be weakened through appropriate variational problems, as shown in Chapter 5.

As the PPE has higher-order derivatives when compared to the original mass-momentum system, the main underlying challenge is to construct appropriate variational formulations allowing standard finite element spaces – as already addressed in Chapter 5. Starting with the Newtonian case ($\nabla\mu \equiv \boldsymbol{0}$), we look for $(\boldsymbol{u}_h,p_h) \in [X_h]^d \times X_h$, with $\boldsymbol{u}_h|_{\Gamma_D} = \boldsymbol{g}_h$, such that

$$\begin{aligned} &\langle\boldsymbol{w}_h,(\rho\nabla\boldsymbol{u}_h)\boldsymbol{u}_h\rangle_\Omega + \langle\nabla\boldsymbol{w}_h,\mu\nabla\boldsymbol{u}_h\rangle_{L^2(\Omega)} - \langle\nabla\cdot\boldsymbol{w}_h,p_h\rangle_{L^2(\Omega)} = \langle\boldsymbol{w}_h,\tilde{\boldsymbol{t}}\rangle_{\Gamma_N}\,, \\ &\langle\beta_h q_h,\nabla\cdot\boldsymbol{u}_h\rangle_{L^2(\Omega)} + \langle\nabla q_h,\nabla p_h + (\rho\nabla\boldsymbol{u}_h)\boldsymbol{u}_h\rangle_{L^2(\Omega)} + \langle\nabla q_h\times\boldsymbol{n},\mu\nabla\times\boldsymbol{u}_h\rangle_\Gamma = 0\,, \end{aligned} \tag{6.11}$$

for all $(\boldsymbol{w}_h,q_h) \in [X_h]^d \times X_h$, with $\boldsymbol{w}_h|_{\Gamma_D} = \boldsymbol{0}$, with X_h being a continuous finite element space. Despite being very similar to PSPG (6.2) in form and structure, this PPE-based stabilisation is fully consistent for any continuous equal-order spaces, since no part of the residual vanishes due to low-order discretisation. The key term for retaining full consistency is the boundary integral proportional to the vorticity $\boldsymbol{\omega} := \nabla\times\boldsymbol{u}$. As a matter of fact, in the Newtonian case this term alone accounts for the entire viscous contribution to the residual. Hence, we shall henceforth refer to this method as *boundary vorticity stabilisation* (BVS). Other than that, the key distinction of the BVS method is that the stabilisation term is computed globally rather than only in element interiors. This is permitted as long as continuous spaces are used. It is important to mention that taking the (still undefined) parameter β_h as zero recovers the formulation introduced by Johnston and Liu [72] in the

context of split-step schemes. Their method, which we denote as BVS_0, has two important shortcomings: it requires $\Gamma_N = \emptyset$ and yields suboptimal velocity convergence in L^2 when using equal-order pairs. We will soon investigate how to select the parameter β_h to yield optimally convergent velocities.

For quasi-Newtonian fluids, only one additional term is needed in each equation, resulting in the problem to find $(\boldsymbol{u}_h, p_h, \mu_h) \in [X_h]^d \times X_h \times X_h$, with $\boldsymbol{u}_h|_{\Gamma_D} = \boldsymbol{g}_h$, such that

$$\begin{aligned}
\left\langle \boldsymbol{w}_h, (\rho\nabla\boldsymbol{u}_h)\boldsymbol{u}_h - (\nabla\boldsymbol{u}_h)^\top\nabla\mu_h \right\rangle_\Omega + \langle \nabla\boldsymbol{w}_h, \mu_h\nabla\boldsymbol{u}_h\rangle_{L^2(\Omega)} - \langle \nabla\cdot\boldsymbol{w}_h, p_h\rangle_{L^2(\Omega)} &= \langle \boldsymbol{w}_h, \tilde{\boldsymbol{t}}\rangle_{\Gamma_N}, \\
\langle \beta_h q_h, \nabla\cdot\boldsymbol{u}_h\rangle_{L^2(\Omega)} + \left\langle \nabla q_h, \nabla p_h + (\rho\nabla\boldsymbol{u}_h)\boldsymbol{u}_h - 2(\nabla\boldsymbol{u}_h)^\top\nabla\mu_h \right\rangle_\Omega + \langle \nabla q_h \times \boldsymbol{n}, \mu_h\nabla\times\boldsymbol{u}_h\rangle_\Gamma &= 0, \\
\langle \upsilon_h, \mu_h - \eta(\dot\gamma(\nabla^s\boldsymbol{u}_h))\rangle_{L^2(\Omega)} &= 0,
\end{aligned} \tag{6.12}$$

for all $(\boldsymbol{w}_h, q_h, \upsilon_h) \in [X_h]^d \times X_h \times X_h$, with $\boldsymbol{w}_h|_{\Gamma_D} = \boldsymbol{0}$.

The stabilisation parameter

The factor β_h in the divergence bilinear form is still undefined, and a comparison between our formulation and PSPG can aid the selection of this parameter. The PSPG term has the form

$$\langle q_h, \nabla\cdot\boldsymbol{u}_h\rangle_{L^2(\Omega)} + \sum_{e=1}^{N_e} \langle \delta_h\nabla q_h, \nabla p_h + (\rho\nabla\boldsymbol{u}_h)\boldsymbol{u}_h - 2\nabla^s\boldsymbol{u}_h\nabla\mu_h - 2\mu_h\nabla\cdot(\nabla^s\boldsymbol{u}_h)\rangle_{\Omega_e} = 0,$$

which when compared to the BVS formula reveals that the parameters β_h and δ_h have inverse roles. Therefore, we select β_h as the inverse of the PSPG stabilisation term, that is,

$$\beta_h = \frac{1}{\delta_h}. \tag{6.13}$$

Moreover, it is known that $\delta_h = \mathcal{O}(h^2)$ is the optimal choice for diffusion-dominated flows, whereas $\delta_h = \mathcal{O}(h)$ is optimal for convective regimes [26]. A more general expression can be used to account for local effects [31]:

$${\delta_h}^{-1} = \sqrt{\left(\frac{\alpha_1\mu_h}{h^2}\right)^2 + \left(\frac{\alpha_2\rho|\boldsymbol{u}_h|}{h}\right)^2 + \left(\frac{\alpha_3\rho}{\Delta t}\right)^2},$$

where Δt is the size of the temporal discretisation in time-dependent problems and α_1, α_2 and α_3 are appropriate stabilisation factors. Since our present focus is on diffusion-dominated flows, we use simply

$$\beta_h|_{\Omega_e} = \frac{\mu_h}{\alpha {h_e}^2}, \tag{6.14}$$

in which case we get

$$\left\langle \nabla q_h, \nabla p_h + (\rho \nabla \boldsymbol{u}_h)\boldsymbol{u}_h - 2\,(\nabla \boldsymbol{u}_h)^\top \nabla \mu_h \right\rangle_{L^2(\Omega)} + \langle \nabla q_h \times \boldsymbol{n}, \mu_h \nabla \times \boldsymbol{u}_h \rangle_\Gamma + \alpha^{-1} \sum_{e=1}^{N_e} {h_e}^{-2} \langle q_h, \mu_h \nabla \cdot \boldsymbol{u}_h \rangle_{\Omega_e} = 0 \tag{6.15}$$

as our stabilised continuity equation. We will later verify through several numerical examples that this is indeed the optimal choice for β_h. The stabilised equation (6.15) has the matrix form

$$\mathbf{K}\underline{p} + \left[\tilde{\mathbf{C}}(\boldsymbol{u}_h) + \mathbf{H}(\mu_h) + \tilde{\mathbf{B}}(\delta_h)\right]\underline{\boldsymbol{u}} - \left[\tilde{\mathbf{S}}(\boldsymbol{u}_h)\right]\underline{\mu} = \underline{f}\,, \tag{6.16}$$

where $\mathbf{K}$ is a standard (Laplacian) stiffness matrix, $\tilde{\mathbf{S}}$ is the viscosity gradient matrix, namely,

$$\tilde{S}_{ij}(\boldsymbol{u}_h) = 2\left\langle \frac{\partial \psi_i}{\partial x_k}\frac{\partial \boldsymbol{u}_h}{\partial x_k}, \nabla \psi_j \right\rangle_{L^2(\Omega)}, \tag{6.17}$$

and the remaining matrices have a horizontal block structure, e.g. $\mathbf{H} = [\mathbf{H}^1 \ldots \mathbf{H}^d]$, with

$$\tilde{C}^k_{ij}(\boldsymbol{u}_h) = \left\langle \rho \frac{\partial \psi_i}{\partial x_k}\boldsymbol{u}_h, \nabla \psi_j \right\rangle_{L^2(\Omega)}, \tag{6.18}$$

$$\tilde{B}^k_{ij}(\delta_h) = \left\langle \psi_i, \delta_h \frac{\nabla \psi_j}{\partial x_k} \right\rangle_{L^2(\Omega)}, \tag{6.19}$$

$$H^k_{ij}(\mu_h) = \sum_{m=1}^{d} \left\langle (\delta_{mk} - 1)\left(n_m \frac{\partial \psi_i}{\partial x_k} - n_k \frac{\partial \psi_i}{\partial x_m} \right), \mu_h \frac{\partial \psi_j}{\partial x_m} \right\rangle_\Gamma, \tag{6.20}$$

where n_k denotes the k-th component of the normal $\boldsymbol{n}$ and δ is the Kronecker delta.

Despite the similarities between our approach and the standard PSPG method, there is a fundamental difference. The added stabilisation terms in PSPG relax incompressibility in a completely artificial way, and *must* therefore be small for accuracy and even for stability (see the analysis in Ref. [86]). On the other hand, the stabilised form in our method is constructed from a strong equation that can be seen as a weighted sum of the continuity equation and a pressure Poisson equation that would *also on its own* enforce incompressibility. For $\beta \to \infty$ we have only the divergence-free constraint – which is unstable at the discrete level –, whereas for $\beta = 0$ (i.e., $\alpha \to \infty$) we have the pure PPE, which is stable but suboptimally convergent [103].

6.3 An ultra-weak stabilisation method allowing discontinuous pressure

It is clear that the stabilisation method we just presented requires $p_h \in H^1(\Omega)$. Although this is the case for nearly all commonly used finite element spaces, it can be of interest to

allow pressure discontinuities. This could be either for numerical reasons, such as using optimal lowest-order pairs, or due to the actual need for resolving high gradients or discontinuities (as in two-phase flows with surface tension). It turns out that stabilisation methods allowing piecewise constant pressure are quite scarce, since most residual-based methods rely on gradient-based terms such as $\langle \nabla q_h, \nabla p_h \rangle_{\Omega_e}$ for stability. We therefore present now an ultra-weak PPE-based stabilisation allowing Q_1Q_0 elements. One possibility would be to consider an expression similar to the one used for the continuous pressure case, i.e,

$$\begin{aligned}\langle \beta_h q_h, \nabla \cdot \boldsymbol{u}_h \rangle_{L^2(\Omega)} - \langle \Delta q_h, p_h \rangle_{L^2(\Omega)} + \langle \nabla q_h, (\rho \nabla \boldsymbol{u}_h)\boldsymbol{u}_h \rangle_{L^2(\Omega)} + \\ \langle \nabla(\nabla q_h), 2\mu_h \nabla^s \boldsymbol{u}_h \rangle_{L^2(\Omega)} - \langle \boldsymbol{n} \otimes \nabla q_h, 2\mu_h \nabla^s \boldsymbol{u}_h \rangle_{\Gamma} = 0\,.\end{aligned}$$

Although possible in principle, this may lead to worse conservation of mass than standard methods, due to the wider support of the C^1 test functions q_h. To illustrate that, let us assume that β_h is constant and large enough that the PPE terms can be neglected, so that

$$\langle q_h, \nabla \cdot \boldsymbol{u}_h \rangle_{L^2(\Omega)} \approx 0\,.$$

In that case, discrete conservation of mass is (approximately) fulfilled in each patch corresponding to the support of q_h. Thus, it is desirable to have as compact a support as possible. If we can use piecewise constant test functions, then the conservation of mass will be approximately satisfied per element. To achieve that, we consider an alternative formulation. Additionally to the momentum equation, we include two equations to find $(p_h, \tilde{p}_h) \in X_h \times X_h$ such that

$$\begin{aligned}\langle q_h, \nabla \cdot \boldsymbol{u} \rangle_{L^2(\Omega)} + \sum_{e=1}^{N_e} \delta_e \langle q_h, p_h - \tilde{p}_h \rangle_{\Omega_e} = 0\,, \\ -\langle \Delta \tilde{q}_h, \tilde{p}_h \rangle_{L^2(\Omega)} + \langle \nabla \tilde{q}_h, (\rho \nabla \boldsymbol{u}_h)\boldsymbol{u}_h \rangle_{L^2(\Omega)} + \\ \langle \nabla(\nabla \tilde{q}_h), 2\mu_h \nabla^s \boldsymbol{u}_h \rangle_{L^2(\Omega)} - \langle \boldsymbol{n} \otimes \nabla \tilde{q}_h, 2\mu_h \nabla^s \boldsymbol{u}_h \rangle_{\Gamma} = 0\end{aligned} \tag{6.21}$$

for all $(q_h, \tilde{q}_h) \in X_h \times Y_h$, where δ_e is a piecewise constant stabilisation parameter, X_h is the usual space of piecewise constants and Y_h is a C^1-conforming space as presented in Chapter 5. The underlying idea is to penalise fluctuations of the original pressure p_h with respect to the stable pressure $\tilde{p}_h$ coming from the PPE (see Ref. [112] for an overview of pressure-fluctuation-based stabilisation methods). This formulation is clearly consistent, since $p = \tilde{p}$ for the exact solution of the strong problem. The relaxed continuity equation thus reduces to an element-level constraint:

$$\frac{1}{|\Omega_e|} \int_{\Omega_e} \nabla \cdot \boldsymbol{u}_h \, \mathrm{d}\Omega = -\delta_e \, (p_e - \tilde{p}_e)\,, \tag{6.22}$$

that is, the velocity field will approximately conserve mass elementwise, up to a consistent term. In the numerical examples we will investigate how to select the stabilisation parameter δ_e to attain optimal convergence.

At first glance, it seems that this approach incurs extra computational cost due to the additional unknown $\tilde{p}_h$. Yet, it is possible to eliminate this unknown without having to invert the corresponding stiffness matrix. Let us write Eqs. (6.21) in matrix form as

$$\mathbf{B}\underline{\boldsymbol{u}} + \mathbf{D}\left(\underline{p} - \underline{\tilde{p}}\right) = \underline{0}, \tag{6.23}$$

$$\mathbf{K}\underline{\tilde{p}} + \left[\mathbf{N}(\boldsymbol{u}_h, \mu_h)\right]\underline{\boldsymbol{u}} = \underline{f}, \tag{6.24}$$

where $\mathbf{N}$ incorporates the nonlinear terms and $\mathbf{D}$ is a diagonal matrix with entries $D_{ee} = \delta_e|\Omega_e|$. Pre-multiplying Eq. (6.23) by $\mathbf{K}\mathbf{D}^{-1}$ leads to

$$\mathbf{K}\mathbf{D}^{-1}\mathbf{B}\underline{\boldsymbol{u}} + \mathbf{K}\left(\underline{p} - \underline{\tilde{p}}\right) = \underline{0},$$

in which we can substitute Eq. (6.24) to get

$$\left[\mathbf{K}\mathbf{D}^{-1}\mathbf{B} + \mathbf{N}(\boldsymbol{u}_h, \mu_h)\right]\underline{\boldsymbol{u}} + \mathbf{K}\underline{p} = \underline{f}. \tag{6.25}$$

By doing so, we have eliminated the additional pressure unknown at the "cost" of inverting only a diagonal matrix. As we shall see in the numerical examples, this stabilised method leads to very good local mass conservation.

6.4 Numerical examples

In this section, several numerical examples are provided in order to test our stabilised formulations' accuracy, stability and robustness with respect to stabilisation parameters. Most examples consider equal-order elements with linear or d-linear basis functions, and focus is placed on diffusion-dominated flows.

6.4.1 Elements with continuous pressure

In all cases involving a continuous pressure approximation, the stabilisation parameter is set as $\delta_h = \alpha h^2/\mu_h = {\beta_h}^{-1}$, with α being a positive stablisation factor whose effects we aim to investigate.

Carreau fluid through straight channel

Our first numerical example is the Poiseuille flow of a Carreau fluid in the channel $\Omega = (0, L) \times (-H/2, H/2)$, with $L = 3H = 3$ mm. We use the same rheological parameters as in Section 4.3 (see Eq. (4.17)) and impose no slip at the walls, $\tilde{\boldsymbol{t}}|_{x_1=0} = (p_{\text{in}}, 0)^\top$ and $\tilde{\boldsymbol{t}}|_{x_1=L} = \mathbf{0}$, with $p_{\text{in}} = 9$ Pa. A convergence study is performed with linear triangular elements, starting from the mesh depicted in Figure 6.1 and then applying six levels of uniform refinement.

Figure 6.2 shows a comparison between the BVS and PSPG methods for a stabilisation factor $\alpha = 1$. It is seen that, while the velocity errors are quite similar, the BVS method performs clearly better in the approximation of pressure. At the finest level, the BVS error is already thirty times smaller than that attained by PSPG, and this difference shows an increasing trend if the refinement continues.

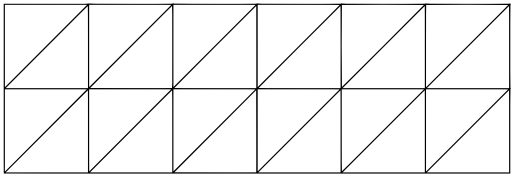

Figure 6.1: Carreau channel flow: coarsest mesh considered.

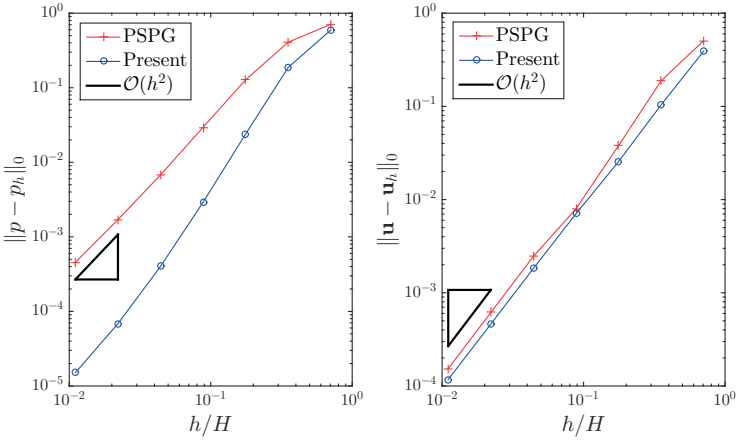

Figure 6.2: Carreau channel flow: uniform refinement study.

The similarity in the velocity errors does not hold in general, as revealed by the error *vs.* α plot in Figure 6.3. For small α, the methods perform similarly because the divergence-free constraint dominates over the stabilisation terms. However, increasing the stabilisation factor leads to a much faster increase in the velocity error for PSPG than for our method. For instance, from $\alpha = 0.1$ to $\alpha = 10$ the PSPG method experiences a 1000% increase in the velocity error, in contrast to only 12% in the BVS case. This is due to the improved

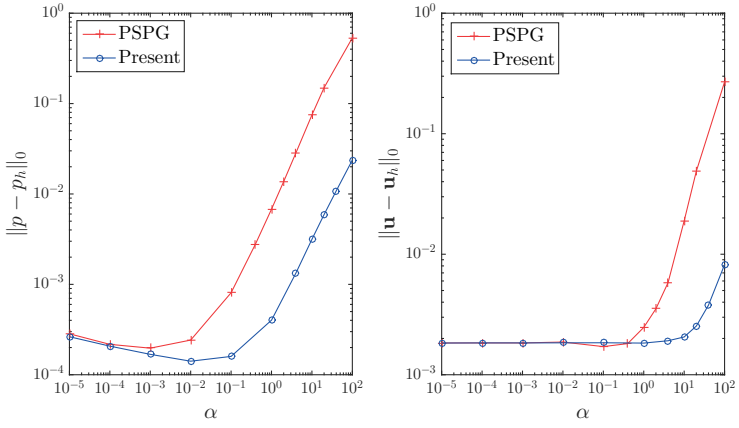

Figure 6.3: Carreau channel flow: effect of the stabilisation factor α.

mass conservation of our approach, which is fully consistent and does not "over-relax" incompressibility.

Additionally to the possible over-relaxation of incompressibility, standard low-order residual-based formulations have another well-known shortcoming: the induction of spurious pressure boundary layers – and the straight channel flow is a perfect example to illustrate that. For this problem, the momentum equation simplifies to

$$\nabla p = \mu \Delta \boldsymbol{u} + \nabla \boldsymbol{u} \nabla \mu \,.$$

Dividing both sides by μ and taking the divergence of the result gives us

$$\nabla \cdot \left(\mu^{-1} \nabla p \right) = \Delta \left(\nabla \cdot \boldsymbol{u} \right) + \frac{\partial}{\partial x_1} \left(\mu^{-1} \frac{\partial u_1}{\partial x_2} \frac{\partial \mu}{\partial x_2} \right) = 0 \,.$$

Thus, there holds

$$\nabla \cdot \boldsymbol{u} - \gamma \nabla \cdot \left(\mu^{-1} \nabla p \right) = 0 \tag{6.26}$$

for an arbitrary scalar γ. Let us now turn our attention to the stabilised formulation. In a uniform mesh with linear simplicial elements, we have $(\nabla \cdot \mathbb{S}_h)|_{\Omega_e} = \mathbf{0}$ and $h_e = h$ for all elements. Then, the PSPG term for this example reads simply

$$\int_\Omega q_h \nabla \cdot \boldsymbol{u}_h \, \mathrm{d}\Omega + \alpha h^2 \int_\Omega \mu_h^{-1} \nabla p_h \cdot \nabla q_h \, \mathrm{d}\Omega = 0 \,, \tag{6.27}$$

which is the weak form of

$$\nabla \cdot \boldsymbol{u} - \alpha h^2 \nabla \cdot \left(\mu^{-1} \nabla p \right) = 0 \ \text{ in } \Omega, \tag{6.28}$$

$$\frac{\partial p}{\partial n} = 0 \ \text{ on } \Gamma. \tag{6.29}$$

That is, although Eq. (6.28) is consistent with this particular example (due to Eq. (6.26)), the PSPG term induces zero Neumann BCs for the pressure as a numerical artifact. This results in loss of accuracy close to the boundary, especially if the stabilisation factor α is not small [82]. Therefore, α must be large enough to attain stability, but not so large that spurious pressure boundary layers become relevant – and this, of course, restricts the choice of the stabilisation parameter. In Figure 6.4 we display the pressure along the channel's centreline, for different values of α. The induced Neumann BCs can be clearly seen in the PSPG solution, and the affected region becomes larger as α increases. Conversely, when using the BVS this is not an issue, since the pressure satisfies consistent boundary conditions derived from the momentum equation.

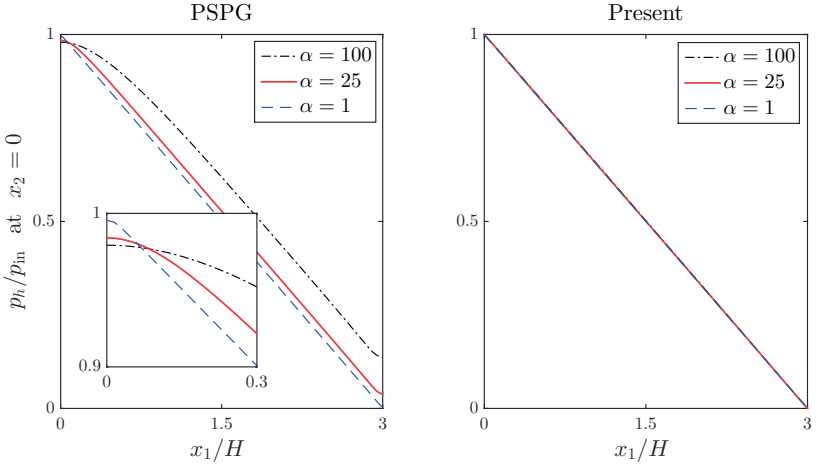

Figure 6.4: Carreau channel flow: centreline pressure for different stabilisation factors, demonstrating the zero Neumann conditions artificially induced by lowest-order PSPG.

Stokes flow in the unit circle

We consider now the benchmark case proposed by Weidman [113]. It consists of the Stokes problem in a circular domain with unit radius, centred at the origin, with zero body

force and periodic Dirichlet datum $u_\theta|_\Gamma = \cos n\theta$, in which n is an integer greater than one, u_θ denotes the circumferential velocity and $\theta = \tan^{-1}(x_2/x_1)$. For $\mu \equiv 1$ and $n = 2$, the analytical solution is

$$\boldsymbol{u} = \begin{pmatrix} 2{x_2}^3 - x_2 \\ 2{x_1}^3 - x_1 \end{pmatrix}, \quad p = 12 x_1 x_2. \tag{6.30}$$

For this example, we consider the mesh depicted in Figure 6.5 (due to symmetry, only a quarter of the mesh is shown). The first goal is to compare the BVS and PSPG methods regarding their performance with respect to the stabilisation factor α. The L^2 errors for $\alpha \in [10^{-4}, 10^5]$ are shown in Figure 6.6, and important considerations can be drawn. The expected behaviour is once again observed: the pressure error is large for small values of α, decreases as α is increased, reaches a minimum, then starts growing again and eventually settles at a finite value. The two formulations yield similar results for small α, since the divergence-free constraint dominates over the stabilisation terms. However, the reasons why each method reaches a limiting performance for $\alpha \to \infty$ are distinct. In the PSPG formulation, the error becomes very high because a large α leads to over-relaxation of incompressibility; in our formulation, $\alpha \to \infty$ leads to the pressure Poisson equation completely replacing the divergence-free constraint, which does not violate (approximate) incompressibility but results in suboptimal convergence [103]. Therefore, the error for large α is much higher for PSPG than for the present formulation. Moreover, the former's incomplete residual has an important impact on the parameter selection. The numerical solution is very sensitive to the stabilisation parameter, with the error growing very fast when α moves away from its optimal value in either direction. Conversely, in our method the error varies in a smoother way and allows more freedom in the parameter selection. This is a crucial feature for a stabilisation technique, since the optimal parameters are problem- and discretisation-dependent. It is also seen that, for this example, the minimum error yielded by our formulation is around one order of magnitude lower than that from PSPG.

To quantitatively investigate the issue of spurious pressure boundary layers induced by the incomplete residual, we assess the pressure error on the boundary, as proposed by Burman and Hansbo [82], using the norm

$$\|p - p_h\|_\Gamma := \frac{\|p - p_h\|_{L^2(\Gamma)}}{\|p\|_{L^2(\Gamma)}}.$$

Note that for this example, as in the previous one, the PSPG method with linear elements reduces to the original formulation of Brezzi and Pitkäranta [23], which contains only the term $\langle \delta_h \nabla q_h, \nabla p_h \rangle_{L^2(\Omega)}$ and therefore induces zero Neumann BCs for the pressure. We also include in the comparison the results attained through the pressure gradient projection (PGP) method of Codina and Blasco [90], which is fully consistent for any continuous equal-order pairs (see (6.3)). The plot shown in Figure 6.7 reveals a similar trend to that attained by edge stabilisation methods [82]: the consistent residual increases the order of the approximation on the boundary, at least initially. This is due to the fact that our formulation is derived from a boundary value problem with consistent pressure BCs [44]. In

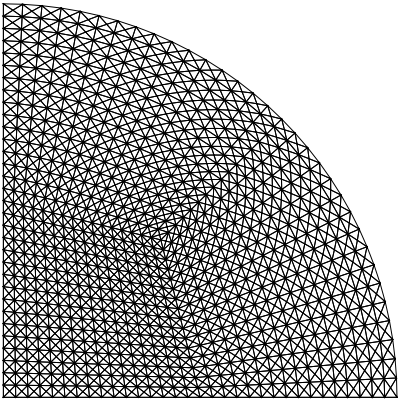

Figure 6.5: Stokes flow in the unit circle: a quarter of the mesh employed.

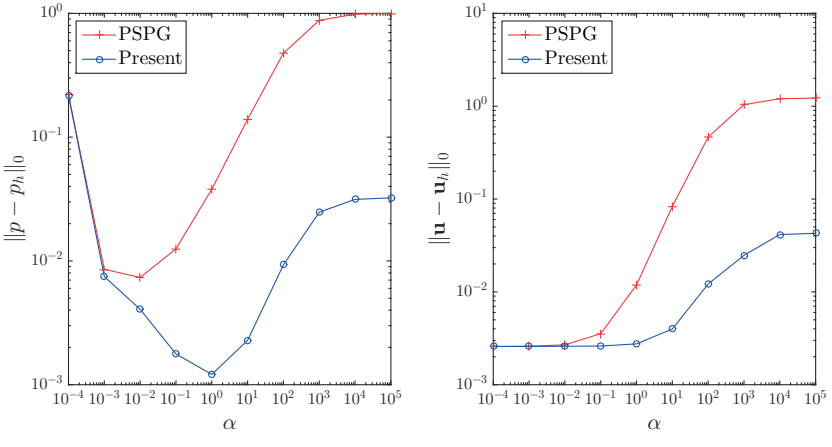

Figure 6.6: Stokes flow in the unit circle: errors for different stabilisation factors.

comparison to edge stabilisation methods, ours has the advantage of not requiring operations involving internal edges/faces, which simplifies implementation. We also see that our method performs very similarly to the PGP technique and even sustains the quadratic

rate longer – with the advantage of not requiring expensive vector projections.

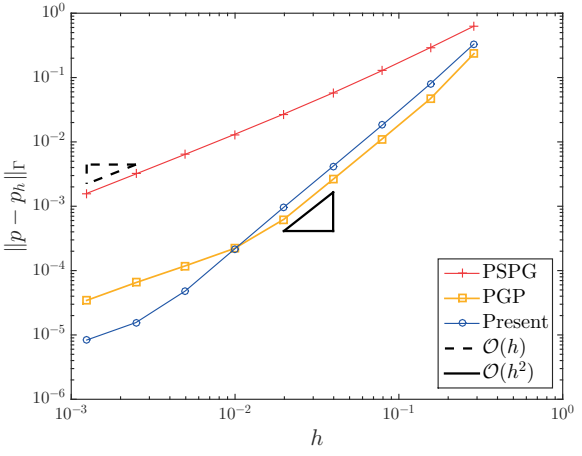

Figure 6.7: Stokes problem in the unit circle: pressure convergence in $L^2(\Gamma)$ for different stabilisation methods, using $\alpha = 0.1$.

Kovasznay flow benchmark

Another classic benchmark for the Newtonian Navier–Stokes problem is the Kovasznay flow [114]. It is one of the only known problems with zero body force and an analytical solution, and models the behaviour of laminar flow past cylinders. The non-dimensionalised solution in $\Omega = (-1/2, 1/2)^2$ is

$$\boldsymbol{u} = \begin{pmatrix} 1 - e^{kx_1}\cos 2\pi x_2 \\ \frac{k}{2\pi} e^{kx_1} \sin 2\pi x_2 \end{pmatrix}, \quad p = \frac{e^k - e^{2kx_1}}{2},$$

with $2k = \mathrm{Re} - \sqrt{\mathrm{Re}^2 + (4\pi)^2}$. We solve the corresponding Dirichlet problem using linear triangular elements. The coarsest mesh is shown in Figure 6.8, and then seven levels of uniform refinement are considered. The pressure and velocity errors for $\mathrm{Re} = 100$ and $\alpha = 1$ are shown in Figure 6.9. We observe that, although both PSPG and BVS methods converge with similar rates, the former takes longer to reach the asymptotic behaviour, which leads to larger errors. The reason for this "delayed" convergence is the fact that the artificial pressure BCs induced by the PSPG formulation only become negligible as the mesh size goes to zero [57]. Another important finding from the convergence plots is

the remarkable performance gain of our approach with respect to the BVS_0 formulation of Johnston and Liu [72], through the addition of the simple term $\langle q_h, \beta_h \nabla \cdot \boldsymbol{u}_h \rangle_{L^2(\Omega)}$ to penalise large velocity divergences.

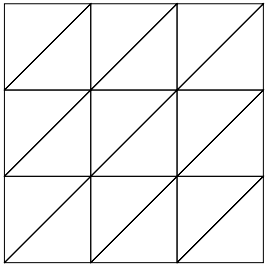

Figure 6.8: Kovasznay benchmark: coarsest mesh used in the refinement study.

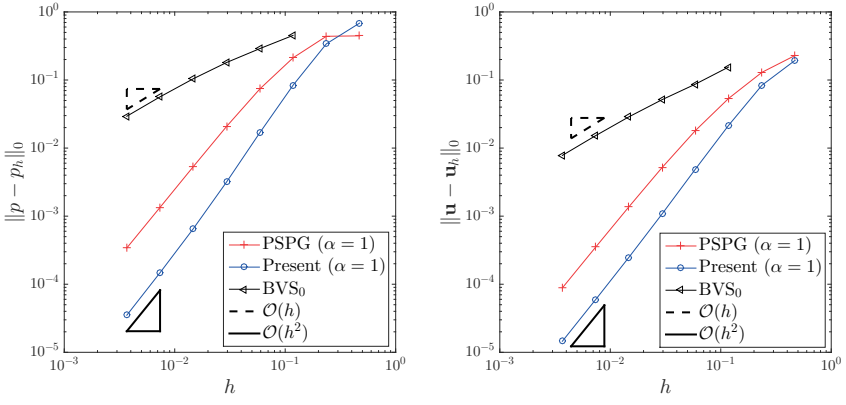

Figure 6.9: Kovasznay benchmark: uniform refinement study.

To further illustrate how the incomplete residual can impact the quality of the approximation, we show in Figure 6.10 the pressure isolines for the Kovasznay problem with $\mathrm{Re} = 40$, $\alpha = 100$ and the third finest mesh considered in the convergence study. This is a particularly good example for illustrating the issue of spurious pressure boundary layers, since the exact solution has perfectly vertical isolines. Note that the stabilisation parameter is deliberately chosen far from the optimal values, so as to critically test the performance of

both methods. We see that PSPG yields completely distorted lines all over the domain, whereas in our approach there is only a mild distortion close to the corners.

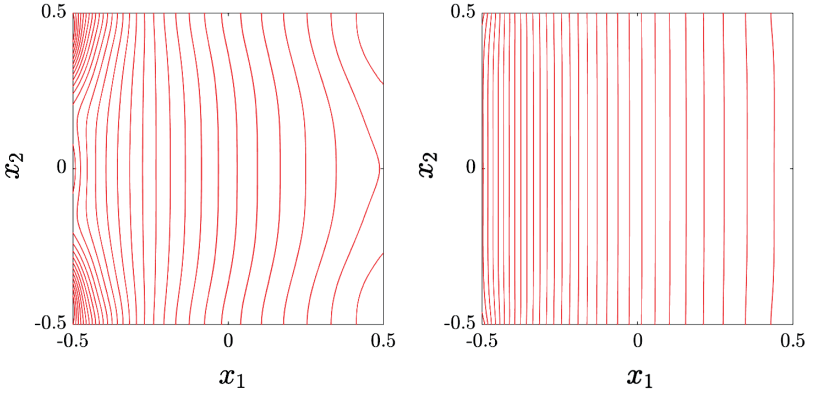

Figure 6.10: Kovasznay benchmark: pressure isolines for PSPG (left) and BVS (right).

It is also of interest to investigate how our method performs in combination with equal-order spaces of higher polynomial degree, since they are able to approximate the viscous terms in the standard PSPG residual. We investigate this by assessing the effect of the stabilisation factor α for elements of type $Q_k Q_k$, with $k = 1,2,3,4$. We consider a 64×64 uniform grid and Re = 100. The results depicted in Figure 6.11 reveal once again an increase in accuracy for a wider range of α. This is due to the fact that, even though the PSPG residual is complete for $k > 1$, large α leads to an over-relaxation of the incompressibility constraint. This does not happen in our PPE-based formulation, which conserves mass even for $\alpha \to \infty$ ($\beta = 0$, see Eq. (6.9)). Especially for $k = 4$, the approximation attained by our method has proven considerably less sensitive to variations of the stabilisation parameter. For $\alpha > 10$ the solution of the PSPG method (considering zero initial guess for the iterative scheme) diverged.

In order to put our method to a more challenging test, we use now anisotropic, highly non-uniform meshes. The coarsest mesh is shown in Figure 6.12, where we can see that the element size varies by a factor of up to 9 between adjacent elements – a rather extreme setting. The pressure and velocity errors for $\alpha = 10$ are shown in Figure 6.13, where good stability and convergence behaviour is verified, as in previous examples.

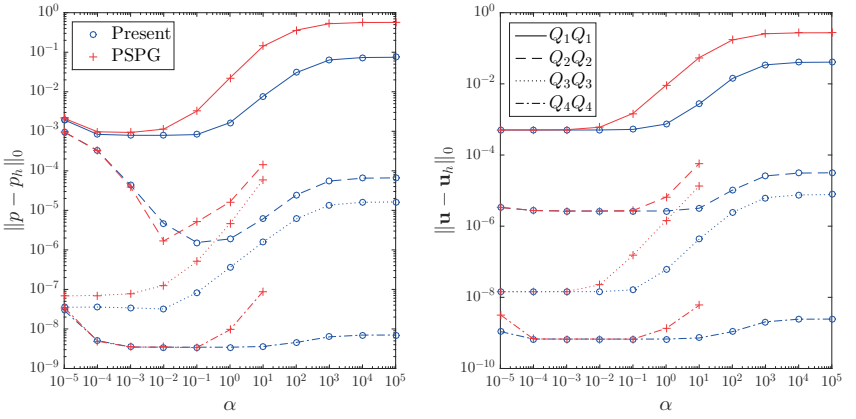

Figure 6.11: Kovasznay benchmark: error *vs.* stabilisation factor for elements of up to order 4.

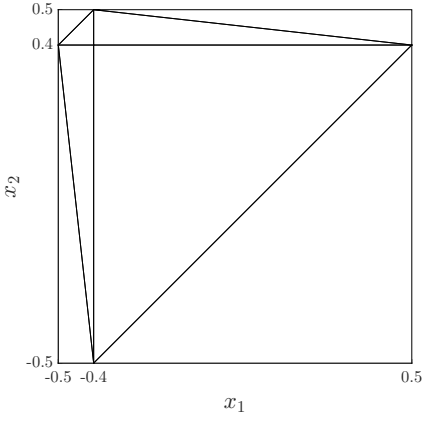

Figure 6.12: Kovasznay benchmark: coarsest anisotropic mesh considered.

Carreau–Yasuda fluid past a backward-facing step

A benchmark problem with less smooth solution is the backward-facing step already considered in previous chapters. For this example we employ the Carreau–Yasuda fluid model

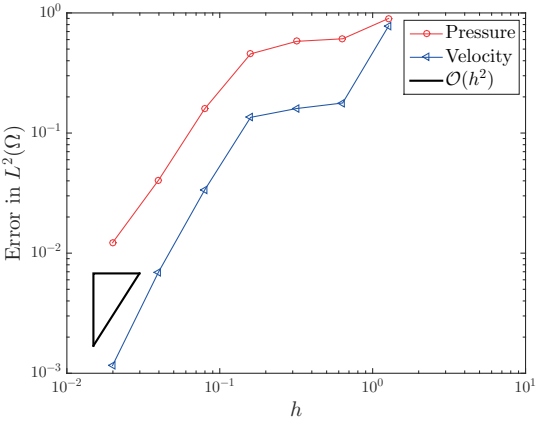

Figure 6.13: Kovasznay benchmark: refinement study with anisotropic meshes.

(*cf.* Eq. (4.15)) with the same parameters used in the second example of Section 5.4. The geometric proportions are as in Figure 4.6, and three different inlet channel heights are considered: $H = 0.5$, 5 and 50 mm. We set Re = 25 to compare our results to those by Masud and Kwack [36], who employed a variational multi-scale method (VMS) for the stabilisation. The comparison is done with respect to the normalised wall shear stress $\overline{\tau_w}$ along the line $x_2 = 0$:

$$\overline{\tau_w} := \frac{\left[\eta(\dot{\gamma})\frac{\partial u_1}{\partial x_2}\right]\Big|_{x_2=0}}{6\mu_\infty Q/(2H)^2},$$

whose denominator corresponds to the wall shear stress of a developed Newtonian flow. For the numerical solution, we use $\alpha = 0.1$ and a uniform mesh with 50,000 bilinear square elements in all three cases. The comparison depicted in Figure 6.14 reveals good agreement between the solutions, especially for $H = 0.5$ and 5 mm. For $H = 50$ mm there is a discrepancy of around 2%. Fortunately, it is possible to compute the exact wall shear stress of the developed flow:

$$\tau_w^\infty = -\frac{2H}{2}\frac{\partial p}{\partial x_1}\bigg|_{x_1\to\infty}, \tag{6.31}$$

due to equilibrium of forces. Although the pressure gradient is not known right away, it can be computed iteratively from the known flow rate Q. Then, with this semi-analytical value of τ_w^∞, we are able to verify that our solution differs in less than 0.5% from the exact one, while the VMS approximation differs in around 3%. For completeness, we present in Table 6.1 the comparison for the other geometries, along with the maximum and minimum values of $\overline{\tau_w}$.

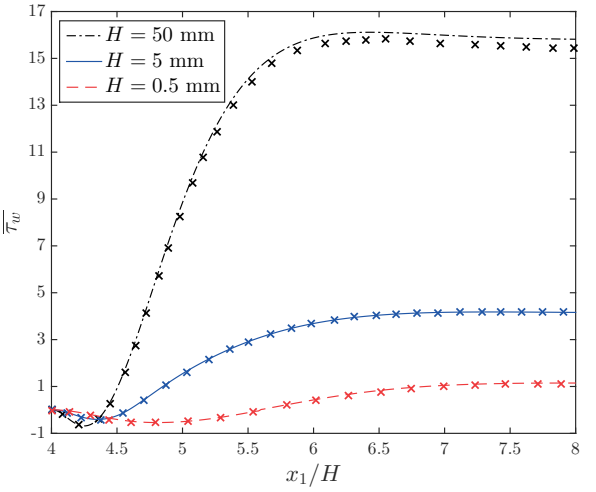

Figure 6.14: Backward-facing step with Carreau–Yasuda fluid: wall shear stress along $x_2 = 0$ (downstream of the step) for the BVS (lines) and VMS (markers) [36] methods.

Table 6.1: Backward-facing step with Carreau–Yasuda fluid: maximum and minimum wall shear stresses along $x_2 = 0$.

H [mm]	$\min\{\overline{\tau_w}\}$	$\max\{\overline{\tau_w}\}$	$\overline{\tau_w}\|_{x_1=L}$	$\overline{\tau_w^\infty}$ (analytical)
0.5	-0.5394	1.147	1.087	1.099
5	-0.4048	4.180	4.139	4.167
50	-0.6814	16.115	15.839	15.897

6.4.2 Elements with discontinuous pressure

We now assess the performance of the ultra-weak stabilised formulation presented in Section 6.3 for Q_1Q_0 elements. The main goal is to, via numerical examples, find a suitable expression for the stabilisation parameter δ_e.

Manufactured Stokes solution in L-shaped domain

The first example consists of a Stokes flow in the L-shaped domain $\Omega = (0,1)^2 \setminus [0,1/2]^2$. For the discretisation we employ a hybrid approach: the momentum and (relaxed) continu-

ity equations are posed in Ω, whereas the PPE is split into two weakly coupled subproblems in two rectangular subdomains of Ω, as shown in Figure 5.3. Setting $\mu \equiv 1$, $\boldsymbol{u}|_\Gamma = \mathbf{0}$ and body force

$$\boldsymbol{f} = \begin{pmatrix} 80x_2 + 8\pi^2 \sin(4\pi x_2)(1 - 2\cos(4\pi x_1)) \\ 80x_1 + 8\pi^2 \sin(4\pi x_1)(2\cos(4\pi x_2) - 1) \end{pmatrix}$$

leads to the solution

$$\boldsymbol{u} = \begin{pmatrix} \sin(4\pi x_2)\sin^2(2\pi x_1) \\ -\sin(4\pi x_1)\sin^2(2\pi x_2) \end{pmatrix}, \quad p = 80x_1x_2 - 25.$$

For the convergence study, we consider two expressions for the stabilisation parameter: $\delta_e = \alpha$ and $\delta_e = \alpha h_e$, with $\alpha > 0$. Six levels of uniform refinement are performed, starting from the mesh shown in Figure 5.3. The error plots in Figure 6.15 show that both types of stabilisation parameters result in stable solutions with linear pressure convergence, but $\delta_e = \mathcal{O}(1)$ yields only linear velocity convergence, while $\delta_e = \mathcal{O}(h_e)$ delivers the full quadratic order. In fact, the PSPG formulation for zeroth-order pressure elements (often called *jump stabilisation*) also has a stabilisation parameter proportional to the element size [6]. We remark that this particular problem has a smooth (manufactured) solution, despite the re-entrant corner at $x_1 = x_2 = 1/2$.

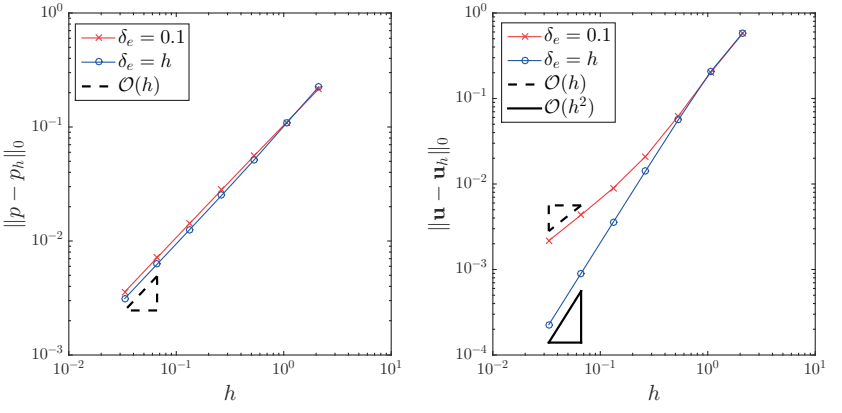

Figure 6.15: Manufactured Stokes solution in L-shaped domain: convergence of the stabilised Q_1Q_0 elements for two different types of stabilisation parameter.

For $\delta_e = h_e$, Figure 6.16 shows the maximum element-mean $\nabla \cdot \boldsymbol{u}_h$, which is a measure of local mass conservation. Although the divergence is expected to converge to zero linearly

in $L^2(\Omega)$, the local error here is quadratic, since

$$\frac{1}{|\Omega_e|}\left|\int_{\Omega_e} \nabla\cdot\boldsymbol{u}_h \,\mathrm{d}\Omega\right| = \delta_e|p_e-\tilde{p}_e| = \mathcal{O}(h_e)\mathcal{O}(h_e) = \mathcal{O}({h_e}^2).$$

This is an important advantage of having discontinuous test functions in the continuity equation.

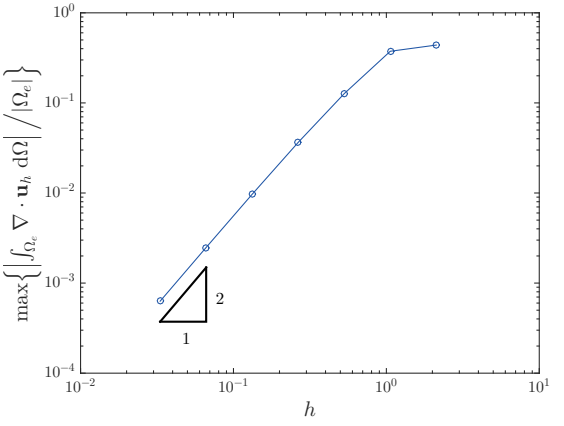

Figure 6.16: Manufactured Stokes solution in L-shaped domain: local divergence error.

Two-phase Poiseuille flow

A problem with less smooth yet still simple solution is the parallel flow of two immiscible fluids with different viscosities. Let us consider a channel $\Omega = (0,L)\times(-H,H)$, with the lower half $(0,L)\times(-H,0)$ occupied by a fluid having a constant viscosity μ_1, and the upper half containing a different fluid with viscosity μ_2. If the pressure is constant along the x_2 direction and has a constant gradient k in the x_1 direction, then solving the momentum equation enforcing (a) no slip on the walls and (b) continuity of velocity and stresses on the interface $x_2 = 0$ gives the analytical velocity profile

$$u_1 = -kH^2\frac{\left[1-(x_2/H)^2\right]+\left[\mathrm{sgn}(x_2)-(x_2/H)\right]\lambda}{\mu_2+\mu_1+(\mu_2-\mu_1)\mathrm{sgn}(x_2)}, \quad \text{with} \quad \lambda := \frac{\mu_2-\mu_1}{\mu_2+\mu_1}.$$

Notice that the velocity profile is continuous but has a kink at the interface, as shown in Figure 6.17. Here it is important to use the stress-divergence formulation to avoid the term $\nabla\mu$, since the viscosity is not continuous. We consider a test case with $k = -1$, $L = 2H = 1$ and $\mu_2 = 3\mu_1 = 3$. The convergence study considers two different families of meshes: one resolving the interface $x_2 = 0$, and another one with the interface going through a row of elements. The former starts with a mesh containing 4×4 square elements, while the latter is generated similarly, but with central nodes slightly shifted upwards. The error plot for $\delta_e = h_e$ in Figure 6.18 confirms the optimal rates for the meshes resolving the interface, whereas the convergence of the second family of meshes seems to eventually degrade to linear. This suboptimal convergence is a known result in two-phase flow problems and can be overcome by enriching the discrete velocity space with distance functions to resolve the kinks [115].

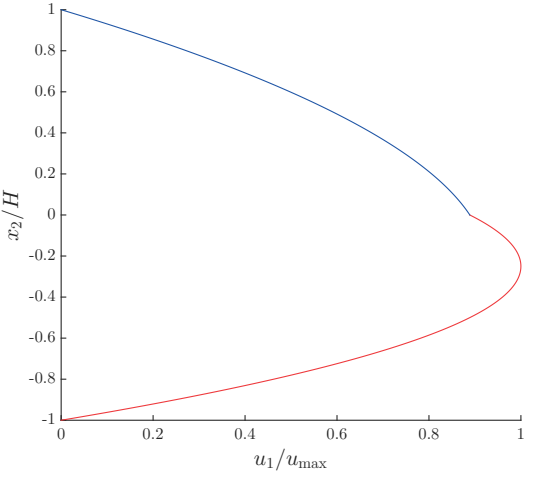

Figure 6.17: Two-phase Poiseuille profile for $\mu_2/\mu_1 = 3$.

6.5 On the pressure convergence of equal-order methods

A reader who is closely familiar with equal-order methods for incompressible flow problems may have noticed that the pressure convergence observed in Subsection 6.4.1 is somewhat higher than expected. In fact, under standard assumptions, the classical theory for

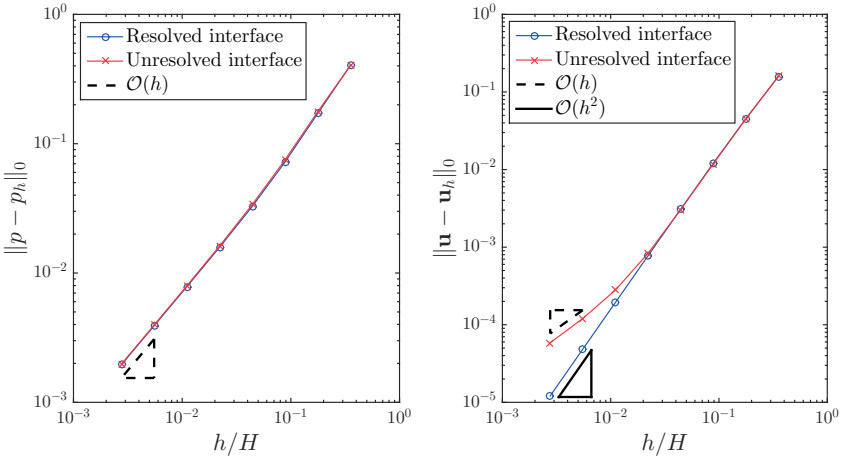

Figure 6.18: Two-phase Poiseuille flow: convergence for meshes with resolved and unresolved interface.

Q_kQ_k and P_kP_k elements only guarantees a $\mathcal{O}(h^k)$ convergence in $L^2(\Omega)$ for the pressure approximation, although higher orders are often observed in numerical experiments [5, 25, 116, 117]. Indeed, a $\mathcal{O}(h^{k+½})$ convergence can be shown to hold for very smooth problems in certain special meshes, at least for low-order elements [116]. We will next show that, under certain conditions, an *initial* higher-order convergence for the pressure may in fact be expected when using equal-order elements. As a model problem we consider the Dirichlet boundary value problem for the Stokes system

$$\begin{aligned} -\Delta \boldsymbol{u} + \nabla p &= \boldsymbol{f} \ \text{ in } \ \Omega, \\ \nabla \cdot \boldsymbol{u} &= 0 \ \text{ in } \ \Omega, \\ \boldsymbol{u} &= \boldsymbol{0} \ \text{ on } \ \Gamma. \end{aligned} \tag{6.32}$$

To simplify the notation, we will make no distinction between scalar- and vector-valued spaces. Using the Riesz representation, we can define bounded linear operators $A : H_0^1(\Omega) \to H^{-1}(\Omega)$ and $B : L^2(\Omega) \to H^{-1}(\Omega)$, i.e.,

$$\langle A\boldsymbol{u}, \boldsymbol{v} \rangle := \int_\Omega \nabla \boldsymbol{u} : \nabla \boldsymbol{v} \, \mathrm{d}\Omega \ \text{ and } \ \langle Bp, \boldsymbol{v} \rangle := \int_\Omega p \nabla \cdot \boldsymbol{v} \, \mathrm{d}\Omega$$

for all $\boldsymbol{u}, \boldsymbol{v} \in H_0^1(\Omega)$ and $p \in L^2(\Omega)$. Note that

$$\langle A\boldsymbol{v}, \boldsymbol{v} \rangle = \|\boldsymbol{v}\|^2_{H_0^1(\Omega)} \ \text{ and } \ \langle A\boldsymbol{u}, \boldsymbol{v} \rangle \leq \|\nabla \boldsymbol{u}\|_{L^2(\Omega)} \|\nabla \boldsymbol{v}\|_{L^2(\Omega)}$$

for all $\boldsymbol{u},\boldsymbol{v} \in H^1_0(\Omega)$, as well as

$$\langle B p, \boldsymbol{v}\rangle \leq \|p\|_{L^2(\Omega)} \|\nabla \boldsymbol{v}\|_{L^2(\Omega)} \quad \text{for all} \quad p \in L^2(\Omega),\, \boldsymbol{v} \in H^1_0(\Omega).$$

We can then write the variational formulation for (6.32) in operator form as

$$\begin{bmatrix} A & -B \\ C & D \end{bmatrix} \begin{pmatrix} \boldsymbol{u} \\ p \end{pmatrix} = \begin{pmatrix} \boldsymbol{f} \\ g \end{pmatrix}, \tag{6.33}$$

in which D, C and g account for possible stabilising terms. As usual, we assume that D is a non-negative operator and C is bounded:

$$\|C\boldsymbol{v}\|_{L^2(\Omega)} \leq c_2^C \|\boldsymbol{v}\|_{H^1_0(\Omega)} \quad \text{for all} \quad \boldsymbol{v} \in H^1_0(\Omega).$$

When considering compatible spaces or a purely pressure-based stabilisation method, we have simply $C = B'$.

Since A is invertible, we can solve the first equation in (6.33) to get the Schur complement system

$$\underbrace{[CA^{-1}B + D]}_{=:\, S} p = \underbrace{g - CA^{-1}\boldsymbol{f}}_{=:\, f}. \tag{6.34}$$

In other words, we have the variational formulation to find $p \in L^2(\Omega)$ such that

$$\langle Sp, q\rangle_{L^2(\Omega)} = \langle f, q\rangle_{L^2(\Omega)} \quad \text{for all} \quad q \in L^2(\Omega). \tag{6.35}$$

From the properties of A, B, C and D, at the continuous level we immediately get that the operator $S : L^2(\Omega) \to L^2(\Omega)$ is bounded and elliptic, that is,

$$\langle Sq, q\rangle_{L^2(\Omega)} \geq c_1^S \|q\|^2_{L^2(\Omega)} \quad \text{and} \quad \|Sq\|_{L^2(\Omega)} \leq c_2^S \|q\|_{L^2(\Omega)} \quad \text{for all} \quad q \in L^2(\Omega).$$

Therefore, we conclude unique solvability of the variational problem (6.35). For a conforming finite element space $\Pi_h = S^\nu_h(\Omega) \subset L^2(\Omega)$ of piecewise polynomial basis functions of degree ν, we consider the Galerkin formulation to find $p_h \in \Pi_h$ such that

$$\langle Sp_h, q_h\rangle_\Omega = \langle f, q_h\rangle_\Omega \quad \text{for all} \quad q_h \in \Pi_h\,.$$

Using standard arguments we arrive at Cea's lemma

$$\|p - p_h\|_{L^2(\Omega)} \leq \frac{c_2^S}{c_1^S} \inf_{q_h \in \Pi_h} \|p - q_h\|_{L^2(\Omega)}\,,$$

and from the approximation property of Π_h we finally conclude the error estimate

$$\|p - p_h\|_{L^2(\Omega)} \leq c_1\, h^{\nu+1}\, |p|_{H^{\nu+1}(\Omega)} \tag{6.36}$$

when assuming $p \in H^{\nu+1}(\Omega)$.

Since the composed operator $S = CA^{-1}B + D$ in general does not allow a direct evaluation, we construct a suitable approximation by defining, for any $p \in L^2(\Omega)$, a vector $\tilde{\boldsymbol{u}} = A^{-1}Bp \in H_0^1(\Omega)$, which is the unique solution of the variational formulation

$$\langle A\tilde{\boldsymbol{u}}, \boldsymbol{v}\rangle = \langle p, B\boldsymbol{v}\rangle \quad \text{for all} \quad \boldsymbol{v} \in H_0^1(\Omega).$$

Let $X_h := S_h^\mu(\Omega) \cap H_0^1(\Omega)$ be a second finite element space of polynomial basis functions with degree μ, for which we consider the Galerkin formulation to find $\tilde{\boldsymbol{u}}_h \in X_h$ such that

$$\langle A\tilde{\boldsymbol{u}}_h, \boldsymbol{v}_h\rangle = \langle p, B\boldsymbol{v}_h\rangle \quad \text{for all} \quad \boldsymbol{v}_h \in X_h.$$

From the ellipticity of A and the boundedness of B we have

$$\|\tilde{\boldsymbol{u}}_h\|^2_{H_0^1(\Omega)} = \langle A\tilde{\boldsymbol{u}}_h, \tilde{\boldsymbol{u}}_h\rangle = \langle p, B\tilde{\boldsymbol{u}}_h\rangle \le \|p\|_{L^2(\Omega)} \|\tilde{\boldsymbol{u}}_h\|_{H_0^1(\Omega)},$$

that is,

$$\|\tilde{\boldsymbol{u}}_h\|_{H_0^1(\Omega)} \le \|p\|_{L^2(\Omega)}.$$

Moreover, using standard arguments, we obtain the *a priori* error estimate

$$\|\tilde{\boldsymbol{u}} - \tilde{\boldsymbol{u}}_h\|_{H_0^1(\Omega)} \le \inf_{\boldsymbol{v}_h \in X_h} \|\tilde{\boldsymbol{u}} - \boldsymbol{v}_h\|_{H_0^1(\Omega)} \le c_2\, h^\mu\, |\tilde{\boldsymbol{u}}|_{H^\mu(\Omega)}$$

when assuming $\tilde{\boldsymbol{u}} \in H^\mu(\Omega)$. Instead of

$$Sp = CA^{-1}Bp + Dp = C\tilde{\boldsymbol{u}} + Dp,$$

we now define the approximate operator

$$\tilde{S}p := C\tilde{\boldsymbol{u}}_h + Dp, \tag{6.37}$$

where we have

$$\|Sp - \tilde{S}p\|_{L^2(\Omega)} = \|C(\tilde{\boldsymbol{u}} - \tilde{\boldsymbol{u}}_h)\|_{L^2(\Omega)} \le c_2^C\, \|\tilde{\boldsymbol{u}} - \tilde{\boldsymbol{u}}_h\|_{H_0^1(\Omega)} \le c_3\, h^\mu\, |\tilde{\boldsymbol{u}}|_{H^{\mu+1}(\Omega)}.$$

Moreover, $\tilde{S} : L^2(\Omega) \to L^2(\Omega)$ is bounded:

$$\|\tilde{S}p\|_{L^2(\Omega)} = \|C\tilde{\boldsymbol{u}}_h + Dp\|_{L^2(\Omega)} \le c_2^C \|\tilde{\boldsymbol{u}}_h\|_{H_0^1(\Omega)} + c_2^D \|p\|_{L^2(\Omega)} \le \left(c_2^C + c_2^D\right) \|p\|_{L^2(\Omega)}.$$

Let us assume that $\tilde{S}$ is elliptic in Π_h, i.e.,

$$\langle \tilde{S}q_h, q_h\rangle_\Omega \ge c_{\tilde{S}} \|q_h\|^2_{L^2(\Omega)} \quad \text{for all} \quad q_h \in \Pi_h.$$

Note that this assumption is satisfied when using either inf-sup stable finite elements or appropriate stabilisation operators. We now consider the perturbed variational formulation to find $\tilde{p}_h \in \Pi_h$ such that

$$\langle \tilde{S}\tilde{p}_h, q_h\rangle_\Omega = \langle f, q_h\rangle_\Omega \quad \text{for all} \quad q_h \in \Pi_h. \tag{6.38}$$

Now we recall the well-known Strang lemma.

Theorem 6.2. *Let $\tilde{S}$ be the approximate Schur complement operator as defined in* (6.37)*, and $\tilde{p}_h$ the corresponding pressure approximation from* (6.38)*. Then, under the assumptions of* (6.36) *and, additionally, the ellipticity of $\tilde{S}$, there holds the error estimate*

$$\|p - \tilde{p}_h\|_{L^2(\Omega)} \leq \alpha\, h^{\nu+1}\, |p|_{H^{\nu+1}(\Omega)} + \beta\, h^{\mu}\, |\tilde{\boldsymbol{u}}|_{H^{\mu+1}(\Omega)}\,,$$

with α and β independent of h.

Proof. From the triangle inequality and the error estimate (6.36) we have

$$\|p - \tilde{p}_h\|_{L^2(\Omega)} \leq \quad \|p - p_h\|_{L^2(\Omega)} + \|p_h - \tilde{p}_h\|_{L^2(\Omega)} \leq \quad c_1\, h^{\nu+1}\, |p|_{H^{\nu+1}(\Omega)} + \|p_h - \tilde{p}_h\|_{L^2(\Omega)}\,.$$

From the ellipticity of $\tilde{S}$ in Π_h we now conclude

$$\begin{aligned} c_{\tilde{S}}\, \|p_h - \tilde{p}_h\|^2_{L^2(\Omega)} &\leq \langle \tilde{S}(p_h - \tilde{p}_h), p_h - \tilde{p}_h \rangle_\Omega \\ &= \langle (\tilde{S} - S) p_h, p_h - \tilde{p}_h \rangle_\Omega \\ &\leq \|(\tilde{S} - S) p_h\|_{L^2(\Omega)} \|p_h - \tilde{p}_h\|_{L^2(\Omega)}\,, \end{aligned}$$

that is,

$$\begin{aligned} c_{\tilde{S}} \|p_h - \tilde{p}_h\|_{L^2(\Omega)} &\leq \|(\tilde{S} - S) p_h\|_{L^2(\Omega)} \\ &\leq \|(\tilde{S} - S)(p_h - p)\|_{L^2(\Omega)} + \|(\tilde{S} - S) p\|_{L^2(\Omega)} \\ &\leq \left(c_2^C + c_2^D + c_2^S\right) \|p_h - p\|_{L^2(\Omega)} + \|(\tilde{S} - S) p\|_{L^2(\Omega)} \\ &\leq \left(c_2^C + c_2^D + c_2^S\right) c_1\, h^{\nu+1}\, |p|_{H^{\nu+1}(\Omega)} + c_3\, h^{\mu}\, |\tilde{\boldsymbol{u}}|_{H^{\mu+1}(\Omega)}\,, \end{aligned}$$

or

$$c_{\tilde{S}} \|p_h - \tilde{p}_h\|_{L^2(\Omega)} \leq c_4 c_1 h^{\nu+1} |p|_{H^{\nu+1}(\Omega)} + c_3 h^{\mu}\, |\tilde{\boldsymbol{u}}|_{H^{\mu+1}(\Omega)}\,, \tag{6.39}$$

which concludes the proof with $\alpha = (1 + c_4/c_{\tilde{S}}) c_1$ and $\beta = c_3/c_{\tilde{S}}$. □

We can now show an initial higher-order convergence for the pressure approximation under certain conditions. From the triangle and Young's inequalities and the estimate (6.36), we get

$$\frac{1}{2} \|p - \tilde{p}_h\|^2_{L^2(\Omega)} \leq \|p - p_h\|^2_{L^2(\Omega)} + \|p_h - \tilde{p}_h\|^2_{L^2(\Omega)} \leq \left(c_1 h^{\nu+1} |p|_{H^{\nu+1}(\Omega)}\right)^2 + \|p_h - \tilde{p}_h\|^2_{L^2(\Omega)}\,. \tag{6.40}$$

As in the previous proof we have

$$c_{\tilde{S}}\, \|p_h - \tilde{p}_h\|^2_{L^2(\Omega)} \leq \|(\tilde{S} - S) p_h\|_{L^2(\Omega)} \|p_h - \tilde{p}_h\|_{L^2(\Omega)}$$

and

$$\|(\tilde{S}-S)p_h\|_{L^2(\Omega)} \le c_1 c_4 h^{\nu+1}|p|_{H^{\nu+1}(\Omega)} + c_3 h^{\nu}|u|_{H^{\nu+1}(\Omega)}$$

for $\mu = \nu$. We also have

$$\|p_h - \tilde{p}_h\|_{L^2(\Omega)} \le \quad \|p_h - p\|_{L^2(\Omega)} + \|p - \tilde{p}_h\|_{L^2(\Omega)} \le \quad c_1\, h^{\nu+1}\,|p|_{H^{\nu+1}(\Omega)} + \|p - \tilde{p}_h\|_{L^2(\Omega)}\,,$$

so that

$$\begin{aligned}
&\|p_h - \tilde{p}_h\|^2_{L^2(\Omega)} \\
&\le \left[\frac{c_4 c_1}{c_{\tilde{S}}} h^{\nu+1}|p|_{H^{\nu+1}(\Omega)} + \frac{c_3}{c_{\tilde{S}}} h^{\nu}|\tilde{\boldsymbol{u}}|_{H^{\nu+1}(\Omega)}\right]\left[c_1 h^{\nu+1}|p|_{H^{\nu+1}(\Omega)} + \|p - \tilde{p}_h\|_{L^2(\Omega)}\right] \\
&= \frac{c_4}{c_{\tilde{S}}}\left(c_1 h^{\nu+1}|p|_{H^{\nu+1}(\Omega)}\right)^2 + \frac{c_3 c_1}{c_{\tilde{S}}} h^{2\nu+1}|p|_{H^{\nu+1}(\Omega)}|\tilde{\boldsymbol{u}}|_{H^{\nu+1}(\Omega)} + \\
&\left[\frac{c_4 c_1}{c_{\tilde{S}}} h^{\nu+1}|p|_{H^{\nu+1}(\Omega)} + \frac{c_3}{c_{\tilde{S}}} h^{\nu}|\tilde{\boldsymbol{u}}|_{H^{\nu+1}(\Omega)}\right]\|p - \tilde{p}_h\|_{L^2(\Omega)}\,.
\end{aligned}$$

Thus, due to (6.40) we get

$$\begin{aligned}
\frac{1}{2}\|p - \tilde{p}_h\|^2_{L^2(\Omega)} \le \left(1 + \frac{c_4}{c_{\tilde{S}}}\right)\left(c_1 h^{\nu+1}|p|_{H^{\nu+1}(\Omega)}\right)^2 + \frac{c_3 c_1}{c_{\tilde{S}}} h^{2\nu+1}|p|_{H^{\nu+1}(\Omega)}|\tilde{\boldsymbol{u}}|_{H^{\nu+1}(\Omega)} + \\
\left[\frac{c_4 c_1}{c_{\tilde{S}}} h^{\nu+1}|p|_{H^{\nu+1}(\Omega)} + \frac{c_3}{c_{\tilde{S}}} h^{\nu}|\tilde{\boldsymbol{u}}|_{H^{\nu+1}(\Omega)}\right]\|p - \tilde{p}_h\|_{L^2(\Omega)}\,.
\end{aligned}$$

Let us write

$$|\tilde{\boldsymbol{u}}|_{H^{\nu+1}(\Omega)} = |A^{-1}Bp|_{H^{\nu+1}(\Omega)} = c_{AB}|p|_{H^{\nu+1}(\Omega)}\,.$$

So, as long as

$$\left(c_4 c_1 h^{\nu+1} + c_{AB} c_3 h^{\nu}\right)|p|_{H^{\nu+1}(\Omega)} \le \frac{k c_{\tilde{S}}}{2}\|p - \tilde{p}_h\|_{L^2(\Omega)} \tag{6.41}$$

is satisfied for some $k < 1$, we get

$$\frac{1-k}{2}\|p - \tilde{p}_h\|^2_{L^2(\Omega)} \le \left(1 + \frac{c_4}{c_{\tilde{S}}}\right)\left(c_1 h^{\nu+1}|p|_{H^{\nu+1}(\Omega)}\right)^2 + \frac{c_3 c_1 c_{AB}}{c_{\tilde{S}}}\left(h^{\nu+\frac{1}{2}}|p|_{H^{\nu+1}(\Omega)}\right)^2,$$

so that we can finally conclude

$$\|p - \tilde{p}_h\|_{L^2(\Omega)} \le \left(c_I h^{\nu+1} + c_{II} h^{\nu+\frac{1}{2}}\right)|p|_{H^{\nu+1}(\Omega)}\,. \tag{6.42}$$

This estimate provides an explanation for the quadratic convergence observed in the previous numerical examples, see e.g. Figures 6.9 and 6.13. Although most assumptions made towards proving (6.42) are rather standard, this is not the case for condition (6.41). In fact, how can we interpret this condition?

For small h, the expression on the left-hand side of (6.41) behaves (on a logarithmic scale) as a line with slope ν. If $\|p - \tilde{p}_h\| = \mathcal{O}(h^{\nu+1/2})$ is assumed to hold for some range of h, we see that even *if* condition (6.41) is satisfied initially, the two lines (left- and right-hand sides) will eventually intersect as h decreases, and thus (6.41) will no longer hold. This is why estimate (6.42) shows only a possible *initial* higher-order convergence. As an alternative scenario, the curve with the higher slope may already start below the other curve, so that (6.41) will not hold for any h. Besides, due to the several constants in (6.41), *whether* and for *how long* this higher-order convergence holds may depend on various factors such as the problem (domain and solution) and the discretisation. Also for this reason, the higher slope might not break down at all within a practical range of mesh sizes. Interestingly, a similar initial higher-order behaviour can be observed (and proved) for boundary element methods when using the same polynomial degree to approximate the solution and boundary conditions [118].

7 NON-NEWTONIAN SPLIT-STEP METHODS

The stabilisation methods presented in Chapter 6 can be easily extended to time-dependent problems by simply adding the acceleration term $\partial_t \boldsymbol{u}$ to the momentum residual and then applying an appropriate temporal discretisation. In this chapter, however, we aim to further exploit the pressure Poisson framework developed in Chapter 5 to design efficient split-step schemes for generalised Newtonian flow problems. Time-splitting or split-step methods are stepping schemes that decouple the computation of pressure and velocity. This is highly advantageous especially when employing iterative solvers, since the decoupled blocks have a simple structure and can thus be easily preconditioned. The most popular split-step schemes are the so-called projection methods where incompressibility of the discrete velocity field is enforced through a Helmholtz-Leray projection. The first generation of these methods were plagued by nonphysical pressure boundary conditions that induced severe numerical boundary layers and spoiled the order of accuracy. Timmermans et al. [119] solved this issue by introducing the so-called rotational pressure-correction scheme that adds a correction term to the pressure update. In one of the rather scarce theoretical studies that are not restricted to the pure Dirichlet case, Guermond et al. [120] showed that in three-dimensional problems with natural BCs, the rotational projection method has an intrinsic contradiction: the factor multiplying the added correction term should be taken as equal to 1 to attain consistent pressure BCs, but must be less than 2/3 to guarantee stability. Although this does not spoil the asymptotic order of convergence *per se*, remedies have been proposed to increase the accuracy of the pressure approximation on the boundaries [121]. An excellent overview of projection methods can be found in the works of Guermond, Minev and Shen [120, 122].

An alternative approach was presented by Liu [71], extending the pressure Poisson method of Johnston and Liu [72] to the more realistic setting where open/traction boundaries are allowed. The method completely replaces the continuity equation by a pressure Poisson problem with consistent boundary conditions. Furthermore, by treating the convective term explicitly, the scheme decouples also the velocity components from each other, leading to a sequence of scalar problems that can be efficiently solved. Several formulations building up from their framework have emerged in the past decade and have proven to be powerful tools in the efficient solution of incompressible flow problems [102–109].

Extending split-step schemes to generalised Newtonian fluids is not straightforward, especially in a finite element framework. In fact, only very recently have the first steps in this direction been taken. Deteix and Yakoubi [123] started by extending the popular rotational projection method to fluids with non-homogeneous viscosity. A more general

setting allowing natural boundary conditions was then formulated by Plasman et al. [124]. Yet, when the viscosity is not only variable but also dependent on the velocity gradient, the divergence of the stress tensor will not be regular (smooth) enough to be incorporated directly into the pressure correction step. One way around that is to project the viscous stress tensor onto a continuous space, as done by Deteix and Yakoubi [125] in their recently introduced shear rate projection (SRP) schemes. Despite being very accurate and simple, the SRP method has a high cost when compared to standard (Newtonian) pressure correction schemes: in three dimensions, it requires the solution of a vector-valued convection-diffusion problem, two Poisson equations and at least ten scalar mass matrix problems (for adding quantities from different vector spaces). Moreover, the SRP method does not allow equal-order velocity-pressure pairs, i.e., the LBB constraint is still imperative. For these reasons, the method can be rather expensive in practical applications.

In this context, we show next how to use our non-Newtonian pressure Poisson formulation to construct a split-step framework with consistent Dirichlet and Neumann pressure BCs, reduced computational cost, very good accuracy and stability properties, while still allowing equal-order finite element pairs. We further show that, by treating the rheological law and the viscous stress appropriately, it is possible to decouple the velocity components to end up with a scheme that requires the solution of one Poisson equation, one scalar projection step and d scalar advection-diffusion equations. The corresponding results are published as a research article [126].

7.1 Strong problem and weak formulation

We start by replacing the classical momentum-mass system (3.1)–(3.5) by the alternative initial-boundary value problem (IBVP)

$$\rho[\partial_t \boldsymbol{u} + (\nabla \boldsymbol{u})\boldsymbol{u}] - \mu[\Delta \boldsymbol{u} + \alpha \nabla(\nabla \cdot \boldsymbol{u})] - 2\nabla^s \boldsymbol{u} \nabla \mu + \nabla p = \boldsymbol{f} \qquad \text{in } \Omega \times (0,T], \quad (7.1)$$

$$-\Delta p + \nabla \cdot [2\nabla^s \boldsymbol{u} \nabla \mu - (\rho \nabla \boldsymbol{u})\boldsymbol{u}] - [\nabla \times (\nabla \times \boldsymbol{u})] \cdot \nabla \mu = -\nabla \cdot \boldsymbol{f} \qquad \text{in } \Omega \times [0,T], \quad (7.2)$$

$$\boldsymbol{u} = \boldsymbol{g} \qquad \text{on } \Gamma_D \times (0,T], \quad (7.3)$$

$$\left[\mu \nabla \boldsymbol{u} + (\alpha \mu \nabla \boldsymbol{u})^\top - p\mathbb{I}\right] \boldsymbol{n} = \boldsymbol{h} \qquad \text{on } \Gamma_N \times (0,T], \quad (7.4)$$

$$\boldsymbol{u} = \boldsymbol{u}_0 \qquad \text{at } t = 0, \quad (7.5)$$

$$\nabla \cdot \boldsymbol{u}_0 = 0 \qquad \text{in } \Omega, \quad (7.6)$$

$$p = \zeta(\boldsymbol{u}) \qquad \text{on } \Gamma_N \times [0,T], \quad (7.7)$$

$$\frac{\partial p}{\partial n} = \lambda(\boldsymbol{u}) \qquad \text{on } \Gamma_D \times [0,T], \quad (7.8)$$

where

$$\zeta(\boldsymbol{u}) := (1+\alpha)\mu \nabla \boldsymbol{u} : (\boldsymbol{n} \otimes \boldsymbol{n} - \mathbb{I}) - \boldsymbol{h} \cdot \boldsymbol{n}, \quad (7.9)$$

$$\lambda(\boldsymbol{u}) := [\boldsymbol{f} - \rho \partial_t \boldsymbol{g} - (\rho \nabla \boldsymbol{u})\boldsymbol{u} + 2\nabla^s \boldsymbol{u} \nabla \mu - \mu \nabla \times (\nabla \times \boldsymbol{u})] \cdot \boldsymbol{n}, \quad (7.10)$$

and α is either 1 for the stress-divergence formulation or 0 for the generalised Laplacian one. This IBVP may seem more complex than the original one, but we shall soon see how it can be used for constructing simple finite element formulations requiring only the solution of Poisson and convection-diffusion problems. Note that, for the homogeneous Newtonian case, all terms depending on $\nabla\mu$ vanish and the formulation by Liu [71] is recovered.

Theorem 7.1. *For sufficiently regular p,$\boldsymbol{u}$,$\boldsymbol{f}$,$\boldsymbol{g}$ and $\boldsymbol{h}$, systems* (7.1)–(7.8) *and* (3.1)–(3.5) *are equivalent.*

Proof. The proof is somewhat similar to what was done in Chapter 6, but with some key differences due to the time-dependent terms and mixed BCs. We will first show that (3.1)–(3.5) imply (7.1)–(7.8). We obtain the Neumann BC (7.8) by dotting the momentum equation with the normal vector $\boldsymbol{n}$, restricting the result to Γ_D and using the relation

$$\Delta\boldsymbol{u} \equiv \nabla(\nabla\cdot\boldsymbol{u}) - \nabla\times(\nabla\times\boldsymbol{u}) = -\nabla\times(\nabla\times\boldsymbol{u})\,.$$

Similarly, the PPE (7.2) is obtained by taking (minus) the divergence of the momentum equation:

$$\begin{aligned}-\Delta p + \nabla\cdot\left[2\nabla^s\boldsymbol{u}\nabla\mu - (\rho\nabla\boldsymbol{u})\boldsymbol{u}\right] + \nabla\cdot\boldsymbol{f} &= \nabla\cdot(\rho\partial_t\boldsymbol{u}) - \Delta\boldsymbol{u}\cdot\nabla\mu - \alpha\nabla\cdot\left[\mu\nabla(\nabla\cdot\boldsymbol{u})\right]\\ &= \rho\partial_t(\nabla\cdot\boldsymbol{u}) + [\nabla\times(\nabla\times\boldsymbol{u}) - \nabla(\nabla\cdot\boldsymbol{u})]\cdot\nabla\mu\\ &= [\nabla\times(\nabla\times\boldsymbol{u})]\cdot\nabla\mu\,.\end{aligned}$$

To obtain the pressure Dirichlet BC (7.7), we first dot Eq. (3.4) by $\boldsymbol{n}$ to get

$$\begin{aligned}\boldsymbol{h}\cdot\boldsymbol{n} &= \left\{\left[\mu\nabla\boldsymbol{u} + (\alpha\mu\nabla\boldsymbol{u})^\top - p\mathbb{I}\right]\boldsymbol{n}\right\}\cdot\boldsymbol{n}\\ &\equiv (1+\alpha)\mu\nabla\boldsymbol{u} : \boldsymbol{n}\otimes\boldsymbol{n} - p\boldsymbol{n}\cdot\boldsymbol{n}\\ &= (1+\alpha)\mu\nabla\boldsymbol{u} : \boldsymbol{n}\otimes\boldsymbol{n} - p\,.\end{aligned}$$

Then, we can arbitrarily subtract $(1+\alpha)\mu\nabla\cdot\boldsymbol{u}$ from the right-hand side and restrict the result to Γ_N, which finally yields Eq. (7.7). The additional condition (7.6) is simply the restriction of the incompressibility constraint to $t = 0$, which completes the first part of the proof.

To prove the other direction, i.e, that (7.1)–(7.8) implies (3.1)–(3.5), we first take the divergence of Eq. (7.1) and add the result to Eq. (7.2), which gives us

$$\begin{aligned}0 &= \nabla\cdot(\rho\partial_t\boldsymbol{u}) - \mu[\nabla\cdot(\Delta\boldsymbol{u}) + \alpha\Delta(\nabla\cdot\boldsymbol{u})] - [\nabla\times(\nabla\times\boldsymbol{u})]\cdot\nabla\mu - \nabla\mu\cdot[\Delta\boldsymbol{u} + \alpha\nabla(\nabla\cdot\boldsymbol{u})]\\ &\equiv \rho\partial_t(\nabla\cdot\boldsymbol{u}) - (1+\alpha)\mu\Delta(\nabla\cdot\boldsymbol{u}) - (1+\alpha)\nabla\mu\cdot[\nabla(\nabla\cdot\boldsymbol{u})]\,,\end{aligned} \tag{7.11}$$

i.e., for the variable $\phi := \nabla\cdot\boldsymbol{u}$ we get the heat equation

$$\partial_t\phi - (1+\alpha)\nabla\cdot(\nu\nabla\phi) = 0\,, \tag{7.12}$$

where $\nu = \mu/\rho$ is the kinematic viscosity. Zero initial condition for ϕ is guaranteed by (7.6), while we can obtain Neumann BCs by dotting Eq. (7.1) with $\boldsymbol{n}$, restricting the result to Γ_D and subtracting from (7.8), which gives

$$\begin{aligned} 0 &= \mu \boldsymbol{n} \cdot [\Delta \boldsymbol{u} + (\nabla \times \nabla \times \boldsymbol{u}) + \alpha \nabla (\nabla \cdot \boldsymbol{u})] \\ &\equiv (1+\alpha)\mu \boldsymbol{n} \cdot [\nabla (\nabla \cdot \boldsymbol{u})] = (1+\alpha)\mu \frac{\partial \phi}{\partial n}, \end{aligned}$$

that is,

$$\frac{\partial \phi}{\partial n} \text{ on } \Gamma_D, \tag{7.13}$$

since $(1+\alpha)\mu \neq 0$. Dirichlet BCs for ϕ on Γ_N come from dotting (7.4) with $\boldsymbol{n}$ and adding the result to (7.7), which yields

$$0 = (1+\alpha)\mu \nabla \boldsymbol{u} : \mathbb{I} = (1+\alpha)\mu \phi \text{ on } \Gamma_N, \tag{7.14}$$

so that $\phi|_{\Gamma_N} = 0$. We thus get $\phi \equiv 0$, that is, our modified system also enforces incompressibility. With mass conservation proved, the equivalence between the reduced momentum equation (7.1) and the standard one (3.1) is straightforward, concluding the proof. □

As we have seen before, the most challenging aspect when dealing with a non-Newtonian pressure Poisson equation is the treatment of the viscous term. Fortunately, all the effort done in Chapter 5 to design a C^0-compatible weak formulation can be directly transferred to the present setting. The corresponding weak PPE is

$$\langle \nabla q, \nabla p \rangle_{L^2(\Omega)} = \left\langle \nabla q, \boldsymbol{f} - (\rho \nabla \boldsymbol{u})\boldsymbol{u} + 2(\nabla \boldsymbol{u})^\top \nabla \mu \right\rangle_{L^2(\Omega)} + \langle \boldsymbol{n} \times \nabla q, \mu \nabla \times \boldsymbol{u} \rangle_\Gamma - \langle q, \rho \partial_t (\boldsymbol{n} \cdot \boldsymbol{g}) \rangle_{\Gamma_D}$$

with the acceleration term reduced to a boundary integral depending only on the normal velocity datum. Mind that the time derivative of $\boldsymbol{g}$ is often known *a priori*. For instance, it is common practice to fit patient-specific inflow data using Fourier series [57], which allows an analytical computation of $\partial_t \boldsymbol{g}_h$. When this is not possible, finite differences can be used to approximate the time derivative.

Lemma 7.2. *For $\boldsymbol{v} \in [L^2(\Gamma)]^d$ and q such that $\boldsymbol{n} \times \nabla q \in L^2(\Gamma)$ and $q|_{\Gamma_N} = 0$, there holds*

$$\langle \boldsymbol{n} \times \nabla q, \boldsymbol{v} \rangle_\Gamma = \langle \boldsymbol{n} \times \nabla q, \boldsymbol{v} \rangle_{\Gamma_D}. \tag{7.15}$$

Proof. The gradient ∇q on Γ can be decomposed into normal and tangential parts:

$$\nabla q = \left(\frac{\partial q}{\partial n} \right) \boldsymbol{n} + \nabla_\tau q = (\boldsymbol{n} \cdot \nabla q)\, \boldsymbol{n} + (\boldsymbol{n} \times \nabla q) \times \boldsymbol{n}.$$

Since $q|_{\Gamma_N} = 0$, the tangential derivative $\nabla_\tau q$ will also be zero on Γ_N. Thus, taking the left cross product with $\boldsymbol{n}$ and restricting the result to Γ_N gives us

$$(\boldsymbol{n} \times \nabla q)\,|_{\Gamma_N} = \left[\left(\frac{\partial q}{\partial n}\right)\boldsymbol{n} \times \boldsymbol{n}\right]\Big|_{\Gamma_N} + (\boldsymbol{n} \times \nabla_\tau q)\,|_{\Gamma_N} = \boldsymbol{0}\,.$$

Hence,

$$\langle \boldsymbol{n} \times \nabla q, \boldsymbol{v}\rangle_\Gamma = \langle \boldsymbol{n} \times \nabla q, \boldsymbol{v}\rangle_{\Gamma_D} + \langle \boldsymbol{n} \times \nabla q, \boldsymbol{v}\rangle_{\Gamma_N} = \langle \boldsymbol{n} \times \nabla q, \boldsymbol{v}\rangle_{\Gamma_D}\,,$$

as we wanted to prove. □

Thus, we can further simplify the right-hand side of the PPE to

$$\Big\langle \nabla q, \boldsymbol{f} - (\rho \nabla \boldsymbol{u})\boldsymbol{u} + 2(\nabla \boldsymbol{u})^\top \nabla \mu \Big\rangle_{L^2(\Omega)} + \langle \boldsymbol{n} \times \nabla q, \mu \nabla \times \boldsymbol{u}\rangle_{\Gamma_D} - \langle q, \rho \partial_t (\boldsymbol{n} \cdot \boldsymbol{g})\rangle_{\Gamma_D}\,.$$

Another distinct aspect with respect to the pressure Poisson formulations from Chapters 5 and 6 is the Dirichlet BC for the pressure. When enforcing (7.7) on a certain section of the outflow boundary Γ_N, the quantity $\zeta := (1+\alpha)\mu \nabla \boldsymbol{u} : (\boldsymbol{n} \otimes \boldsymbol{n} - \mathbb{I}) - \boldsymbol{h} \cdot \boldsymbol{n}$ will be discontinuous in the discrete case and, thus, not well defined at the pressure nodes we want to fix. The solution proposed by Liu [71] and also used by Plasman et al. [124] is to project ζ onto Γ_N such that the resulting quantity $\hat{\zeta}$ is continuous on each section of Γ_N. The cost of this projection on Γ_N is negligible in comparison to the other steps of the overall scheme. On the other hand, if an ultra-weak framework is considered for the pressure Poisson problem, then the Dirichlet BCs are enforced weakly and, therefore, the discontinuity of ζ is not an issue. In other words, the double integration by parts leads to

$$-\int_\Omega p \Delta q \,\mathrm{d}\Omega + \int_{\Gamma_N} \frac{\partial q}{\partial n} \underbrace{p}_{=\,\zeta(\boldsymbol{u})} \mathrm{d}\Gamma - \int_{\Gamma_D} q \underbrace{\frac{\partial p}{\partial n}}_{=\,\lambda(\boldsymbol{u})} \mathrm{d}\Gamma$$

with the test functions q taken in $Y = \left\{ q \in H^1_\Delta(\Omega) :\ \boldsymbol{n} \cdot \nabla q = 0 \text{ on } \Gamma_D \ \text{ and } \ q = 0 \text{ on } \Gamma_N \right\}$.

7.2 Efficient iteration-free split-step schemes

We are interested here in decoupling velocity and pressure in order to enable efficient solutions, and therefore the pressure term in the momentum equation will be treated explicitly. Moreover, to further improve efficiency, we will focus on schemes that decouple also the velocity components. In the Newtonian case, this can be achieved by simply treating convection explicitly, whereas the viscous term can be kept implicit [72]. This results in problems which are not only smaller but also linearised, so that there is no need for iterative methods. However, in the presence of nonlinear viscosity, it is necessary to treat the viscous term appropriately in order to keep the velocity components decoupled, as we will show next.

7.2.1 A first-order scheme

Let us start by considering a first-order backward differentiation formula (BDF1) in time. In order to include both stress-divergence and generalised Laplacian formulations in one framework, let us write the viscous trilinear form as

$$\langle \nabla \boldsymbol{w}, \mu \nabla \boldsymbol{u} \rangle_{L^2(\Omega)} + (\alpha - 1) \left\langle \boldsymbol{w}, (\nabla \boldsymbol{u})^\top \nabla \mu \right\rangle_\Omega + \alpha \left\langle \mu \nabla \boldsymbol{w}, (\nabla \boldsymbol{u})^\top \right\rangle_{L^2(\Omega)},$$

where the last term vanishes for the generalised Laplacian form ($\alpha = 0$), while the middle one vanishes in the stress-divergence case ($\alpha = 1$). Whichever term remains would end up coupling the velocity components even with a linearised viscosity. Therefore, we treat such terms explicitly, whereas for the weak Laplacian term $\mu \nabla \boldsymbol{u} : \nabla \boldsymbol{w}$ we use a linearised viscosity and the current velocity. When it comes to convection, there are two approaches that allow the decoupling: one is to treat the convective term explicitly [72], and the other one is to use a linearised convective velocity with the current velocity gradient. In the (temporally) first-order case, this leads to the problem of finding $\boldsymbol{u}^{n+1} \in \left[X_h^u\right]^d$, with $\boldsymbol{u}^{n+1}|_{\Gamma_D} = \boldsymbol{g}_h^{n+1}$, such that

$$\begin{aligned} \left\langle \boldsymbol{w}, (\rho \nabla \boldsymbol{u}^{n+1}) \boldsymbol{u}^n + \frac{\rho}{\Delta t} \boldsymbol{u}^{n+1} \right\rangle_\Omega + \left\langle \nabla \boldsymbol{w}, \mu^n \nabla \boldsymbol{u}^{n+1} \right\rangle_{L^2(\Omega)} = -\alpha \left\langle \mu^n \nabla \boldsymbol{w}, (\nabla \boldsymbol{u}^n)^\top \right\rangle_{L^2(\Omega)} + \\ \left\langle \boldsymbol{w}, \boldsymbol{f}^{n+1} + \frac{\rho}{\Delta t} \boldsymbol{u}^n + (1 - \alpha) \left(\nabla \boldsymbol{u}^n\right)^\top \nabla \mu^n \right\rangle_\Omega + \langle \nabla \cdot \boldsymbol{w}, p^n \rangle_{L^2(\Omega)} + \langle \boldsymbol{w}, \boldsymbol{h}^{n+1} \rangle_{\Gamma_N} \end{aligned}$$

for all $\boldsymbol{w} \in \left[X_h^u\right]^d$, with $\boldsymbol{w}|_{\Gamma_D} = \boldsymbol{0}$. We drop the subscript h to easen the notation. Notice that this equation, along with the PPE and the viscosity projection, are linear algebraic systems, so that there is no need to iterate in order to find the solution. The overall first-order algorithm can be summarised as follows:

1. *Initialisation:*
   Compute the initial viscosity from $\boldsymbol{u}_0$, then the initial pressure using the PPE.

2. *Convection-diffusion steps:*
   For each of the d velocity components, solve the convection-diffusion problem of finding $u_i^{n+1} \in X_h^u$, with $u_i^{n+1}|_{\Gamma_D} = g_i^{n+1}$, such that

$$\begin{aligned} \left\langle w, \rho \boldsymbol{u}^n \cdot \nabla u_i^{n+1} + \frac{\rho}{\Delta t} u_i^{n+1} \right\rangle_\Omega + \left\langle \nabla w, \mu^n \nabla u_i^{n+1} \right\rangle_{L^2(\Omega)} = \left\langle \frac{\partial w}{\partial x_i}, p^n \right\rangle_{L^2(\Omega)} + \\ \left\langle w, f_i^{n+1} + \frac{\rho}{\Delta t} u_i^n + (1 - \alpha) \frac{\partial \boldsymbol{u}^n}{\partial x_i} \cdot \nabla \mu^n \right\rangle_\Omega - \alpha \left\langle \nabla w, \mu^n \frac{\partial \boldsymbol{u}^n}{\partial x_i} \right\rangle_{L^2(\Omega)} + \left\langle w, h_i^{n+1} \right\rangle_{\Gamma_N} \end{aligned} \tag{7.16}$$

   for all $w \in X_h^u$, with $w|_{\Gamma_D} = 0$.

3. *Viscosity projection:*
   Find $\mu^{n+1} \in X_h^\mu$ such that

$$\left\langle \upsilon, \mu^{n+1} \right\rangle_{L^2(\Omega)} = \left\langle \upsilon, \eta\left(\dot{\gamma}\left(\nabla^s \boldsymbol{u}^{n+1}\right)\right)\right\rangle_{L^2(\Omega)} \tag{7.17}$$

   for all $\upsilon \in X_h^\mu$.

4. *Pressure BC projection (only if $\Gamma_N \neq \emptyset$):*
   Project $\zeta^{n+1} := (1+\alpha)\mu^{n+1}\nabla \boldsymbol{u}^{n+1} : [\boldsymbol{n}\otimes\boldsymbol{n} - \mathbb{I}] - \boldsymbol{n}\cdot\boldsymbol{h}^{n+1}$ such that the resulting quantity $\hat{\zeta}^{n+1}$ is continuous on Γ_N.

5. *Pressure Poisson step:*
   Find $p^{n+1} \in X_h^p$, with $p^{n+1}|_{\Gamma_N} = \hat{\zeta}^{n+1}$, such that

$$\begin{aligned}\left\langle \nabla q, \nabla p^{n+1} \right\rangle_{L^2(\Omega)} = &\left\langle \nabla q, \boldsymbol{f}^{n+1} - (\rho\nabla \boldsymbol{u}^{n+1})\boldsymbol{u}^{n+1} + 2(\nabla \boldsymbol{u}^{n+1})^\top \nabla \mu^{n+1} \right\rangle_{L^2(\Omega)} \\ &+ \left\langle \boldsymbol{n}\times\nabla q, \mu^{n+1}\nabla\times \boldsymbol{u}^{n+1}\right\rangle_{\Gamma_D} - \left\langle q, \rho\boldsymbol{n}\cdot\partial_t \boldsymbol{g}_h^{n+1}\right\rangle_{\Gamma_D}\end{aligned} \tag{7.18}$$

   for all $q \in X_h^p$, with $q|_{\Gamma_N} = 0$.

Note that the pressure Poisson step is fully implicit, which is crucial for accuracy and stability [71]. When normal acceleration data are not analytically available, we can approximate

$$\left\langle q, \rho\boldsymbol{n}\cdot\partial_t \boldsymbol{g}_h^{n+1}\right\rangle_{\Gamma_D} \approx \left\langle q, \frac{\rho}{\Delta t}\left(\boldsymbol{g}^{n+1} - \boldsymbol{g}^n\right)\cdot\boldsymbol{n}\right\rangle_{\Gamma_D}, \tag{7.19}$$

or using higher-order finite differences matching the temporal order of the overall scheme.

Matrix problem

Let us denote by $\underline{u}_k^n$ the vector of nodal values of the k-th velocity component at the n-th time step – and analogously for $\underline{p}^n$ and $\underline{\mu}^n$. The main steps of the first-order marching scheme we just described can be written in matrix form as

$$\left[\mathbf{M}^\mu + \mathbf{C}(\boldsymbol{u}^n) + \mathbf{K}^u(\mu^n)\right]\underline{u}_k^{n+1} = \underline{f}^{n+1} + \mathbf{M}^\mu \underline{u}_k^n + \left[(1-\alpha)\mathbf{A}^k(\boldsymbol{u}^n) - \alpha\mathbf{D}^k(\boldsymbol{u}^n)\right]\underline{\mu}^n + (\mathbf{B}^k)^\top \underline{p}^n$$
$$\text{for } k = 1,\ldots,d,$$
$$\mathbf{M}^\mu \underline{\mu}^{n+1} = \underline{r}(\boldsymbol{u}^{n+1}),$$
$$\mathbf{K}^p \underline{p}^{n+1} = \underline{g}^{n+1} + \left[\boldsymbol{S}(\boldsymbol{u}^{n+1}) + 2\sum_{k=1}^d \tilde{\mathbf{A}}^k(\boldsymbol{u}^{n+1})\right]\underline{\mu}^{n+1} - \sum_{k=1}^d \left[\tilde{\mathbf{C}}^k(\boldsymbol{u}^{n+1})\right]\underline{u}_k^{n+1},$$

where the vectors $\underline{f}$ and $\underline{g}$ appropriately include the effects of body forces and BCs, and the remaining matrices are given as

$$
\begin{aligned}
M^u_{ij} &= \frac{1}{\Delta t}\left\langle \psi^u_i, \rho\psi^u_j \right\rangle_\Omega , & M^\mu_{ij} &= \left\langle \psi^\mu_i, \psi^\mu_j \right\rangle_\Omega , \\
K^u_{ij}(\mu) &= \left\langle \nabla\psi^u_i, \mu\nabla\psi^u_j \right\rangle_\Omega , & K^p_{ij} &= \left\langle \nabla\psi^p_i, \nabla\psi^p_j \right\rangle , \\
C_{ij}(\boldsymbol{u}) &= \left\langle \psi^u_i, \rho\boldsymbol{u}\cdot\nabla\psi^u_j \right\rangle_\Omega , & \tilde{C}^k_{ij}(\boldsymbol{u}) &= \left\langle \frac{\partial\psi^p_i}{\partial x_k}, \rho\boldsymbol{u}\cdot\nabla\psi^u_j \right\rangle_\Omega , \\
A^k_{ij}(\boldsymbol{u}) &= \left\langle \psi^u_i, \frac{\partial\boldsymbol{u}}{\partial x_k}\cdot\nabla\psi^\mu_j \right\rangle_\Omega , & \tilde{A}^k_{ij}(\boldsymbol{u}) &= \left\langle \frac{\partial\psi^p_i}{\partial x_k}, \frac{\partial\boldsymbol{u}}{\partial x_k}\cdot\nabla\psi^\mu_j \right\rangle_\Omega , \\
D^k_{ij}(\boldsymbol{u}) &= \left\langle \nabla\psi^u_i\cdot\frac{\partial\boldsymbol{u}}{\partial x_k}, \psi^\mu_j \right\rangle_\Omega , & S_{ij}(\boldsymbol{u}) &= \left\langle \boldsymbol{n}\times\nabla\psi^p_i, \psi^\mu_j\nabla\times\boldsymbol{u} \right\rangle_{\Gamma_D} , \\
B^k_{ij} &= \left\langle \psi^p_i, \frac{\partial\psi^u_j}{\partial x_k} \right\rangle_\Omega . &&
\end{aligned}
$$

Therefore, all we need to solve at each time step are d scalar convection-diffusion problems, one scalar mass matrix and one Poisson problem. Also note that not only are the velocity components decoupled, but their system matrices are all identical. This simplifies computations and reduces assembling costs. Furthermore, one may further improve efficiency by lumping the mass matrix $\mathbf{M}^\mu$ in the viscosity projection step. This essentially eliminates the cost due to introducing the viscosity as an additional unknown, without jeopardising stability and accuracy.

7.2.2 Improving the conservation of mass

It is clear that when the direct incompressibility constraint is replaced by the PPE, in the discrete case the resulting velocity will not be divergence-free, which is in principle not an issue. Yet, as observed by Liu et al. [102], in problems with non-smooth solutions one can considerably improve stability by performing a standard Leray projection, as done in classical pressure correction methods [120, 122]. After computing the velocity field $\boldsymbol{u}$ from Eq. (7.16), we can solve the Poisson problem

$$-\Delta\varphi = \nabla\cdot\boldsymbol{u} \quad \text{in } \Omega, \tag{7.20}$$

$$\frac{\partial\varphi}{\partial n} = 0 \quad \text{on } \Gamma_D, \tag{7.21}$$

$$\varphi = 0 \quad \text{on } \Gamma_N, \tag{7.22}$$

so that the modified velocity $\hat{\boldsymbol{u}} := \boldsymbol{u} + \nabla\varphi$ satisfies

$$\begin{aligned} \nabla \cdot \hat{\boldsymbol{u}} &= 0 \ \text{ in } \ \Omega, \\ \hat{\boldsymbol{u}} \cdot \boldsymbol{n} &= \boldsymbol{u} \cdot \boldsymbol{n} \ \text{ on } \ \Gamma_D, \\ \hat{\boldsymbol{u}} \cdot \boldsymbol{s} &= \boldsymbol{u} \cdot \boldsymbol{s} \ \text{ on } \ \Gamma_N, \end{aligned}$$

for any tangential vector $\boldsymbol{s}$ on Γ_N. In other words, we would end up with one velocity field $\boldsymbol{u}$ that is not divergence-free but fully satisfies the Dirichlet BCs, and another field $\hat{\boldsymbol{u}}$ that is divergence-free but only partially satisfies the prescribed BCs. As discussed by Guermond et al. [122], both velocity fields are expected to converge with the same rates, such that from an accuracy standpoint there is no objective reason to pick one over the other. The reason for performing the projection here is to keep divergence errors from potentially building up in time due to spatial discretisation errors (see Ref. [102] for details). Also notice that when using standard Lagrangian finite element spaces for φ, the resulting $\hat{\boldsymbol{u}}$ will be discontinuous. Therefore, the modified velocity has to be further projected onto a continuous space before it can be used in subsequent steps. This requires the additional solution of d scalar mass matrix problems and renders the resulting projected velocity only *weakly* divergence-free.

Remark 7.1. *A key difference between the present framework and standard pressure correction methods is that here the projection step does not induce any artificial pressure boundary conditions, since we compute the pressure directly via the PPE instead of using φ to update it.*

In light of the shortcomings regarding the Leray projection, we use an approach that offers a compromise between the two variants discussed so far. As noted by Liu [71], if we apply the Leray projection always to the previous velocity $\boldsymbol{u}^n$ and use the modified velocity $\hat{\boldsymbol{u}}^n$ only in the acceleration term of the momentum equation, we can eliminate the computational overhead due to the projection. More precisely, for the first-order scheme in time we write

$$\partial_t \boldsymbol{u}|_{t=t^{n+1}} \approx \frac{1}{\Delta t}\left(\boldsymbol{u}^{n+1} - \hat{\boldsymbol{u}}^n\right),$$

which leads to

$$\frac{\rho}{\Delta t}\left[\boldsymbol{u}^{n+1} - (\boldsymbol{u}^n + \nabla\varphi^n)\right] + \nabla p^n + \boldsymbol{r}^{n+1,n} = \boldsymbol{f}^{n+1},$$

where in $\boldsymbol{r}^{n+1,n}$ we group the nonlinear terms, for concision. We can combine p^n and φ^n appropriately to yield

$$\frac{\rho}{\Delta t}\left(\boldsymbol{u}^{n+1} - \boldsymbol{u}^n\right) + \nabla \hat{p}^n + \boldsymbol{r}^{n+1,n} = \boldsymbol{f}^{n+1}, \tag{7.23}$$

with

$$\hat{p}^n := p^n - \frac{\rho}{\Delta t}\varphi^n. \tag{7.24}$$

Notice that this circumvents the need for projecting $\hat{\boldsymbol{u}}^n$ onto a continuous space, since the acceleration term has no spatial derivatives. We can further eliminate the additional Poisson step by combining Eqs. (7.20)–(7.22) with the original pressure Poisson problem (7.2)–(7.8) into a Poisson equation for the modified pressure $\hat{p}$:

$$-\Delta\hat{p}^n = [\nabla\times(\nabla\times\boldsymbol{u}^n)]\cdot\nabla\mu^n - \nabla\cdot[2\nabla^s\boldsymbol{u}^n\nabla\mu^n - (\rho\nabla\boldsymbol{u}^n)\boldsymbol{u}^n] - \nabla\cdot\boldsymbol{f}^n - \frac{\rho}{\Delta t}\nabla\cdot\boldsymbol{u}^n, \quad (7.25)$$

with the same boundary conditions as in the original PPE, since φ has zero Dirichlet and Neumann BCs. It is also worth remarking that, since φ is zero for the exact solution, the quantity $\hat{p}$ is still a consistent approximation for the pressure. Therefore, for the first-order scheme the only modification needed with respect to the basic algorithm (7.16)–(7.18) is to add to the right-hand side of the PPE the term $(-\rho/\Delta t)\nabla\cdot\boldsymbol{u}^{n+1}$, which on the matrix level becomes

$$-\frac{\rho}{\Delta t}\sum_{k=1}^{d}\mathbf{B}^k\underline{u}_k^{n+1}.$$

This technique is sometimes referred to as *divergence damping* [105, 108, 127], as it can be seen as penalising the PPE with nonzero values of the velocity divergence. This simple approach considerably improves mass conservation and temporal stability. In the next subsection we present the generalisation to higher-order, potentially adaptive temporal discretisations.

7.2.3 Higher-order schemes with variable time step

It can be desirable, especially when using higher-order finite element spaces, to also increase the temporal order of discretisation, and in particular allowing variable time steps $\Delta t^n = t^{n+1} - t^n$, for efficiency. This can be attained by using a combination of higher-order backward differentiation schemes

$$\partial_t\boldsymbol{u}|_{t=t^{n+1}} \approx \alpha_0^m\boldsymbol{u}^{n+1} + \sum_{j=1}^{m}\alpha_j^m\hat{\boldsymbol{u}}^{n+1-j}$$

and suitable extrapolation formulas

$$\boldsymbol{u}^{n+1} \approx \boldsymbol{u}^\star := \sum_{j=1}^{m}\beta_j^m\boldsymbol{u}^{n+1-j} \quad (7.26)$$

of order m with coefficients α_j^m and β_j^m exemplarily given in Table 7.1 for $m = 2$. The modified pressure is now defined as

$$\hat{p}^\star := p^\star + \rho\sum_{j=1}^{m}\alpha_j^m\varphi^{n+1-j}, \quad (7.27)$$

Table 7.1: Backward differentiation and extrapolation coefficients of order $m = 2$ [128].

j	0	1	2
α_j^m	$\frac{2\Delta t^n+\Delta t^{n-1}}{\Delta t^n(\Delta t^n+\Delta t^{n-1})}$	$-\frac{\Delta t^n+\Delta t^{n-1}}{\Delta t^n\Delta t^{n-1}}$	$\frac{\Delta t^n}{\Delta t^{n-1}(\Delta t^n+\Delta t^{n-1})}$
β_j^m	–	$1+\frac{\Delta t^n}{\Delta t^{n-1}}$	$-\frac{\Delta t^n}{\Delta t^{n-1}}$

incorporating both the extrapolated pressure and projection contribution to past velocities. Let us write the discretised right-hand side of the weak PPE at time t^{n+1} as

$$l(\boldsymbol{u}^{n+1},\mu^{n+1},q) = \left\langle \nabla q, \boldsymbol{f}^{n+1} - (\rho\nabla\boldsymbol{u}^{n+1})\boldsymbol{u}^{n+1} + 2(\nabla\boldsymbol{u}^{n+1})^\top\nabla\mu^{n+1}\right\rangle_{L^2(\Omega)} + \left\langle \boldsymbol{n}\times\nabla q, \mu^{n+1}\nabla\times\boldsymbol{u}^{n+1}\right\rangle_{\Gamma_D} - \langle q, \rho\boldsymbol{n}\cdot\partial_t\boldsymbol{g}_h\rangle_{\Gamma_D}.$$

We can insert the definition (7.27) and linearly combine PPEs similarly to Eq. (7.25) to obtain an equation for the modified pressure $\hat{p}^\star$ to be used in the next time step:

$$\begin{aligned}\left\langle \nabla q, \nabla\hat{p}^\star\right\rangle_{L^2(\Omega)} &= \left\langle \nabla q, \nabla\left(p^\star + \rho\sum_{j=1}^m \alpha_j^m\varphi^{n+1-j}\right)\right\rangle_{L^2(\Omega)} \\ &= \sum_{j=1}^m \beta_j^m l(\boldsymbol{u}^{n+1-j},\mu^{n+1-j},q) + \left\langle q, \rho\sum_{j=1}^m \alpha_j^m\nabla\cdot\boldsymbol{u}^{n+1-j}\right\rangle_{L^2(\Omega)}.\end{aligned} \tag{7.28}$$

The final higher-order scheme is initialised by first computing the initial viscosity from the initial velocity, then the initial pressure through the PPE. The resulting algorithm reads

1. *Initialisation:*
   Use lower-order schemes with increasing order ($\hat{m} = 1,2,\ldots,m$) until having all the quantities required to proceed with the m-th order scheme.

2. *Convection-diffusion steps:*
   For each of the d velocity components, solve the convection-diffusion problem of finding $u_i^{n+1} \in X_h^u$, with $u_i^{n+1}|_{\Gamma_D} = g_i^{n+1}$, such that

$$\begin{aligned}\left\langle \rho w, \boldsymbol{u}^\star\cdot\nabla u_i^{n+1} + \alpha_0^m u_i^{n+1}\right\rangle_\Omega + \left\langle \nabla w, \mu^\star\nabla u_i^{n+1}\right\rangle_{L^2(\Omega)} = \\ \left\langle \frac{\partial w}{\partial x_i}, \hat{p}^\star\right\rangle_{L^2(\Omega)} + \left\langle w, f_i^{n+1} + \rho\sum_{j=1}^m\left(\alpha_j^m u_i^{n+1-j}\right) + (1-\alpha)\frac{\partial\boldsymbol{u}^\star}{\partial x_i}\cdot\nabla\mu^\star\right\rangle_\Omega \\ -\alpha\left\langle \nabla w, (\mu^\star\nabla\boldsymbol{u}^\star)^\top\right\rangle_\Omega + \left\langle w, h_i^{n+1}\right\rangle_{\Gamma_N}\end{aligned} \tag{7.29}$$

   for all $w \in X_h^u$, with $w|_{\Gamma_D} = 0$.

3. *Viscosity projection:*
   Find $\mu^{n+1} \in X_h^\mu$ such that

$$\left\langle \upsilon, \mu^{n+1}\right\rangle_{L^2(\Omega)} = \left\langle \upsilon, \eta\left(\dot{\gamma}\left(\nabla^s\boldsymbol{u}^{n+1}\right)\right)\right\rangle_{L^2(\Omega)} \quad \text{for all } \upsilon \in X_h^\mu. \tag{7.30}$$

4. *Time-step update:*
   If using adaptive stepping, compute Δt^n and update the coefficients α_j^m and β_j^m.

5. *Pressure BC projection (only if $\Gamma_N \neq \emptyset$):*
   Project $\zeta^\star := \sum_{j=1}^m \beta_j^m \left[(1+\alpha)\mu^{n+2-j} \nabla \boldsymbol{u}^{n+2-j} : (\boldsymbol{n}\otimes\boldsymbol{n} - \mathbb{I}) - \boldsymbol{n}\cdot\boldsymbol{h}^{n+2-j} \right]$ such that the resulting quantity $\hat{\zeta}^\star$ is continuous on Γ_N.

6. *Pressure Poisson step*
   Update the modified pressure for the next time step by finding $\hat{p}^\star \in X_h^p$, with $\hat{p}^\star|_{\Gamma_N} = \hat{\zeta}^\star$, such that for all $q \in X_h^p$, with $q|_{\Gamma_N} = 0$, we have

$$\left\langle \nabla q, \nabla \hat{p}^\star \right\rangle_{L^2(\Omega)} = \sum_{j=1}^m \beta_j^m l(\boldsymbol{u}^{n+2-j}, \mu^{n+2-j}, q) + \left\langle q, \rho \sum_{j=1}^m \alpha_j^m \nabla\cdot\boldsymbol{u}^{n+2-j} \right\rangle_{L^2(\Omega)} . \quad (7.31)$$

7.3 Numerical examples

In this section, we assess the accuracy and stability of our non-Newtonian time-splitting framework by tackling simple problems with manufactured solutions and also some classical benchmarks. One of the main advantages of the present approach with respect to conventional split-step methods is the possibility to use finite element pressure-velocity pairs that are not LBB-compatible. We consider first-order simplicial and tensor-product elements, as well as Taylor–Hood elements. The space chosen for the viscosity is the same as the pressure space in each case. We remark that several stability tests with elements and BDFs of first and second order were performed, in two and three dimensions, and our scheme has always been found stable under a standard CFL condition in all cases. This indicates that keeping the grad-grad part of the viscous term on the left-hand side (while treating the remaining part explicitly) is enough to avoid a diffusive step constraint, as in the Newtonian case (see Refs. [71, 72] for details).

Manufactured solutions

Let us start by tackling simple examples with manufactured solutions and a pure Dirichlet boundary, that is, $\Gamma_N = \emptyset$. While in most numerical examples we apply the divergence damping introduced in Subsection 7.2.2, here the term is dropped in order to yield a clearer convergence study. In the unit square $\Omega = (0,1)^2$, we consider solutions of the type

$$p = 2\sin(2-2x_1)f(t),\ \ u_1 = f(t)\sin(2x_2)\sin^2(x_1),\ \ u_2 = -f(t)\sin(2x_1)\sin^2(x_2),$$

under the shear-thinning rheological law $\eta(\dot{\gamma}) = [1+(10\dot{\gamma})^2]^{-1/4}$.

The solution is "ramped up" with different functions $f(t)$, and the resulting Dirichlet datum $\boldsymbol{g}$ and body force $\boldsymbol{f}$ are computed accordingly. First, to measure the spatial accuracy of our method, we choose $f(t) = 1 - e^{-2t}$, so that the solution tends to a steady state as $t \to \infty$. Starting with a coarse mesh containing four identical square elements, several levels of uniform spatial refinement are applied. The spatial approximation errors are computed through the norms

$$\|p - p_h\|_T := \left(\frac{\|p - p_h\|_{L^2(\Omega)}}{\|p\|_{L^2(\Omega)}} \right)\Bigg|_{t=T} \quad \text{and} \quad \|\nabla \boldsymbol{u} - \nabla \boldsymbol{u}_h\|_T = \left(\frac{\|\nabla \boldsymbol{u} - \nabla \boldsymbol{u}_h\|_{L^2(\Omega)}}{\|\nabla \boldsymbol{u}\|_{L^2(\Omega)}} \right)\Bigg|_{t=T}.$$

The final time is selected as $T = 10$, at which $1 - f \approx 2 \times 10^{-9}$. We use the first-order temporal discretisation (BDF1) with a fixed time step $\Delta t = 10^{-2}$. Since this solution has an extremely small time residual at $t = T$, the temporal error should not contaminate the spatial order of accuracy, even when using a large (but still stable) time step and a low-order stepping scheme. The results of the spatial convergence study are shown in Figure 7.1. As expected, the Q_1Q_1 pair yields linear spatial convergence, whereas the Taylor–Hood elements converge quadratically.

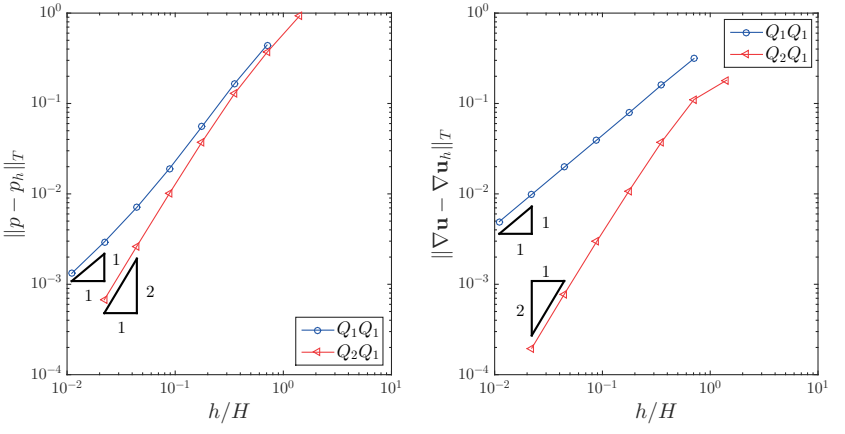

Figure 7.1: Manufactured solution: spatial convergence study.

We also assess the effects of lumping the viscosity projection on the spatial accuracy. The comparison between the standard and lumped versions of the first-order splitting scheme with Q_2Q_1 elements is shown in Figure 7.2. The velocity convergence experiences only a mild degradation at the finest levels, and the pressure is virtually unaffected. This indicates that using a lumped projection can be a simple way to improve efficiency in practice.

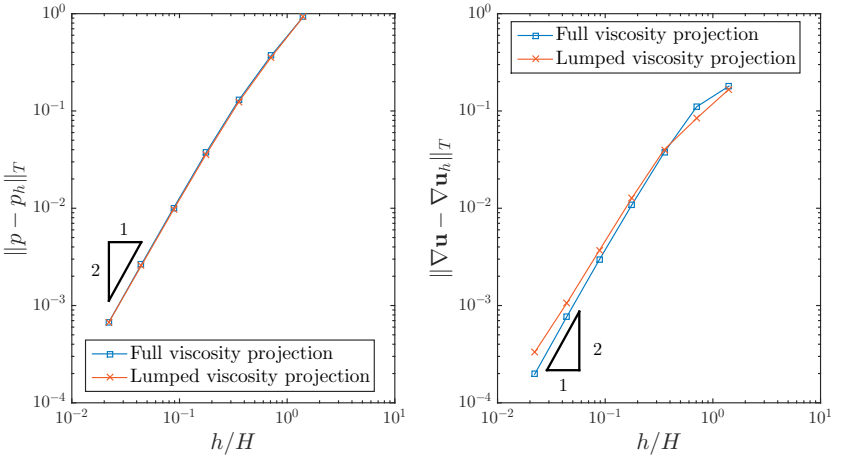

Figure 7.2: Manufactured solution: effect of lumping the viscosity projection.

To assess also the temporal accuracy of the first- and second-order stepping schemes, we now use a periodic function $f(t) = \sin^2(t)$ in the interval $t \in [0,10]$ and consider the maximum error in $\mathrm{Q} := \Omega \times (0,T]$, that is, using the $L^\infty(\mathrm{Q})$ norm. In this case we use the finest spatial mesh considered in the previous study, and refine the time step uniformly by halving it from $\Delta t = 0.16$ all the way down to $\Delta t = 0.00125$. The first-order temporal scheme is combined with the Q_1Q_1 elements, whereas for the second-order stepping scheme (BDF2) we use the Q_2Q_1 elements. The results are shown in Figure 7.3, where the expected orders of convergence are verified. It is worth noting that in these examples the CFL number has ranged from 0.1 to almost 15, which speaks to the good stability properties of the present schemes.

Carreau fluid past a backward-facing step

We now consider the classical backward-facing step setup proposed by Choi and Barakat [129]. They used the Carreau rheological model with the hemodynamic parameters $\rho = 1060$ kg/m^3, $\mu_\infty = 3.5$ mPa·s, $\mu_0 = 250$ mPa·s, $n = 0.25$ and $\lambda = 25$ s. The geometric dimensions (see Figure 7.4) are $L_2 = 2L_1 = 20H$, $s = 0.9423H$ and $H = 5.2$ mm. In order to compare our results to the reference stationary solutions, we use a parabolic inlet profile with flow rate $Q(t)$ ramped up smoothly from zero to $Q_{\max}$ so that $Q(t)/Q_{\max} = \xi(t)$,

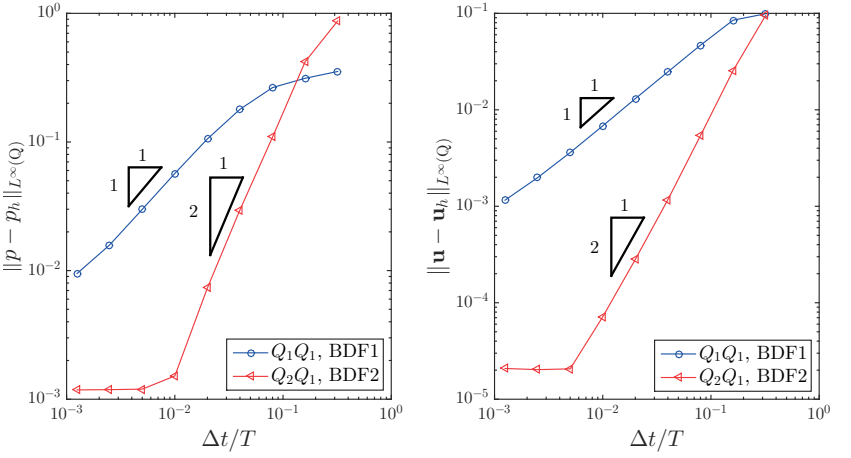

Figure 7.3: Manufactured solution: temporal convergence study.

according to

$$\xi(t) = \begin{cases} \sin^2\left(\frac{\pi t}{2\tau}\right), & \text{for } 0 \le t < \tau, \\ 1, & \text{for } \tau \le t \le T, \end{cases} \tag{7.32}$$

with $\tau = 0.3$ s and $T = 2$ s. On the outlet we set the usual zero pseudo-traction condition $(\mu\nabla\boldsymbol{u} - p\mathbb{I})\boldsymbol{n} = \boldsymbol{0}$. We have employed a first-order method in both space and time, using triangular elements for the spatial discretisation. The mesh is structured, with the element length equal to $H/40$ in the horizontal direction. The elements above and below the step's corner have a vertical length equal to $H/40$ and $s/40$, respectively. This results in a total of 160,000 elements and 81,281 nodes. The time step is set as $\Delta t = 5 \times 10^{-4}$ s for all cases. Choi and Barakat [129] considered several values for the Reynolds number, which they define as $\mathrm{Re} = 2\rho Q_{\max}/\mu_\infty$. The comparison between the reference results and ours for $\mathrm{Re} \in [50{,}300]$ is depicted in Figure 7.5, in terms of the reattachment length r. The comparison shows in general very good agreement. For $\mathrm{Re} = 300$ there is a 5% difference, which might indicate the need for some further refinement close to the re-circulation zone (mind that we are not using any convective stabilisation).

Carreau fluid flow through idealised aneurysm

As a final numerical example inspired by challenging hemodynamic applications, we consider the pulsatile flow of a shear-thinning fluid through a three-dimensional idealised

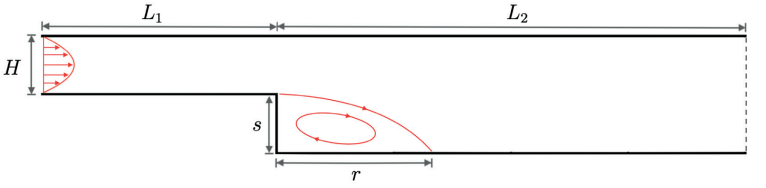

Figure 7.4: Backward-facing step benchmark: problem setup and reattachment length.

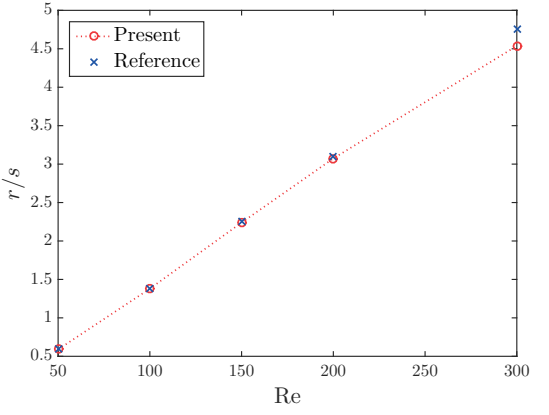

Figure 7.5: Backward-facing step benchmark: reattachment length *vs.* Reynolds number, in comparison to reference results [129].

aneurysm. The fluid parameters are chosen in the physiologically relevant range, considering a Carreau fluid with $\mu_0 = 50$ mPa·s, $\mu_\infty = 5$ mPa·s, $n = 0.25$, $\lambda = 5$ s and $\rho = 1000$ kg/m^3. To generate a suitable mesh, we start from a straight circular cylinder with central axis from $(x_1,x_2,x_3) = (0,0,0)$ to $(0.2,0,0)$, resulting in a length of $L = 0.2$ m between inlet and outlet circular cross-sections of radius $R = 0.01$ m. This simple geometry is easily meshed and afterwards deformed by mapping the radial coordinate r of each nodal point via $\tilde{r} = \left[1+2\sin^{10}(\pi x_1/L)\right] r$. The final mesh consists of around half a million Q_1Q_1 elements with approximately half a million nodes. The second-order stepping is chosen, with $\Delta t = 0.5 \times 10^{-3}$ s. We prescribe an inlet velocity profile given by $u_{in} = [1-(r/R)^2][1-0.3\cos(\pi t/\tau)]\xi(t)$ m/s, with $\xi(t)$ as in (7.32) and $\tau = 0.5$ s. Then, the resulting Reynolds number considering the inlet diameter and mean inlet velocity is 2600. In Figure 7.6 we show the normalised viscosity (*cf.* Eq. (4.18)) at the apex point (A)

located at $(L/2,R,0)$, another apex point (B) at $(L/2,R/\sqrt{2},R/\sqrt{2})$, and the outlet centre point (C). The curves indicate periodicity in time and axisymmetry in space, showing a very intense variation of the viscosity within a pulsation period. Not only the temporal but also the spatial gradients of the viscosity are very large, as seen in Figure 7.7. This behaviour, which one expects to be even more pronounced in smaller vessels with lower Reynolds numbers, highlights the importance of accounting for non-Newtonian rheology. The spatial distribution of μ also reveals axisymmetry and a large recirculation zone. The pressure field depicted in Figure 7.8 shows a steep drop downstream of the aneurysm, caused by the severe radial narrowing.

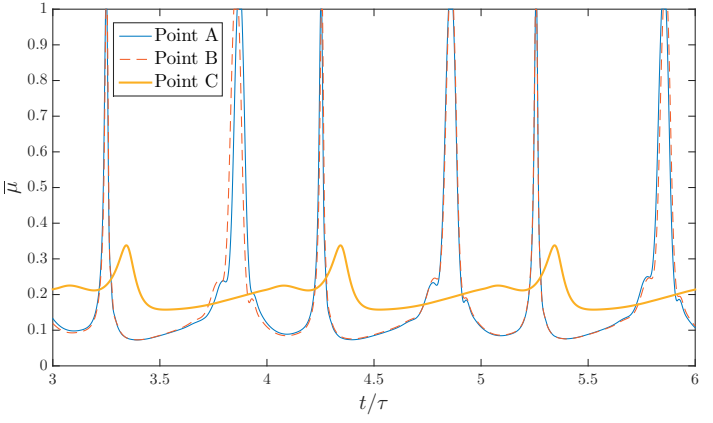

Figure 7.6: Idealised aneurysm flow: normalised viscosity at selected locations. The viscosity at the outlet's centroid (C) varies rather mildly, whereas the two appex points A and B experience a tenfold variation within a pulsation period.

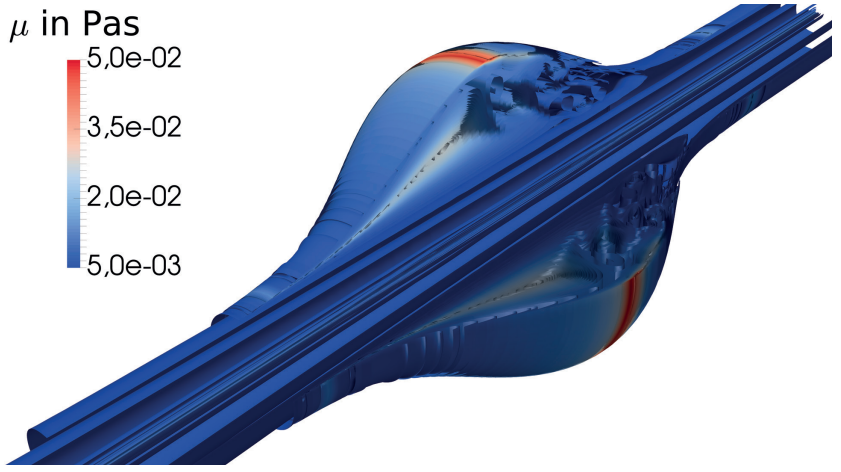

Figure 7.7: Idealised aneurysm flow: selected viscosity contours at $t = 5.83$ s, revealing high gradients and complex flow pattern inside the aneurysm.

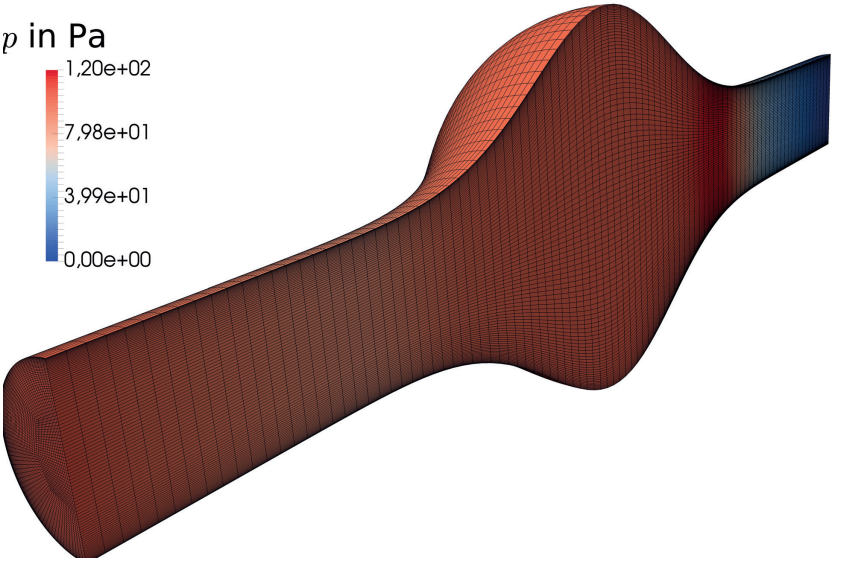

Figure 7.8: Idealised aneurysm flow: pressure field at $t = 5.37$ s, revealing a large, steep decrease right past the aneurysm.

8 STABLE SPACE-TIME FINITE ELEMENT METHODS

In time-dependent flow problems, the time interval and the spatial domain are typically treated in very different manners. The most popular approach is to use finite differences in time and finite elements or volumes for the spatial discretisation, as done in the previous chapter. Despite simple and very efficient in several applications, those methods have an important limitation when it comes to high-performance computing: the temporal discretisation can be adaptive in time but must be uniform in space. This means that a temporal refinement that would perhaps be needed only locally is instead applied to the entire spatial domain, thereby unnecessarily increasing the global number of degrees of freedom. Space-time methods aim to overcome the limitations of such time-stepping schemes by offering a unified approach where time and space are treated in an equal – or at least similar – manner. The vast majority of works dealing with space-time finite element methods for fluid flows employ a discontinuous Galerkin (DG) method in time [37, 130–132] and sometimes also in space [133–135]. This enables sequential solution procedures where the space-time domain is divided in the time direction into slabs: the solution obtained in the first time slab is weakly transmitted onto the second one, and so on. The main shortcomings of DG methods are the increased number of degrees of freedom and the need for face-based data structure and implementation. In this chapter, we consider a continuous finite element discretisation in both space and time.

The original results presented here have been partially published. First numerical results using space-time Taylor–Hood elements are published in Ref. [136], whereas the corresponding FETI method are reported in Ref. [137]. An article on the analysis of the space-time Stokes system in Bochner spaces is currently in preparation [138].

8.1 Variational problem and discretisation

For simplicity of presentation, let us consider the time-dependent model problem with zero initial and boundary conditions:

$$\rho[\partial_t \boldsymbol{u} + (\nabla \boldsymbol{u})\boldsymbol{u}] - \nabla \cdot (2\mu \nabla^s \boldsymbol{u}) + \nabla p = \boldsymbol{f} \quad \text{in } \mathrm{Q}, \tag{8.1}$$

$$\nabla \cdot \boldsymbol{u} = 0 \quad \text{in } \mathrm{Q}, \tag{8.2}$$

$$\boldsymbol{u} = \boldsymbol{0} \quad \text{on } \Sigma, \tag{8.3}$$

$$\boldsymbol{u} = \boldsymbol{0} \quad \text{at } t = 0, \tag{8.4}$$

with the pressure scaling

$$\int_\Omega p \, \mathrm{d}\Omega = 0 \;\; \text{for all} \;\; t \,, \tag{8.5}$$

where $\mathrm{Q} := \Omega \times (0,T)$ is the space-time cylinder and $\Sigma := \partial\Omega \times (0,T)$. Of course, if the spatial domain Ω varies in time, then Q will in general be a non-tensor-product domain in $\mathbb{R}^{d+1}$, which can be handled very naturally by space-time methods [134, 139]. Equation (8.5) presents one of many possible scaling conditions to uniquely define the pressure; such conditions are only necessary in the pure Dirichlet problem.

Remark 8.1. *As done so far, we use the symbol ∇ to denote spatial differentiation. Alternative notations such as ∇_x are sometimes found in the space-time literature [140].*

The space-time variational formulation in Bochner spaces reads: given $\boldsymbol{f} \in Z'$, find $(\boldsymbol{u},p) \in X \times Y$ such that for all $(\boldsymbol{w},q) \in Z \times Y$ we have

$$\int_\mathrm{Q} \rho \boldsymbol{w} \cdot [\partial_t \boldsymbol{u} + (\nabla \boldsymbol{u})\boldsymbol{u}] \, \mathrm{dQ} + \int_\mathrm{Q} 2\mu \nabla^s \boldsymbol{u} : \nabla^s \boldsymbol{w} \, \mathrm{dQ} - \int_\mathrm{Q} (\nabla \cdot \boldsymbol{w}) \, p \, \mathrm{dQ} = \int_\mathrm{Q} \boldsymbol{w} \cdot \boldsymbol{f} \, \mathrm{dQ}, \tag{8.6}$$

$$\int_\mathrm{Q} q \nabla \cdot \boldsymbol{u} \, \mathrm{dQ} + \int_0^T \left(\int_\Omega q \, \mathrm{d}\Omega \int_\Omega p \, \mathrm{d}\Omega \right) \mathrm{d}t = 0 \,, \tag{8.7}$$

with the second term in Eq. (8.7) enforcing the pressure scaling (8.5). Since no time derivative is applied to the velocity test function $\boldsymbol{w}$, we get a Petrov–Galerkin formulation with $Y = L^2(\mathrm{Q})$, $Z := \left[L^2\left(0,T; H_0^1(\Omega)\right) \right]^d$, $Z' = \left[L^2\left(0,T; H^{-1}(\Omega)\right) \right]^d$ and

$$X := \{ \boldsymbol{u} \in Z \;:\; [\partial_t \boldsymbol{u} + (\nabla \boldsymbol{u})\boldsymbol{u}] \in Z' \;\; \text{and} \;\; \boldsymbol{u}|_{t=0} = \boldsymbol{0} \} \,. \tag{8.8}$$

Although the continuous problem is posed as a Petrov–Galerkin formulation, in the discrete case we will employ a mixed Bubnov–Galerkin method, i.e., the same finite element spaces will be used for test and trial (*Ansatz*) functions. It is worth noting that, when $\mu = \mu(\nabla^s \boldsymbol{u})$, the velocity trial space as defined in Eq. (8.8) might not be regular enough.

In most – if not all – of the literature on space-time finite element methods for flow problems, stabilised rather than LBB-stable formulations are considered. The main reason for that is perhaps the simplicity and reduced computational cost offered by first-order finite element discretisations. As in the stationary case, the most common stabilisation techniques employed in space-time applications are VMS, PSPG and GLS methods [37, 132, 141]. Of course, the stabilisation methods presented in Chapter 6 are also applicable to the space-time problem. Nevertheless, this chapter focus on LBB-stable elements and, in fact, we introduce space-time Taylor–Hood elements: globally continuous second- and first-order

(in both space and time) spaces for velocity and pressure, respectively. Figure 8.1 illustrates a prismatic Taylor–Hood element in two spatial dimensions. Notice that the velocity nodes are formed by a "quadratic extrusion" in time. For $d = 3$ the elements are constructed analogously: for instance, by appropriately extruding (spatial) tetrahedral Taylor–Hood elements in time. Alternatively, more flexibility in the space-time discretisation can be attained via simplicial Taylor–Hood elements (tetrahedra for $d = 2$ or pentatopes for $d = 3$). Such elements are more appropriate for unstructured mesh generation and adaptivity [38, 39, 134, 139], although adaptive methods are not our current focus. As we shall demonstrate through various numerical examples, these space-time Taylor–Hood elements are not only stable but also optimally convergent.

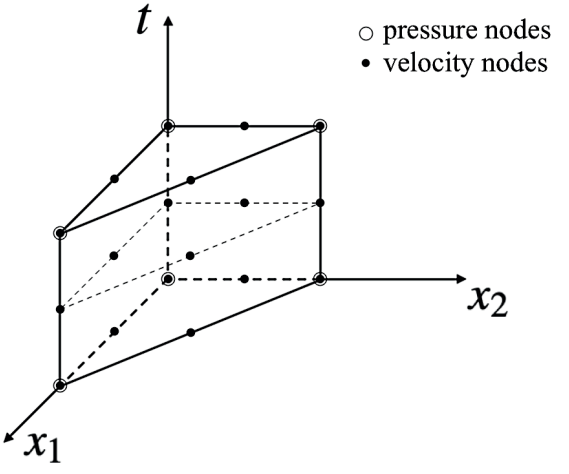

Figure 8.1: Prismatic space-time Taylor–Hood element for $d = 2$.

8.2 Space-time finite element tearing and interconnecting methods

When solving large-scale problems, modern high-performance computing relies heavily on parallelisation and often on domain decomposition methods (DDMs). This is especially important in the space-time setting, since abandoning the standard structure of time slabs/steps leads to very large algebraic systems to be solved at once. Therefore, decomposing the space-time domain into smaller subdomains that can be handled efficiently is key to making space-time methods competitive. Although the use of DDM is very well-established in computational engineering in general, in space-time methods they have only

recently started to gain momentum [142–147]. In this context, we present an approach that is, to the best of our knowledge, the first finite element tearing and interconnecting (FETI) method for space-time problems – in fact, for parabolic problems in general.

8.2.1 Basic setup

FETI methods were originally introduced by Farhat and Roux [148] for elliptic problems, the most popular of which being solid elasticity. The goal is to create smaller subproblems that can be efficiently solved in parallel. Let us consider a decomposition of the space-time cylinder Q into s non-overlapping subdomains Q_i, $i = 1,...,s$. The idea behind FETI methods is to *tear* the global problem into local problems in the subdomains, and then *interconnect* them all back using discrete Lagrange multipliers $\underline{\lambda}$. Although the multipliers can be given physical interpretations in different problems [149], the method is algebraically motivated and can be derived from a discrete skeleton formulation [150]. For simplicity, we take here the Stokes system as our model problem. On the discrete level, the algebraic system has the form

$$\underbrace{\begin{bmatrix} \mathbf{A} & -\mathbf{C}^\top \\ \mathbf{C} & \mathbf{D} \end{bmatrix}}_{\mathbf{K}} \underbrace{\begin{pmatrix} \underline{\boldsymbol{u}} \\ \underline{p} \end{pmatrix}}_{\underline{\boldsymbol{q}}} = \underbrace{\begin{pmatrix} \underline{\boldsymbol{f}}^u \\ \underline{\mathrm{f}}^p \end{pmatrix}}_{\underline{\boldsymbol{f}}}, \tag{8.9}$$

or, more compactly, $\mathbf{K}\underline{\boldsymbol{q}} = \underline{\boldsymbol{f}}$. When using continuous pressure elements, two options are possible in the FETI approach. The first is to use a set of Lagrange multipliers $\underline{\lambda}^u$ for the velocity interface degrees of freedom and another set $\underline{\lambda}^p$ for the pressure ones. The other possibility is to take advantage of the fact that the mixed variational formulation allows $p \in L^2(\mathrm{Q})$ and relax the (interface) continuity of the pressure [151]. Both approaches will be considered and compared herein. Let us assume, for clarity of presentation, a decomposition of Q into two subdomains Q_1 and Q_2. In this case, the discrete FETI system for fully continuous pressure has the form

$$\begin{bmatrix} \mathbf{A}_1 & -\mathbf{C}_1^\top & \mathbf{0} & \mathbf{0} & \mathbf{B}_1^{u\top} & \mathbf{0} \\ \mathbf{C}_1 & \mathbf{D}_1 & \mathbf{0} & \mathbf{0} & \mathbf{0} & \mathbf{B}_1^{p\top} \\ \mathbf{0} & \mathbf{0} & \mathbf{A}_2 & -\mathbf{C}_2^\top & \mathbf{B}_2^{u\top} & \mathbf{0} \\ \mathbf{0} & \mathbf{0} & \mathbf{C}_2 & \mathbf{D}_2 & \mathbf{0} & \mathbf{B}_2^{p\top} \\ \mathbf{B}_1^u & \mathbf{0} & \mathbf{B}_2^u & \mathbf{0} & \mathbf{0} & \mathbf{0} \\ \mathbf{0} & \mathbf{B}_1^p & \mathbf{0} & \mathbf{B}_2^p & \mathbf{0} & \mathbf{0} \end{bmatrix} \begin{pmatrix} \underline{\boldsymbol{u}}_1 \\ \underline{p}_1 \\ \underline{\boldsymbol{u}}_2 \\ \underline{p}_2 \\ \underline{\lambda}^u \\ \underline{\lambda}^p \end{pmatrix} = \begin{pmatrix} \underline{\boldsymbol{f}}_1^u \\ \underline{\mathrm{f}}_1^p \\ \underline{\boldsymbol{f}}_2^u \\ \underline{\mathrm{f}}_2^p \\ \underline{\mathbf{0}} \\ \underline{0} \end{pmatrix},$$

where subscript i indicates matrices and vectors arising from the Stokes system restricted to subdomain Q_i, and $\mathbf{B}_i^u$ and $\mathbf{B}_i^p$ are boolean matrices interconnecting the velocity and pressure fields, respectively. Then, grouping pressure and velocity into a vector $\underline{\boldsymbol{q}}$ and considering again the general setting with s subdomains, the system can be written compactly

as

$$\begin{bmatrix} \mathbf{K}_1 & \mathbf{0} & \dots & \mathbf{0} & \mathbf{B}_1^\top \\ \mathbf{0} & \mathbf{K}_2 & \dots & \mathbf{0} & \mathbf{B}_2^\top \\ \vdots & \vdots & \ddots & \vdots & \vdots \\ \mathbf{0} & \mathbf{0} & \dots & \mathbf{K}_s & \mathbf{B}_s^\top \\ \mathbf{B}_1 & \mathbf{B}_2 & \dots & \mathbf{B}_s & \mathbf{0} \end{bmatrix} \begin{pmatrix} \underline{\boldsymbol{q}}_1 \\ \underline{\boldsymbol{q}}_2 \\ \vdots \\ \underline{\boldsymbol{q}}_s \\ \underline{\lambda} \end{pmatrix} = \begin{pmatrix} \underline{\boldsymbol{f}}_1 \\ \underline{\boldsymbol{f}}_2 \\ \vdots \\ \underline{\boldsymbol{f}}_s \\ \underline{\mathbf{0}} \end{pmatrix}, \tag{8.10}$$

in which

$$\mathbf{B}_i := \begin{bmatrix} \mathbf{B}_i^u & \mathbf{0} \\ \mathbf{0} & \mathbf{B}_i^p \end{bmatrix}, \quad \underline{\lambda} := \begin{pmatrix} \underline{\lambda}^u \\ \underline{\lambda}^p \end{pmatrix}, \tag{8.11}$$

and similarly for the other matrices and vectors. If the interface continuity of the pressure is to be relaxed, we simply take $\mathbf{B}_i = \begin{bmatrix} \mathbf{B}_i^u & \mathbf{0} \end{bmatrix}$ and $\underline{\lambda} = \underline{\lambda}^u$. Unless where otherwise stated, in the numerical examples we consider fully continuous pressure.

8.2.2 Global problem and floating subdomains

If we assume that $\overline{\mathrm{Q}_i} \cap \Sigma \neq \emptyset$ for all i, so that all local stiffness matrices $\mathbf{K}_i \in \mathbb{R}^{n_i \times n_i}$ are invertible, then the local problems can be written as

$$\mathbf{K}_i \underline{\boldsymbol{q}}_i = \underline{\boldsymbol{f}}_i - \mathbf{B}_i^\top \underline{\lambda}, \ i = 1,\dots,s, \tag{8.12}$$

and the local degrees of freedom $\underline{\boldsymbol{q}}_i$ are "glued" back together by enforcing

$$\sum_{i=1}^{s} \mathbf{B}_i \underline{\boldsymbol{q}}_i = \underline{\mathbf{0}}. \tag{8.13}$$

This results in a saddle point problem usually handled via the Schur complement approach, in which the Lagrange multipliers are found by solving the global problem

$$\left(\sum_{i=1}^{s} \mathbf{B}_i \mathbf{K}_i^{-1} \mathbf{B}_i^\top \right) \underline{\lambda} = \sum_{i=1}^{s} \mathbf{B}_i \mathbf{K}_i^{-1} \underline{\boldsymbol{f}}_i. \tag{8.14}$$

Once $\underline{\lambda}$ has been found, the local problems (8.12) are effectively decoupled and can be solved independently. Differently from standard elliptic FETI applications, our problem is *not* symmetric, therefore conjugate gradient methods cannot be applied to solve Eq. (8.14). Our method of choice is the generalized minimal residual method (GMRES) [152], as done for instance by Toselli [153] and Kučera et al. [154].

When a certain subdomain Q_i does not intersect $\partial\mathrm{Q}$, or only intersects the "lid" of the space-time domain ($t = T$), the local stiffness matrix $\mathbf{K}_i$ will be singular. In that case, we write the solution of the local problem as

$$\underline{\boldsymbol{q}}_i = \mathbf{K}_i^+ \left(\underline{\boldsymbol{f}}_i - \mathbf{B}_i^\top \underline{\lambda} \right) + \mathbf{R}_i \underline{\alpha}_i, \tag{8.15}$$

where $\mathbf{K}_i^+$ is a generalised inverse (or pseudo-inverse) of $\mathbf{K}_i$, $\underline{\alpha}_i \in \mathbb{R}^{k_i}$ is a vector of (unknown) linear coefficients, $k_i = \dim[\mathcal{N}(\mathbf{K}_i)]$ and $\mathbf{R}_i \in \mathbb{R}^{n_i \times k_i}$ is a matrix whose columns form a basis of $\mathcal{N}(\mathbf{K}_i)$, which is the null-space (or kernel) of $\mathbf{K}_i$.

We shall turn our attention to the solution of Eq. (8.15) soon, but what it already tells us is that the space $\mathcal{N}(\mathbf{K}_i)$ is a necessary component for the solver. Fortunately, for the Stokes system, this information can be retrieved from the continuous case. Differently from the strong Stokes operator, the weak variational operator has a finite-dimensional kernel, namely, the space of constant (in space and time) velocities and null pressures (see Remark 8.2). Although the terms "rigid-body modes" and "floating subdomains" have a structural mechanics background, they are often employed in the FETI literature in a more general sense [150]. We shall henceforth say that Q_i is a *floating subdomain* if $\mathbf{K}_i$ is singular, and denote by *rigid-body modes* of $\mathbf{K}_i$ its eigenvectors associated with null eigenvalues.

Remark 8.2. *If the Laplace form of the Stokes operator is replaced by the elasticity (stress-divergence) form, then the kernel will additionally contain $2d-3$ rigid rotation modes [155, 156]. Another disadvantage of using the elasticity form is the dependence of $\mathcal{N}(\mathbf{K}_i)$ upon the number of nodes in $\overline{Q_i} \cap \Sigma$ [157].*

Since we know the kernel of the continuous operators, matrices $\mathbf{R}_i$ can be straightforwardly constructed. Now, denoting the range (or image) of $\mathbf{K}_i$ by $\mathcal{R}(\mathbf{K}_i)$, it is known that system (8.15) is solvable if, and only if [158]

$$\underline{f}_i - \mathbf{B}_i^\top \underline{\lambda} \in \mathcal{R}(\mathbf{K}_i)\,. \tag{8.16}$$

Since the fundamental theorem of linear algebra gives [159]

$$\mathbb{R}^{n_i} = \mathcal{R}(\mathbf{K}_i) \oplus \mathcal{N}(\mathbf{K}_i^\top)\,,$$

we can rewrite the solvability condition (8.16) as

$$\tilde{\mathbf{R}}_i^\top \left(\underline{f}_i - \mathbf{B}_i^\top \underline{\lambda}\right) = (\underbrace{0, \ldots, 0}_{k_i \text{ times}})^\top, \tag{8.17}$$

where $\tilde{\mathbf{R}}_i \in \mathbb{R}^{n_i \times k_i}$ is such that its columns form a basis of $\mathcal{N}(\mathbf{K}_i^\top)$. Here we must be careful so as not to try and apply standard procedures devised for the usual (symmetric) FETI setting. In such cases, one simply takes $\tilde{\mathbf{R}}_i = \mathbf{R}_i$, that is, the same basis is used for Eqs. (8.15) and (8.17). Yet, since the problem under consideration here is not symmetric, different solution procedures must be employed, as discussed later on. Note that condition (8.17) gives us k_i linearly independent equations that compensate for the k_i additional unknown coefficients in $\underline{\alpha}_i$.

Substituting the local problems (8.15) into the interconnecting condition (8.13) leads to

$$\mathbf{S}\underline{\lambda} - \mathbf{G}\underline{\alpha} = \underline{d}\,, \tag{8.18}$$

in which $\mathbf{S} = \sum_{i=1}^{s} \mathbf{B}_i \mathbf{K}_i^{+} \mathbf{B}_i^{\top}$, $\underline{d} = \sum_{i=1}^{s} \mathbf{B}_i \mathbf{K}_i^{+} \underline{\boldsymbol{f}}_i$,

$$\mathbf{G} = \begin{bmatrix} \mathbf{B}_1 \mathbf{R}_1 & \dots & \mathbf{B}_s \mathbf{R}_s \end{bmatrix} \text{ and } \underline{\alpha} = \begin{pmatrix} \underline{\alpha}_1 \\ \vdots \\ \underline{\alpha}_s \end{pmatrix}.$$

Similarly, the compatibility condition (8.17) can be reformulated as

$$\tilde{\mathbf{G}}^{\top} \underline{\lambda} = \underline{e}, \tag{8.19}$$

where

$$\tilde{\mathbf{G}} = \begin{bmatrix} \mathbf{B}_1 \tilde{\mathbf{R}}_1 & \dots & \mathbf{B}_s \tilde{\mathbf{R}}_s \end{bmatrix} \text{ and } \underline{e} = \begin{pmatrix} \tilde{\mathbf{R}}_1^{\top} \underline{\boldsymbol{f}}_1 \\ \vdots \\ \tilde{\mathbf{R}}_s^{\top} \underline{\boldsymbol{f}}_s \end{pmatrix}.$$

Of course, when a certain subdomain Ω_j is not floating, then $\mathbf{K}_j^{+} = \mathbf{K}_j^{-1}$ and there is no $\underline{\alpha}_j$ to be found, that is, Ω_j will not contribute to either $\mathbf{G}$, $\tilde{\mathbf{G}}$ or $\underline{\alpha}$. Alternatively, when using the so-called *all-floating* approach, Dirichlet and initial conditions are also enforced via Lagrange multipliers and all local problems are singular [160, 161].

The global problem can finally by stated as

$$\begin{bmatrix} \mathbf{S} & -\mathbf{G} \\ \tilde{\mathbf{G}}^{\top} & \mathbf{0} \end{bmatrix} \begin{pmatrix} \underline{\lambda} \\ \underline{\alpha} \end{pmatrix} = \begin{pmatrix} \underline{d} \\ \underline{e} \end{pmatrix}. \tag{8.20}$$

Since $\tilde{\mathbf{G}} \neq \mathbf{G}$ due to the asymmetry of the space-time variational formulation, standard techniques normally used in the context of symmetric FETI methods cannot be applied straightforwardly. We will therefore introduce a suitable procedure for the present case.

Generalised inverse

In order to assemble the global problem, we need to compute the generalised inverses $\mathbf{K}_i^{+}$ and the bases for $\mathcal{N}(\mathbf{K}_i)$ and $\mathcal{N}(\mathbf{K}_i^{\top})$. As previously discussed, for most common problems we can construct matrices $\mathbf{R}_i$ trivially since the rigid-body modes are known *a priori*. On the other hand, $\tilde{\mathbf{R}}_i$ must be computed numerically since the kernel of $\mathbf{K}_i^{\top}$ is generally discretisation-dependent – but that does not necessarily incur computational overhead. For instance, when using a singular value decomposition (SVD) algorithm to find $\mathbf{K}_i^{+}$, we get an orthonormal basis for $\mathcal{N}(\mathbf{K}_i^{\top})$ as a subproduct. Let us consider the classical SVD of a matrix $\mathbf{K}_i \in \mathbb{R}^{n \times n}$ with rank r:

$$\mathbf{K}_i = \mathbf{U}\mathbf{W}\mathbf{V}^{\top},$$

where $\mathbf{U}$ and $\mathbf{V}$ are orthogonal matrices and $\mathbf{W}$ is a diagonal matrix containing the singular values of $\mathbf{K}_i$ in descending magnitude order (see Ref. [162] for details). A pseudo-inverse of $\mathbf{K}_i$ is given by $\mathbf{K}_i^+ = \mathbf{V}\tilde{\mathbf{W}}\mathbf{U}^\top$, in which $\tilde{\mathbf{W}}$ is a diagonal matrix whose entries are

$$\tilde{W}_{kk} = \begin{cases} 1/W_{kk}, & \text{if } 1 \leq k \leq r, \\ 0, & \text{otherwise,} \end{cases}$$

and $\tilde{\mathbf{R}}_i$ can be constructed simply with the last $n - r$ columns of $\mathbf{U}$. Yet, performing a full SVD may be prohibitive in practical situations when the local problems are large. For such cases, an efficient technique for computing both the pseudo-inverse and the kernel of a matrix with known nullity was proposed by Farhat and Géradin [157], combining LU and singular value decompositions. This is possible in the present case, since the nullity of $\mathbf{K}_i^\top$ is known ($\dim[\mathcal{N}(\mathbf{K}_i^\top)] = \dim[\mathcal{N}(\mathbf{K}_i)] = k_i$). Thus, applying the method to matrix $\mathbf{K}_i^\top$ will give us $(\mathbf{K}_i^+)^\top$ and $\tilde{\mathbf{R}}_i$ at once.

Solving the global problem

With all ingredients at hand for assembling the global problem (8.20), we turn our attention to its solution, which will be performed using a projected GMRES approach. In order to decouple the Lagrange multipliers $\underline{\lambda}$ from the rigid-body coefficients $\underline{\alpha}$, we introduce a projection operator $\mathbf{P} : \mathbb{R}^m \to \mathcal{N}(\tilde{\mathbf{G}}^\top)$ constructed as

$$P := \mathbf{I} - \mathbf{G}(\tilde{\mathbf{G}}^\top \mathbf{G})^{-1}\tilde{\mathbf{G}}^\top, \tag{8.21}$$

where m is the dimension of $\underline{\lambda}$ and $\mathbf{I}$ is the $m \times m$ identity matrix. Notice that $\tilde{\mathbf{G}}^\top\mathbf{G}$ is a small matrix and can be inverted directly. Applying $\mathbf{P}$ to Eq. (8.18) leads to the projected equation

$$(\mathbf{PS})\underline{\lambda} = \mathbf{P}\underline{d}, \tag{8.22}$$

which must be solved under the constraint $\tilde{\mathbf{G}}^\top\underline{\lambda} = \underline{e}$. To do that, we use a similar approach to that employed by Toselli [153], homogenising Eq. (8.22) through the splitting

$$\underline{\lambda} = \underline{\lambda}_0 + \tilde{\underline{\lambda}}, \tag{8.23}$$

with $\tilde{\underline{\lambda}} \in \mathcal{N}(\tilde{\mathbf{G}}^\top)$ and $\tilde{\mathbf{G}}^\top\underline{\lambda}_0 = \underline{e}$. It is easy to verify that the choice $\underline{\lambda}_0 := \mathbf{G}(\tilde{\mathbf{G}}^\top\mathbf{G})^{-1}\underline{e}$ fullfils the requirement. Thus, we are left with the problem to find $\tilde{\underline{\lambda}} \in \mathcal{N}(\tilde{\mathbf{G}}^\top)$ such that

$$(\mathbf{PS})\tilde{\underline{\lambda}} = \mathbf{P}\left(\underline{d} - \mathbf{S}\underline{\lambda}_0\right). \tag{8.24}$$

As long as we start the GMRES algorithm with a vector in $\mathcal{N}(\tilde{\mathbf{G}}^\top)$ (e.g., the null vector), the subsequent iterates will also meet the constraint, up to round-off error [150, 154]. We refer the reader to the works of Kučera et al. [154, 163] for excellent discussions on both theoretical and algorithmic aspects of projected Krylov methods for asymmetric systems. Once we have found $\tilde{\underline{\lambda}}$ and rebuilt $\underline{\lambda}$, it remains to find $\underline{\alpha}$. This can be done by premultiplying Eq. (8.18) by $(\tilde{\mathbf{G}}^\top\mathbf{G})^{-1}\tilde{\mathbf{G}}^\top$, which leads to

$$\underline{\alpha} = (\tilde{\mathbf{G}}^\top\mathbf{G})^{-1}\tilde{\mathbf{G}}^\top\left(\mathbf{S}\underline{\lambda} - \underline{d}\right). \tag{8.25}$$

8.3 Numerical examples

We now present various numerical examples to showcase the accuracy of our stable space-time elements, as well as the performance of the present FETI-based solver. In the Newtonian examples, we consider the non-dimensionalised version of the Navier–Stokes problem:

$$\int_{\mathrm{Q}} \left\{ \boldsymbol{w}_h \cdot [\partial_t \boldsymbol{u}_h + (\nabla \boldsymbol{u}_h)\,\boldsymbol{u}_h] + \frac{1}{\mathrm{Re}} \nabla \boldsymbol{w}_h : \nabla \boldsymbol{u}_h + (\nabla \cdot \boldsymbol{w}_h)\, p_h \right\} \mathrm{dQ} = \int_{\mathrm{Q}} \boldsymbol{w}_h \cdot \boldsymbol{f} \ \mathrm{dQ}, \tag{8.26}$$

$$\int_{\mathrm{Q}} q_h \nabla \cdot \boldsymbol{u}_h \ \mathrm{dQ} + \int_{s_0} q_h p_h \ \mathrm{d}t = 0, \tag{8.27}$$

with $s_0 := \left\{ (\boldsymbol{x},t) \in \mathbb{R}^{d+1} \ : \ \boldsymbol{x} = \boldsymbol{0} \right\}$. The line integral in Eq. (8.27) enforces the pressure scaling $p(\boldsymbol{0},t) \equiv 0$. This is possible when we employ a finite element discretisation in which $(q_h p_h)|_{\boldsymbol{x}=\boldsymbol{0}}$ is well-defined, which is not necessarily the case when $p \in L^2(\mathrm{Q})$. The advantage of this pressure scaling is that it produces a highly sparse matrix, whereas the somewhat more standard scaling in Eq. (8.7) leads to a dense one.

8.3.1 Convergence study

Manufactured Stokes flow solution in two spatial dimensions

We first consider the linear Stokes problem in the unit cube $\mathrm{Q} = (0,1)^3$ with $\mathrm{Re} = 1$, homogeneous initial and (Dirichlet) boundary conditions and body force $\boldsymbol{f} = \boldsymbol{f}_p + \boldsymbol{f}_t + \boldsymbol{f}_x$:

$$\boldsymbol{f}_p = \begin{pmatrix} t^2 \left(x_2 t e^{-x_1 x_2 t} + 1 \right) \\ t^3 x_1 e^{-x_1 x_2 t} \end{pmatrix},$$

$$\boldsymbol{f}_t = \begin{pmatrix} e^{-t} \left(4{x_2}^3 - 6{x_2}^2 + 2x_2 \right) [x_1 (x_1 - 1)]^2 \\ -e^{-t} \left(4{x_1}^3 - 6{x_1}^2 + 2x_1 \right) [x_2 (x_2 - 1)]^2 \end{pmatrix},$$

$$\boldsymbol{f}_x = \begin{pmatrix} (1 - e^{-t})\,(4 - 8x_2) \left(3{x_1}^4 - 6{x_1}^3 - 6(x_1 x_2)^2 + 3{x_1}^2 - 6x_1 {x_2}^2 + 6x_1 x_2 + {x_2}^2 - x_2 \right) \\ (e^{-t} - 1)\,(4 - 8x_1) \left(3{x_2}^4 - 6{x_2}^3 - 6(x_1 x_2)^2 + 3{x_2}^2 - 6x_2 {x_1}^2 + 6x_1 x_2 + {x_1}^2 - x_1 \right) \end{pmatrix}.$$

The corresponding analytical solution is

$$p = \left(1 + x_1 - e^{-x_1 x_2 t} \right) t^2, \ \ \boldsymbol{u} = \begin{pmatrix} (1 - e^{-t}) \left(4{x_2}^3 - 6{x_2}^2 + 2x_2 \right) [x_1 (x_1 - 1)]^2 \\ (e^{-t} - 1) \left(4{x_1}^3 - 6{x_1}^2 + 2x_1 \right) [x_2 (x_2 - 1)]^2 \end{pmatrix}.$$

For the discretisation we use tetrahedral Taylor–Hood elements, starting with the coarse mesh shown in Figure 8.2 (top) and performing four levels of uniform refinement. The

fifth and finest mesh, depicted in Figure 8.2 (bottom), has approximately 4×10^5 elements and 1.2×10^6 degrees of freedom. As we can see in Table 8.1, the convergence study reveals very interesting results. While the pressure and the spatial velocity gradient convergence quadratically, as in stationary cases, the temporal derivative of the velocity converges linearly. Although *a priori* error estimates are – to the best of our knowledge and at the moment of writing – still an open problem, we can conjecture that the different convergence rates of the spatial and temporal gradients are due to the different regularity requirements in space and time (see (8.8)). Error estimates in $H^{1,0}(\Omega) := L^2(0,T;H^1(\Omega))$ for the heat equation, which is closely related to the Stokes system, have been proven by Steinbach [140] and are in agreement with our current numerical results. Following the same analysis, we can assert that a CFL-like condition is not to be expected here, at least when considering the linear Stokes problem. On the other hand, using similar space-time finite elements for hyperbolic problems such as the wave equation *does* incur a CFL condition [164]. Note that the observed convergence rates can be seen as optimal not only from a theoretical point of view, but also from a practical standpoint. Firstly because all the terms present in the strong residual of the momentum equation, namely $\partial_t \boldsymbol{u}_h$, $\Delta \boldsymbol{u}_h$ and ∇p_h, shall converge with the same order. Secondly, p_h and $\nabla \boldsymbol{u}_h$ converging quadratically leads to quadratic convergence of the Cauchy stress tensor, which is of critical importance in FSI and hemodynamic applications.

Table 8.1: Stokes problem in two spatial dimensions: mesh convergence study.

Mesh	$\|\nabla \boldsymbol{u} - \nabla \boldsymbol{u}_h\|_0$	eoc	$\|\partial_t \boldsymbol{u} - \partial_t \boldsymbol{u}_h\|_0$	eoc	$\|p - p_h\|_0$	eoc
1	5.93e-1	–	2.21e-0	–	2.37e-1	–
2	1.82e-1	1.70	8.15e-1	1.43	6.36e-2	1.90
3	4.85e-2	1.90	3.32e-1	1.29	1.61e-2	1.98
4	1.23e-2	1.97	1.55e-1	1.10	3.99e-3	2.01
5	3.10e-3	1.99	7.78e-2	1.00	9.77e-4	2.03

Two-dimensional Taylor–Green vortex

Taylor–Green vortices in two spatial dimensions are among very few analytical time-dependent solutions of the Navier–Stokes system with zero body force. In a normalised space-time domain $Q = (0,1)^3$, the dimensionless solution represents a decaying system of vortices described by

$$p = -\frac{f^2(t)}{2}\left(\sin^2 2\pi x_1 + \sin^2 2\pi x_2\right), \quad \boldsymbol{u} = \begin{pmatrix} f(t)\sin\pi x_1 \cos\pi x_2 \\ -f(t)\sin\pi x_2 \cos\pi x_1 \end{pmatrix}, \quad \text{with} \quad f(t) = e^{-2\pi^2 t/\mathrm{Re}}.$$

While this problem is typically simulated considering periodic BCs, for simplicity we assume a standard Dirichlet setting, computing the boundary and initial data from the

known analytical solution. This time we use prismatic elements for the uniform refinement study, the coarsest and finest meshes being depicted in Figure 8.3. The results for Re = 100, shown in Table 8.2, are similar to the ones obtained for the Stokes problem. The quadratic convergence observed for the temporal velocity gradient is probably only an initial higher-order convergence which should eventually turn linear again. When setting Re = 2000 to simulate a more convective flow regime, the results in Table 8.3 show that the quadratic rates are not reached within the refinement levels considered. This is somewhat expected, since we are not using any kind of convective stabilisation such as SUPG or VMS. Therefore, once the element Reynolds numbers are low enough and the flow is sufficiently resolved, the quadratic convergence should be attained.

Table 8.2: Taylor–Green vortex: convergence study for Re = 100.

Mesh	$\|\nabla \boldsymbol{u} - \nabla \boldsymbol{u}_h\|_0$	eoc	$\|\partial_t \boldsymbol{u} - \partial_t \boldsymbol{u}_h\|_0$	eoc	$\|p - p_h\|_0$	eoc
1	3.06e-1	–	6.05e-1	–	9.45e-2	–
2	2.72e-1	0.17	5.65e-1	0.10	7.10e-2	0.41
3	7.83e-2	1.80	1.17e-1	2.26	2.48e-2	1.52
4	2.16e-2	1.86	2.46e-2	2.25	6.87e-3	1.85
5	5.63e-3	1.94	5.67e-3	2.12	1.77e-3	1.95

Table 8.3: Taylor–Green vortex: convergence study for Re = 2000.

Mesh	$\|\nabla \boldsymbol{u} - \nabla \boldsymbol{u}_h\|_0$	eoc	$\|\partial_t \boldsymbol{u} - \partial_t \boldsymbol{u}_h\|_0$	eoc	$\|p - p_h\|_0$	eoc
1	6.31e-1	–	22.6	–	7.75e-2	–
2	9.59e-1	-0.6	33.1	-0.5	9.30e-2	-0.2
3	2.83e-1	1.76	8.04	2.04	2.00e-2	2.21
4	8.52e-2	1.73	1.45	2.47	5.84e-3	1.78
5	3.18e-2	1.42	0.421	1.78	1.76e-3	1.73

Stokes flow in a moving domain

Although space-time methods can be highly competitive to tackle flows in fixed spatial domains as well as FSI problems, a scenario where a unified treatment of space and time is particularly advantageous lies somewhat inbetween: transport problems with prescribed motion of the spatial domain. In a rotary pump, for instance, the periodic angular motion of the gears leads the topology of the spatial domain to constantly change, which renders the simulation of fluid or heat flow by standard methods virtually unfeasible. In a space-time framework, on the other hand, provided that an appropriate triangulation of the "non-cylindrical" space-time domain is available, nothing else changes in comparison to

a standard problem with $\Omega(t) \equiv \Omega_0$ and $Q = \Omega_0 \times (0,T)$. That is, there is no need to employ expensive remeshing procedures or modify the conservation laws to include boundary motion terms *à la* arbitrary Lagrangian-Eulerian methods.

To test the accuracy of our space-time elements in a problem with moving spatial domain, we use once again a problem with analytical solution. To construct such a solution we will consider, in a moving annular domain $\Omega(t) \in \mathbb{R}^2$, a laminar flow driven by the radial motion of the inner wall. Let us first introduce the radial coordinate $r = \sqrt{{x_1}^2 + {x_2}^2}$ and the radial velocity $u_r(r,t)$, in the usual way. The spatial domain is initially an annulus Ω_0 with inner and outer radii equal to r_0 and R, respectively. The outer boundary is fixed, while the inner one moves radially according to a given function $r_i(t)$. Modelling the inner boundary as an impermeable wall yields

$$u_r|_{r=r_i} = [r_i(t)]'. \tag{8.28}$$

Moreover, conservation of mass and circumferential symmetry (purely radial motion) leads to

$$u_r(r,t) = R\frac{V(t)}{r}, \tag{8.29}$$

where $V(t)$ is the radial velocity on the outer boundary $r = R$. Therefore, the balance of linear momentum in the radial direction reduces to

$$\frac{1}{\rho}\frac{\partial p}{\partial r} = \chi\frac{R^2}{r^3}V^2(t) - \frac{R}{r}V'(t), \tag{8.30}$$

in which $\chi = 1$ and $\chi = 0$ correspond to the Navier–Stokes and Stokes systems, respectively. Integration with respect to r leads to

$$p(r,t) = P(t) + \chi\frac{\rho}{2}\left(1 - \frac{R^2}{r^2}\right)V^2(t) + \rho R\log\left(\frac{R}{r}\right)V'(t), \tag{8.31}$$

with $P(t)$ denoting the pressure on the outer boundary. Combining (8.28) and (8.29) then yields

$$V(t) = \frac{1}{2R}\frac{\mathrm{d}}{\mathrm{d}t}\left\{[r_i(t)]^2\right\}, \tag{8.32}$$

so that the analytical solution is determined by choosing $r_i(t)$ and $P(t)$.

For the numerical example we set $R = \rho = \mu = 1$ and a pulsatile inner wall motion

$$r_i(t) = [1 + A\sin(2\pi t/T)]\, r_0,$$

where $r_0 = R/2$, $A = 1/4$ and $T = 2$ is the time horizon of the simulation. As for the pressure scaling, we enforce $p = 0$ at $(x_1,x_2) = (R,0)$, which leads to $P(t) \equiv 0$. Five tetrahedral meshes are considered, the finest of which is depicted in Figure 8.4. As shown in Table 8.4 for the Stokes solution ($\chi = 0$), the convergence follows the same trends observed for fixed spatial domains.

Table 8.4: Stokes problem in a pulsating annulus: mesh convergence study.

Mesh	$\|\nabla \boldsymbol{u} - \nabla \boldsymbol{u}_h\|_0$	eoc	$\|\partial_t \boldsymbol{u} - \partial_t \boldsymbol{u}_h\|_0$	eoc	$\|p - p_h\|_0$	eoc
1	1.84e-1	–	1.05e-1	–	3.71e-0	–
2	4.61e-2	1.99	2.90e-2	1.86	4.33e-1	3.10
3	1.16e-2	2.00	9.74e-3	1.57	9.14e-2	2.24
4	2.87e-3	2.01	3.65e-3	1.41	2.08e-2	2.13
5	7.10e-4	2.01	1.58e-3	1.20	5.05e-3	2.04

Carreau fluid past a two-dimensional backward-facing step

Benchmark solutions for time-dependent non-Newtonian problems are extremely scarce in the literature. We therefore consider a ramped-up solution based on the stationary BFS problem tackled in Section 4.3, and compare the final solution to that of Siebert and Fodor [165]. The space-time setup and mesh are illustrated in Figures 8.6 and 8.5. We use a parabolic inlet profile with flow rate $Q(t)$ ramped up smoothly from zero to $Q_{\max}$ as in Eq. (7.32), with $\tau = 0.4$ s, $T = 0.6$ s and $Q_{\max} = 25$ mm^2/s. The qualitative comparison depicted in Figure 8.5 reveals very good agreement. We see once again the spurious outflow behaviour caused by real traction BCs.

Manufactured Stokes flow solution in three spatial dimensions

We finally tackle a problem in a four-dimensional space-time domain $\mathrm{Q} = (0,1)^4$. The settings are $\mathrm{Re} = 1$, homogeneous initial and boundary data and a body force $\boldsymbol{f} = \boldsymbol{f}_t + \boldsymbol{f}_x$, with

$$\boldsymbol{f}_t = \begin{pmatrix} x^2 y e^{-t}(x-1)^2(z^2-z)(2y^2-3y+1) \\ 2xy^2 e^{-t}(y-1)^2(z-z^2)(2x^2-3x+1) \\ 0 \end{pmatrix},$$

$$\boldsymbol{f}_x = \begin{pmatrix} 4(e^{-t}-1)(2y-1)\{(z^2-z)[3(x^2-x)^2+(6(x^2-x)+1)y^2-6(x^2-x)y-y]+(y^2-y)(x^2-x)^2\} \\ 4(1-e^{-t})(2x-1)\{(z^2-z)(3(y^2-y)^2+(6(y^2-y)+1)x^2-6(y^2-y)x-x)+(x^2-x)(y^2-y)^2\} \\ e^{-t}(1-2z) \end{pmatrix},$$

where (x_1, x_2, x_3) are denoted as (x, y, z) to shorten the expressions. We then get

$$p = z(1-z)e^{-t}, \quad \boldsymbol{u} = \begin{pmatrix} (e^{-t}-1)x^2(x-1)^2(4y^3-6y^2+2y)(z^2-z) \\ (1-e^{-t})y^2(y-1)^2(4x^3-6x^2+2x)(z^2-z) \\ 0 \end{pmatrix}.$$

For this example we construct four-dimensional prismatic elements by extruding tetrahedral elements in time. At the coarsest level, the mesh is generated from the tetrahedral mesh shown in Figure 8.2 (top), with the time interval divided into two equal segments. Then, due to memory limitations, only two levels of uniform refinement are applied (the

next level would result in over 7.5 million degrees of freedom). The results of the refinement study, shown in Table 8.5, reveal similar trends as in the two-dimensional examples.

Table 8.5: Stokes problem in three spatial dimensions: mesh convergence study.

Mesh	$\|\nabla \boldsymbol{u} - \nabla \boldsymbol{u}_h\|_0$	eoc	$\|\partial_t \boldsymbol{u} - \partial_t \boldsymbol{u}_h\|_0$	eoc	$\|p - p_h\|_0$	eoc
1	1.49e-0	–	1.61e-0	–	5.80e-0	–
2	5.80e-1	1.36	5.23e-1	1.62	1.42e-1	2.02
3	1.73e-1	1.75	1.69e-1	1.63	3.55e-2	2.00

8.3.2 Solver performance

To demonstrate important aspects of our FETI solver, we use the first numerical example in this chapter as a test case. A family of four uniformly refined meshes is considered, the coarsest and finest of which are illustrated in Figure 8.8. Figure 8.9 depicts the different decompositions adopted, and Table 8.6 shows the corresponding number of Lagrange multipliers for the cases with continuous and discontinuous interface pressure. Note that the floating case (decomposition *e*) is not possible on the coarsest mesh. A relative of 10^{-6} is set for the iterative solver.

Table 8.6: Number of interface unknowns for various decompositions and refinement levels, with continuous (left) and discontinuous (right) interface pressures.

Mesh \DD	a)	b)	c)	d)	e)
1	95 | 82	95 | 82	141 | 122	149 | 128	–
2	331 | 290	331 | 290	495 | 434	508 | 444	383 | 338
3	1235 | 1090	1235 | 1090	1851 | 1634	1874 | 1652	1483 | 1314
4	4771 | 4226	4771 | 4226	7155 | 6338	7198 | 6372	5843 | 5186

We first consider the fully continuous setting without preconditioning. Those results are then compared to test cases where the Jacobi preconditioner (JPD) is used in Eq. (8.22). The comparison shown in Table 8.7 reveals important trends. We can see how the direction of the cut affects the performance of the iterative solver. When the interface is normal to the temporal direction, the number of iterations is considerably lower. The solver performs similarly whether the interface is parallel or oblique to time. The hardest cases to solve seem to be those in which the interface changes direction. Also remarkable is the considerable effect that a simple preconditioner can have on the solver's performance: we attain a reduction not only in the number of iterations, but also in the rate at which it grows with

the refinement. These observations highlight the need for appropriate preconditioners in space-time domain decomposition methods.

Table 8.8 and Figure 8.10 exhibit, respectively, the number of iterations and the residual evolution for the approach with discontinuous interface pressure, also using the Jacobi preconditioner. The comparison with the fully continuous case reveals a very similar performance for almost all configurations. The slightly smaller iteration count for the discontinuous approach can be associated to the reduced number of interface unknowns.

Table 8.7: FETI with continuous pressure: iterations without (left) and with (right) JPD.

Mesh \DD	a)	b)	c)	d)	e)
1	15 | 11	26 | 13	31 | 15	36 | 19	–
2	25 | 13	54 | 17	57 | 20	79 | 29	72 | 28
3	36 | 17	94 | 22	105 | 27	165 | 44	181 | 50
4	55 | 22	180 | 34	206 | 39	374 | 66	325 | 83

Table 8.8: FETI with discontinuous interface pressure: iterations with a Jacobi preconditioner.

Mesh \DD	a)	b)	c)	d)	e)
1	8	11	12	16	–
2	9	16	16	22	28
3	13	21	22	35	47
4	18	33	34	60	66

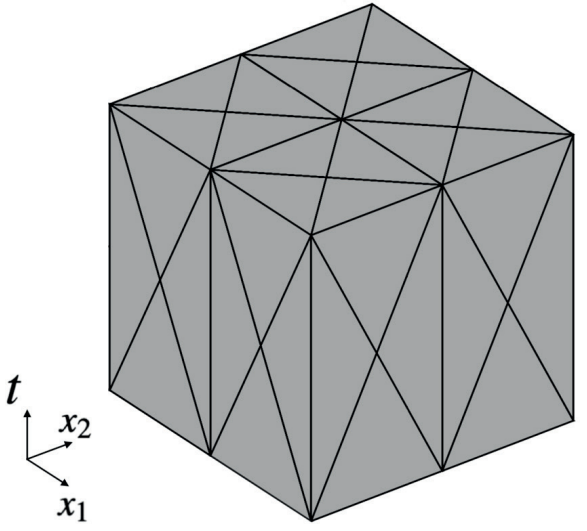

(a) Mesh 1 (coarsest).

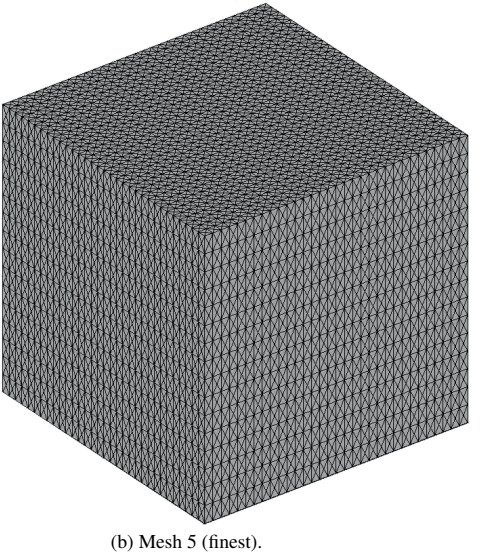

(b) Mesh 5 (finest).

Figure 8.2: Stokes problem: coarsest and finest meshes used in the convergence study.

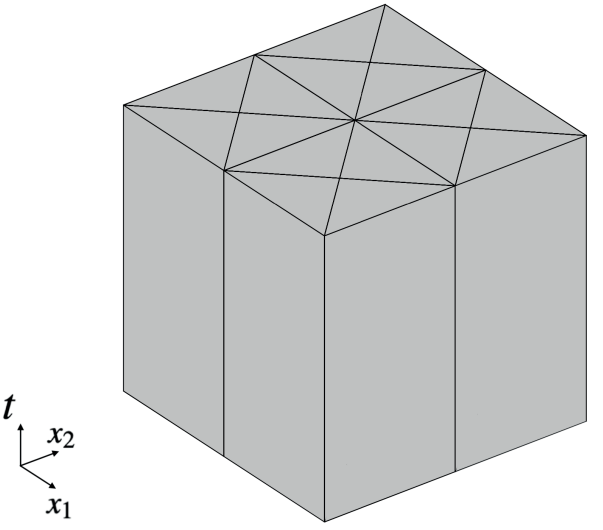

(a) Mesh 1 (coarsest).

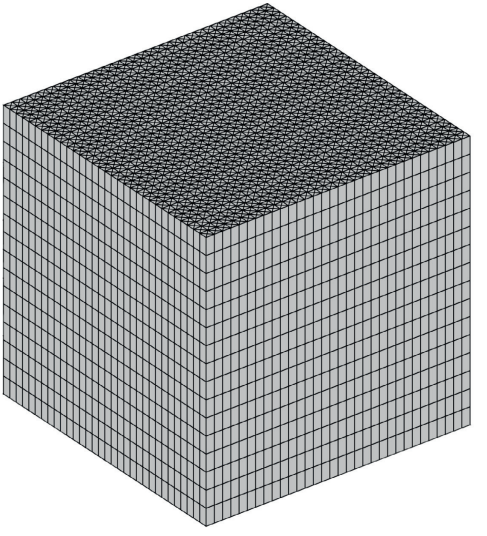

(b) Mesh 5 (finest).

Figure 8.3: Taylor–Green vortex: coarsest and finest meshes used in the convergence study.

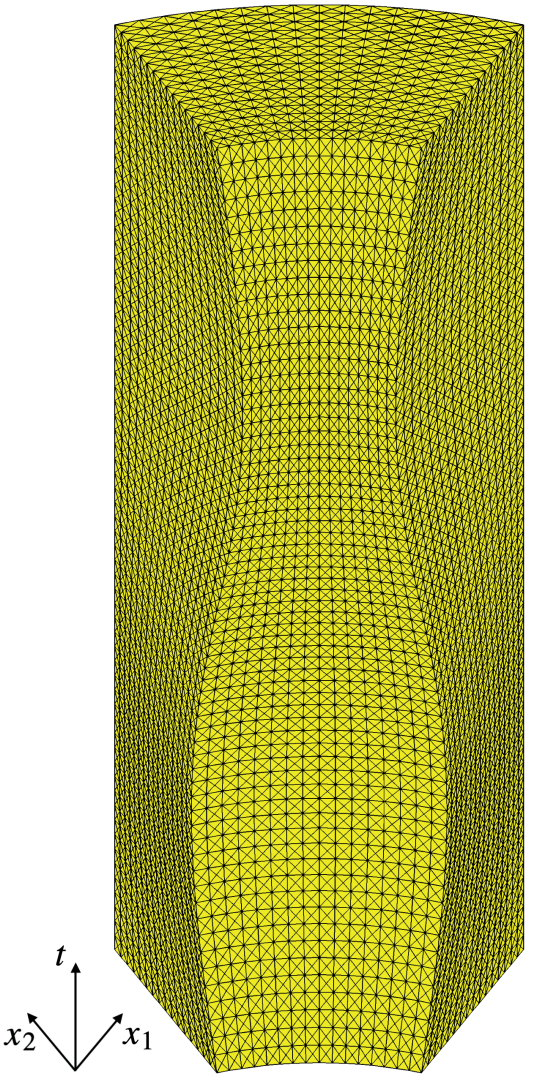

Figure 8.4: Stokes problem in a pulsating annulus: discretisation of the space-time domain with tetrahedral elements.

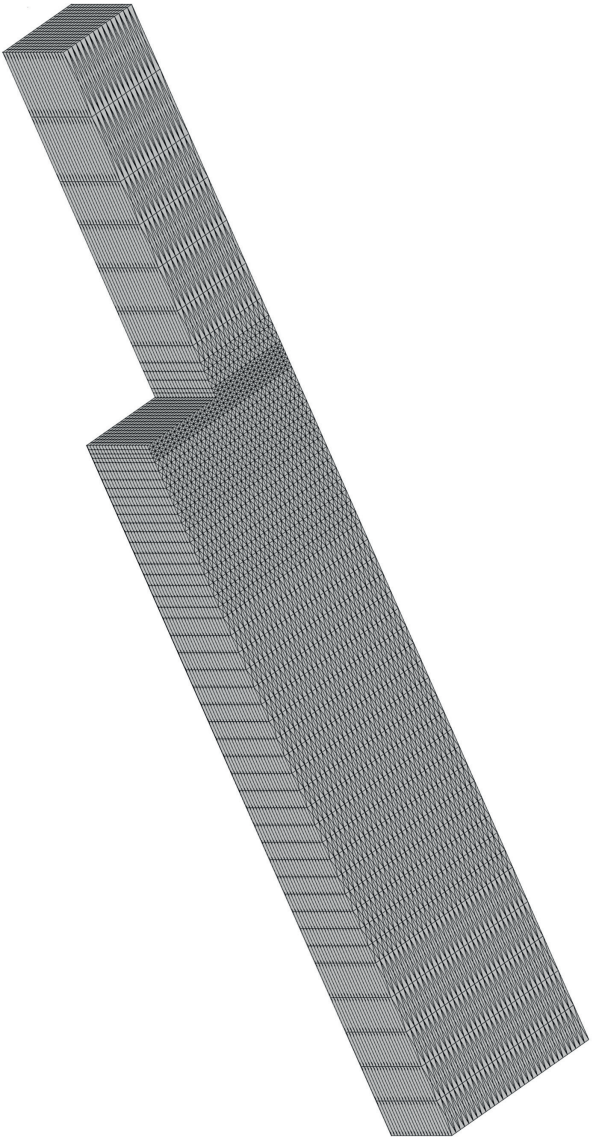

Figure 8.5: Backward-facing step: space-time mesh.

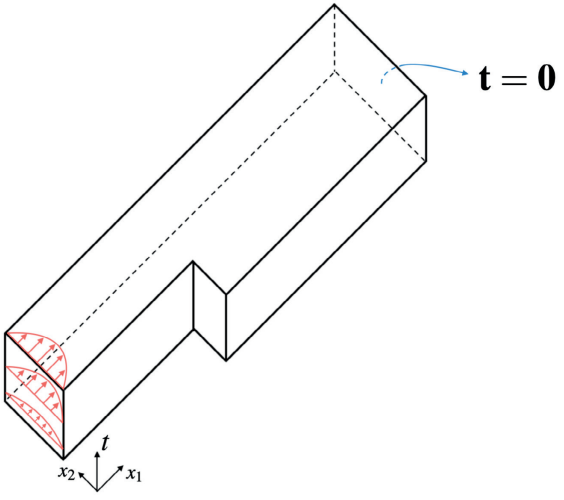

Figure 8.6: Backward-facing step: space-time problem setup.

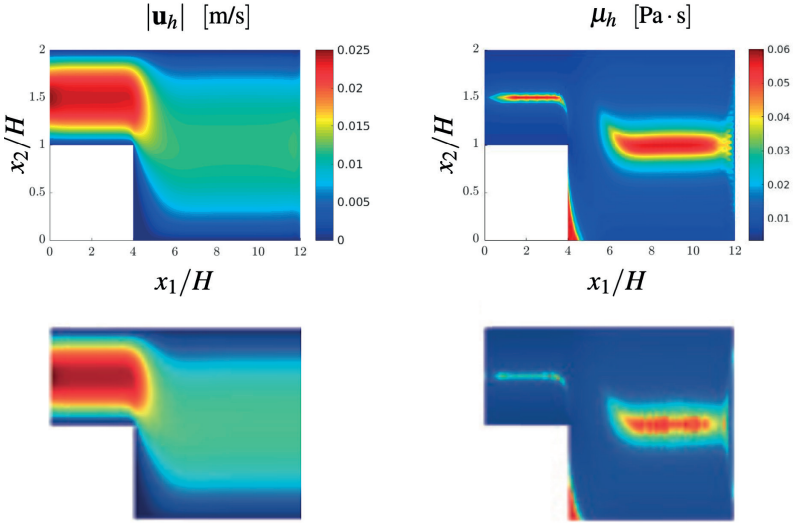

Figure 8.7: Backward-facing step: qualitative comparison between present results (top) and the reference solution by Siebert and Fodor [165] (bottom).

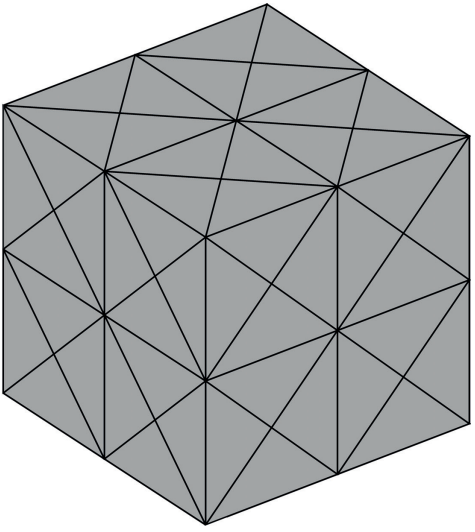

(a) Mesh 1 (192 elements).

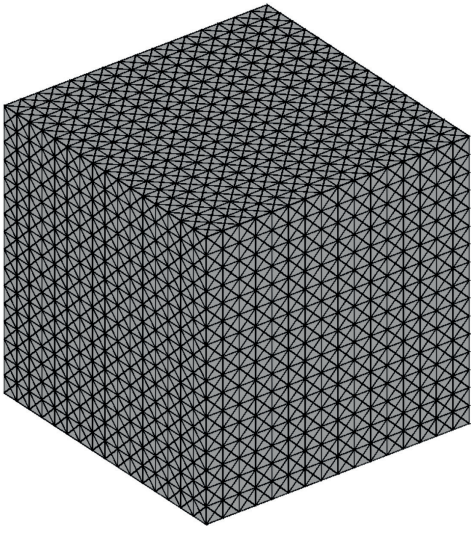

(b) Mesh 4 (98304 elements).

Figure 8.8: Coarsest and finest meshes used in the FETI study.

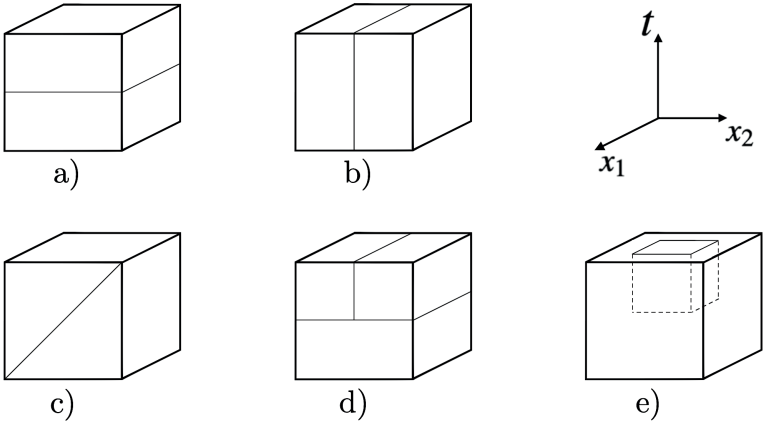

Figure 8.9: Different domain decompositions considered in the FETI study.

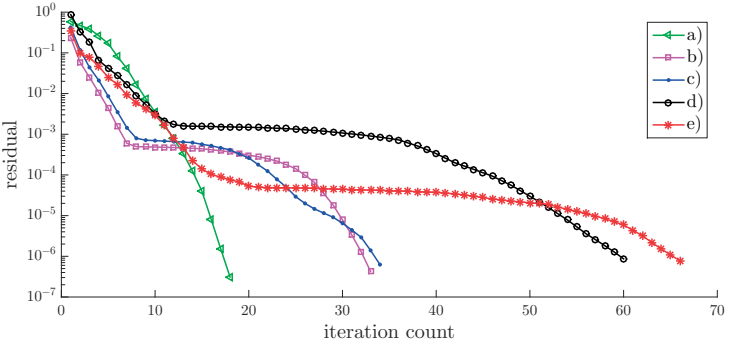

Figure 8.10: FETI with discontinuous interface pressure: residual evolution at the finest mesh for the diagonally preconditioned solver.

9 OUTLOOK AND OPEN PROBLEMS

In this final chapter, we summarise the various parts of this work and outline open problems and possible extensions. We began this investigation by setting ourselves the goal of developing accurate, efficient, reliable numerical methods for generalised Newtonian computational fluid dynamics. In highly applied fields such as biomedical engineering, the need for quick, simple solutions often leads to the use of techniques that are readily available but might not always be suitable or ideal for the desired application. In particular, when investigating the state of the art in finite element methods for blood flows, we ended up finding considerable room for improvement with respect to the techniques employed for solving non-Newtonian problems. In that context, relevant gaps which we took upon ourselves to fill include various aspects such as boundary conditions, pressure stabilisation methods and temporal discretisation schemes.

After introducing the background for our investigation in Chapters 1 and 2, we presented in Chapter 3 the standard variational formulation for quasi-Newtonian fluid flow problems. A major issue in those problems is the presence of natural boundary conditions not suitable as outflow data. In fact, the standard approach in the non-Newtonian case is to prescribe zero or constant outflow traction, which is widely known to produce nonphysical oscillations. We have then shown how *pseudo-tractions* can be used to appropriately enforce outflow conditions and presented two techniques for enforcing such data. Several numerical examples were provided to qualitatively and quantitatively showcase the accuracy of the formulations we introduced.

Chapter 5 is dedicated to the so-called pressure Poisson equation (PPE), which is a classical mathematical tool in inverse hemodynamics. This boundary value problem, derived directly from the Navier–Stokes momentum equation, is typically used for computing pressure fields from measured/given flow velocities. Our first contribution there was to extend the formulation to a very general framework allowing non-Newtonian and even compressible flow behaviour. Furthermore, we have introduced an *ultra-weak* finite element method allowing discontinuous pressure spaces, which is not possible in standard weak formulations. As a trade-off, test functions with continuous derivatives must be constructed, as we have presented for the case of piecewise constant pressure approximations in tensor-product meshes. The main open problem here is devising a robust framework that does not require Cartesian meshes, so that realistic domains can be considered. A promising idea for realising this is to use unfitted discretisations in which a geometry-independent background mesh is used, while the actual domain is implicitly described (see Figure 9.1). Unfitted finite element methods have very recently been used in problems where smooth

basis functions are required [166]. Mind that not only can ultra-weak formulations profit from unfitted methods, but the latter can also benefit from the former. In the unfitted framework, Dirichlet boundary conditions must be enforced weakly, which is in most cases done via Nitsche-type methods that add artificial terms to the variational formulation [167]. In the ultra-weak framework, on the other hand, Dirichlet data can be weakly enforced via boundary terms arising naturally from integration by parts. The combination of ultra-weak and unfitted methods has thus great potential to increase robustness of discretisations for challenging applications such as fluid-structure interaction and multi-phase flow problems.

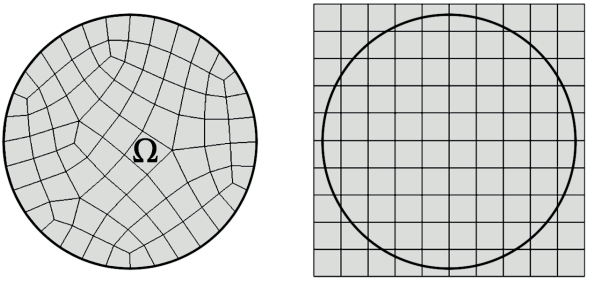

Figure 9.1: Illustration of fitted (left) and unfitted (right) meshes for a circular domain.

As it turns out, pressure Poisson problems can be used not only in computing pressure from given velocities, but also to design accurate flow solvers. In Chapter 6, we introduced a family of fully consistent PPE-based stabilisation methods for the equal-order discretisation of pressure and velocity in generalised Newtonian problems. This solves a major issue of standard residual-based pressure stabilisation methods, namely, the presence of numerical boundary layers when first-order elements are used. Although our new framework has a very similar structure, implementation and cost as standard stabilisation methods, it not only eliminates spurious pressure boundary layers, but also improves mass conservation and parameter-robustness. Several numerical examples have been provided to demonstrate that our approach consistently outperforms existing residual-based pressure stabilisation methods, not only for linear but also for higher-order elements.

As another extension of the generalised PPE framework developed in Chapter 5, we presented in Chapter 7 a split-step framework decoupling pressure, velocity and viscosity in time-dependent problems. The idea there is to use a slightly modified pressure Poisson problem with suitable boundary conditions to write pressure in terms of velocity and enforce incompressibility in an indirect way. This results in highly efficient time-stepping schemes that require only the solution of scalar convection-diffusion and Poisson problems and allow discretisations of both equal or compatible orders. An interesting extension will be to consider non-Newtonian fluid models with pressure-dependent viscosity, as

appearing for instance in dense granular flows [33]. When that is the case, the unique solvability of the resulting boundary value problem may be dependent on the pressure range [168, 169]. Hence, stability properties that we herein took for granted – due to having a linear Poisson equation for the pressure – may no longer hold, and appropriate regularisation and linearisation methods must be employed to guarantee accuracy and efficiency. Other relevant and challenging applications to which our pressure Poisson framework can be extended include viscoelastic fluids [29] and variable-density (but still incompressible) flows [170, 171].

At last, providing an alternative to the still dominant trend of equal-order time-stepping solvers, we have introduced a family of *stable* space-time finite elements for general incompressible flow problems. These elements are extensions of the famous (spatial) Taylor–Hood elements and, as such, yield stable and optimally convergent approximations. This is what our extensive numerical experiments indicate, yet theoretical stability and error estimates for this mixed finite element method are, at the moment of writing, still an open problem. We have further presented a new domain decomposition method for the resulting space-time algebraic system, which allows easy parallelisation in both space and time. This is important especially when handling realistic three-dimensional flows leading to large space-time systems. The main open task there is the development of appropriate preconditioners for the iterative solvers used for the global problem. Another current topic of intense investigation by the space-time community is the robust, automatic generation of adaptive four-dimensional meshes. Although time-stepping schemes such as the ones presented in Chapter 7 offer an efficient, simple way to handle large problems without the need for great processing and memory capacity, we believe that parallel space-time methods have the potential to be real game changers in next-generation high performance computing.

In order to cover the very different gaps mentioned in the beginning of this chapter, it was necessary to move through different areas of computational fluid dynamics rather than focusing on a single method, framework or application. This is why we have dealt with stable and stabilised formulations, time-stepping and space-time methods, weak and ultra-weak problems, Newtonian and non-Newtonian models. We believe that labelling a single method or model as "superior" would be, if nothing else, naive. Selecting the best suited approach for a specific application always depends on the availability of computational resources, the quality of data and the final goals – among other factors.

For instance, inf-sup-stable and higher-order elements are often excellent choices, but sometimes in biomedical applications one has no alternative but to work with very rough, non-smooth meshes coming from image segmentation. In such cases, stabilised first-order elements are often the (pragmatic) way to go. Another example is the *time-stepping vs. space-time* discussion. When all which is available are standard computers and software, split-step methods such as presented in Chapter 7 can be powerful tools, as they

allow one to easily turn simple “heat equation solvers” into efficient incompressible non-Newtonian flow solvers. On the other hand, it is a known fact that the algebraic systems arising from time-stepping schemes are often too small to fully benefit from the capabilities of modern supercomputers, so that parallel space-time methods become a very attractive option. Also when it comes to rheological modelling, in some cases there may be so much uncertainty in experimental or patient-specific data that the efforts in building and implementing sophisticated non-Newtonian models might eventually not pay off in comparison to a standard Newtonian approach.

In this context, we sincerely believe to have presented herein robust, reliable techniques that improve or extend relevant features in the state of the art of (incompressible) computational fluid dynamics, especially for quasi-Newtonian fluids. Although the numerical examples we provided are in most cases simple manufactured or benchmark problems, we are confident that they provide a clear picture of the issues and features we meant to show and make a strong case for the improvements we achieved.

REFERENCES

[1] G.P. Galdi, R. Rannacher, A.M. Robertson, and S. Turek. *Hemodynamical Flows: Modeling, Analysis and Simulation*, volume 37 of *Oberwolfach Seminars*. Birkhäuser, Basel, 2008.

[2] S. Chien. Shear dependence of effective cell volume as a determinant of blood viscosity. *Science*, 168(3934):977–979, 1970.

[3] S. Chien, R.G. King, R. Skalak, S. Usami, and A.L. Copley. Viscoelastic properties of human blood and red cell suspensions. *Biorheology*, 12(6):341–346, 1975.

[4] Y.I. Cho and K.R. Kensey. Effects of the non-Newtonian viscosity of blood on flows in a diseased arterial vessel. Part 1: Steady flows. *Biorheology*, 28:241–62, 1991.

[5] T.J.R. Hughes, L.P. Franca, and M. Balestra. A new finite element formulation for computational fluid dynamics: V. Circumventing the Babuška-Brezzi condition: a stable Petrov-Galerkin formulation of the stokes problem accommodating equal-order interpolations. *Comput. Methods Appl. Mech. Eng.*, 59(1):85–99, 1986.

[6] T.J.R. Hughes and L.P. Franca. A new finite element formulation for computational fluid dynamics: VII. The Stokes problem with various well-posed boundary conditions: Symmetric formulations that converge for all velocity/pressure spaces. *Comput. Methods Appl. Mech. Eng.*, 65(1):85–96, 1987.

[7] L. Rubart and G. Böhme. Numerical simulation of shear-thinning flow problems in mixing vessels. *Theor. Comput. Fluid Dyn.*, 3(2):95–115, 1991.

[8] H. R. Tamaddon-Jahromi, D. Ding, M. F. Webster, and P. Townsend. A Taylor–Galerkin finite element method for non-Newtonian flows. *Int. J. Numer. Methods Eng.*, 34(3):741–757, 1992.

[9] J.P.W. Baaijens, A.A. van Steenhoven, and J.D. Janssen. Numerical analysis of steady generalized Newtonian blood flow in a 2D model of the carotid artery bifurcation. *Biorheology*, 60(1):63–74, 1993.

[10] C. Tu and M. Deville. Pulsatile flow of non-Newtonian fluids through arterial stenoses. *J. Biomech.*, 29(7):899–908, 1996.

[11] N. Arada, M. Pires, and A. Sequeira. Viscosity effects on flows of generalized Newtonian fluids through curved pipes. *Comput. Math. Appl.*, 53(3-4):625–646, 2007.

[12] W.L. Barth, L.V. Branets, and G.F. Carey. Non-Newtonian flow in branched pipes and artery models. *Int. J. Numer. Meth. Fluids*, 57(5):531–553, 2008.

[13] M.G.H.M. Baltussen, Y.J. Choi, M.A. Hulsen, and P.D. Anderson. Weakly-imposed Dirichlet boundary conditions for non-Newtonian fluid flow. *J. Non-Newton. Fluid Mech.*, 166(17-18):993–1003, 2011.

[14] H. Lee. Numerical approximation of quasi-Newtonian flows by ALE-FEM. *Numer. Methods Partial Differ. Equ.*, 28(5):1667–1695, 2012.

[15] H. Damanik, J. Hron, A. Ouazzi, and S. Turek. Monolithic Newton-multigrid solution techniques for incompressible nonlinear flow models. *Int. J. Numer. Meth. Fluids*, 71(2):208–222, 2013.

[16] X. Zheng, G. Chen, and X. Xie. A divergence-free weak Galerkin method for quasi-Newtonian Stokes flows. *Sci. China Math.*, 60(8):1515–1528, 2017.

[17] N. Fehn, M. Kronbichler, C. Lehrenfeld, G. Lube, and P.W. Schroeder. High-order DG solvers for underresolved turbulent incompressible flows: A comparison of L^2 and $H(\mathrm{div})$ methods. *Int. J. Numer. Meth. Fluids*, 91(11):533–556, 2019.

[18] B. Blais, L. Barbeau, V. Bibeau, S. Gauvin, T.E. Geitani, S. Golshan, R. Kamble, G. Mirakhori, and J. Chaouki. Lethe: An open-source parallel high-order adaptative CFD solver for incompressible flows. *SoftwareX*, 12:100579, 2020.

[19] H. Sobhani, M. Razavi-Nouri, and M.H.R. Ghoreishy. Investigation of combination of finite element formulation and element type on the accuracy of 3D modeling of polymeric fluid flow in an extrusion die. *J. Appl. Polym. Sci.*, 120(3):1607–1615, 2011.

[20] G.F. Carey, K.C. Wang, and W.D. Joubert. Performance of iterative methods for Newtonian and generalized Newtonian flows. *Int. J. Numer. Meth. Fluids*, 9(2): 127–150, 1989.

[21] G. Böhme and L. Rubart. Non-Newtonian flow analysis by finite elements. *Fluid Dyn. Res.*, 5(3):147–158, 1989.

[22] M. Franta, J. Málek, and K.R. Rajagopal. On steady flows of fluids with pressure– and shear–dependent viscosities. *Proc. Math. Phys. Eng. Sci.*, 461(2055):651–670, 2005.

[23] F. Brezzi and J. Pitkäranta. On the stabilization of finite element approximations of the Stokes equations. In W. Hackbusch, editor, *Efficient solutions of elliptic systems*, pages 11–19. Notes on Numerical Fluid Mechanics, 1984.

[24] S. Knauf, S. Frei, T. Richter, and R. Rannacher. Towards a complete numerical description of lubricant film dynamics in ball bearings. *Comput. Mech.*, 53(2):239–255, 2014.

[25] C.R. Dohrmann and P.B. Bochev. A stabilized finite element method for the Stokes problem based on polynomial pressure projections. *Int. J. Numer. Meth. Fluids*, 46 (2):183–201, 2004.

[26] L. John, P. Pustějovská, and O. Steinbach. On the influence of the wall shear stress vector form on hemodynamic indicators. *Comput. Vis. Sci.*, 18(4-5):113–122, 2017.

[27] N.S. Hanspal, A.N. Waghode, V. Nassehi, and R.J. Wakeman. Numerical Analysis of Coupled Stokes/Darcy Flows in Industrial Filtrations. *Transp. Porous Media*, 64 (1):73–101, 2006.

[28] K. Chitra, T. Sundararajan, S. Vengadesan, and P. Nithiarasu. Non-Newtonian blood flow study in a model cavopulmonary vascular system. *Int. J. Numer. Meth. Fluids*, 66(3):269–283, 2011.

[29] I.G. Donev and B.D. Reddy. Time-dependent finite element simulations of a shear-thinning viscoelastic fluid with application to blood flow. *Int. J. Numer. Meth. Fluids*, 75(9):668–686, 2014.

[30] W. Gao and R. Liu. A hybrid finite volume/finite element method for incompressible generalized Newtonian fluid flows on unstructured triangular meshes. *Acta Mech. Sin.*, 25(6):747–760, 2009.

[31] B. Hübner and D. Dinkler. A simultaneous solution procedure for strong interactions of generalized Newtonian fluids and viscoelastic solids at large strains. *Int. J. Numer. Methods Eng.*, 64(7):920–939, 2005.

[32] V.L. Marrero, J.A. Tichy, O. Sahni, and K.E. Jansen. Numerical study of purely ciscous non-Newtonian flow in an abdominal aortic aneurysm. *J. Biomech. Eng.*, 136(10), 2014.

[33] L. Gesenhues, J.J. Camata, A.M.A. Côrtes, F.A. Rochinha, and A.L.G.A. Coutinho. Finite element simulation of complex dense granular flows using a well-posed regularization of the μ(I)-rheology. *Comput. Fluids*, 188:102–113, 2019.

[34] F. Zinani and S. Frey. Finite element approximations for quasi-Newtonian flows employing a multi-field GLS method. *Comput. Mech.*, 48(2):139–152, 2011.

[35] E. Castillo and R. Codina. Stabilized stress–velocity–pressure finite element formulations of the Navier–Stokes problem for fluids with non-linear viscosity. *Comput. Methods Appl. Mech. Eng.*, 279:554–578, 2014.

[36] A. Masud and J. Kwack. A stabilized mixed finite element method for the incompressible shear-rate dependent non-Newtonian fluids: Variational Multiscale framework and consistent linearization. *Comput. Methods Appl. Mech. Eng.*, 200(5-8): 577–596, 2011.

[37] M. Behr and T.E. Tezduyar. Finite element solution strategies for large-scale flow simulations. *Comput. Methods Appl. Mech. Eng.*, 112(1-4):3–24, 1994.

[38] M. Behr. Simplex space–time meshes in finite element simulations. *Int. J. Numer. Meth. Fluids*, 57(9):1421–1434, 2008.

[39] O. Steinbach and H. Yang. Comparison of algebraic multigrid methods for an adaptive space-time finite-element discretization of the heat equation in 3D and 4D. *Numer. Linear Algebra Appl.*, 25(3):e2143, 2018.

[40] R. Rannacher. On the numerical solution of the incompressible Navier-Stokes equations. *J. Appl. Math. Mech.*, 73(9):203–216, 1993.

[41] J.G. Heywood, R. Rannacher, and S. Turek. Artificial boundaries and flux and pressure conditions for the incompressible Navier-Stokes equations. *Int. J. Numer. Meth. Fluids*, 22(5):325–352, 1996.

[42] T. Richter. *Fluid-Structure interactions: models, analysis and finite elements*, volume 118 of *Lect. Notes Comput. Sci. Eng.* Springer, Cham, 2017.

[43] A. Coccarelli, A. Prakash, and P. Nithiarasu. A novel porous media-based approach to outflow boundary resistances of 1D arterial blood flow models. *Biomech. Model. Mechanobiol.*, 18(4):939–951, 2019.

[44] P.M. Gresho and R.L. Sani. On pressure boundary conditions for the incompressible Navier-Stokes equations. *Int. J. Numer. Meth. Fluids*, 7(10):1111–1145, 1987.

[45] K.U. Rehman, M.Y. Malik, R. Mahmood, N. Kousar, and I. Zehra. A potential alternative CFD simulation for steady Carreau–Bird law-based shear thickening model: Part-I. *J. Braz. Soc. Mech. Sci. & Eng.*, 41(4):176, 2019.

[46] A. Karim, M.M. Hossain, S. Parvin, and M.A.H. Khan. Hemodynamic blood flow through a section of human artery under the effect of applied magnetic field. *AIP Conf. Proc.*, 2121(1):050010, 2019.

[47] S. Dong, G. Karniadakis, and C. Chryssostomidis. A robust and accurate outflow boundary condition for incompressible flow simulations on severely-truncated unbounded domains. *J. Comput. Phys.*, 261:83–105, 2014.

[48] D. Arndt, M. Braack, and G. Lube. Finite elements for the Navier-Stokes problem with outflow condition. In *Lect. Notes Comput. Sci. Eng.*, pages 95–103. Springer, 2016.

[49] C. Bertoglio, A. Caiazzo, Y. Bazilevs, M. Braack, M. Esmaily, V. Gravemeier, A.L Marsden, O. Pironneau, I.E Vignon-Clementel, and W.A. Wall. Benchmark problems for numerical treatment of backflow at open boundaries. *Int. J. Numer. Methods Biomed. Eng.*, 34(2):e2918, 2018.

[50] G. Arbia, I. E. Vignon-Clementel, T.-Y. Hsia, and J.-F. Gerbeau. Modified Navier–Stokes equations for the outflow boundary conditions in hemodynamics. *Eur. J. Mech. B Fluids*, 60:175–188, 2016.

[51] M. Huber, U. Rüde, C. Waluga, and B. Wohlmuth. Surface couplings for subdomain-wise isoviscous gradient based Stokes finite element discretizations. *J. Sci. Comput.*, 74(2):895–919, 2018.

[52] N.R. Anturkar, T.C. Papanastasiou, and J.O. Wilkes. Stability of coextrusion through converging dies. *J. Non-Newton. Fluid Mech.*, 41(1-2):1–25, 1991.

[53] S.Y. Na and D.H. Kim. Three-dimensional modelling of Non-Newtonian fluid flow in a coat-hanger die. *Korean J. Chem. Eng.*, 12(2):236–243, 1995.

[54] D.R.Q. Pacheco, T.S. Müller, O. Steinbach, and G. Brenn. On outflow boundary conditions in finite element simulations of non-Newtonian internal flows. *Int. J. Comput. Vis. Sci. Eng.*, 1:4, 2021.

[55] P. Hood and C. Taylor. Navier-Stokes equations using mixed interpolation. In J.T. Oden, O.C. Zienkiewicz, R.H. Gallagher, and C. Taylor, editors, *Finite element methods in flow problems*, pages 57–66. UAH Press, 1974.

[56] F. Brezzi and R.S. Falk. Stability of higher-order Hood–Taylor methods. *SIAM J. Numer. Anal.*, 28(3):581–590, 1991.

[57] V. John. *Finite element methods for incompressible flow problems*. Springer, New York, 2016.

[58] J. Donea and A. Huerta. *Finite Element Methods for Flow Problems*. John Wiley & Sons, New York, 2003.

[59] A. Quarteroni and A. Valli. *Numerical Approximation of Partial Differential Equations*, volume 23. Springer, Berlin and Heidelberg, 1994.

[60] T.F. Chen, C.L. Cox, H.C. Lee, and K.L. Tung. Least-squares finite element methods for generalized Newtonian and viscoelastic flows. *Appl. Numer. Math.*, 60(10): 1024–1040, 2010.

[61] S. Serdas, A. Schwarz, J. Schröder, S. Turek, A. Ouazzi, and M. Nickaeen. Least-squares finite element methods for the Navier-Stokes equations for generalized Newtonian fluids. *Proc. Appl. Math. Mech*, 14(1):623–624, 2014.

[62] S. Münzenmaier. First-order system least squares for generalized-Newtonian coupled Stokes-Darcy flow. *Numer. Methods Partial Differ. Equ.*, 31(4):1150–1173, 2015.

[63] V.M. Verzhbitskii and I.F. Yumanova. On the quadratic convergence of the Aitken Δ^2 process. *Comput. Math. Math. Phys.*, 51(10):1659–1663, 2011.

[64] B.M. Irons and R.C. Tuck. A version of the Aitken accelerator for computer iteration. *Int. J. Numer. Methods Eng.*, 1(3):275–277, 1969.

[65] U. Küttler and W.A. Wall. Fixed-point fluid-structure interaction solvers with dynamic relaxation. *Comput. Mech.*, 43(1):61–72, 2008.

[66] T.C. Papanastasiou. Flows of materials with yield. *J. Rheol.*, 31(5):385–404, 1987.

[67] D.R.Q. Pacheco and O. Steinbach. A continuous finite element framework for the pressure Poisson equation allowing non-Newtonian and compressible flow behavior. *Int. J. Numer. Meth. Fluids*, 93:1435–1445, 2021.

[68] D.R.Q. Pacheco and O. Steinbach. On the pressure Poisson equation for the Stokes system. *Proc. Appl. Math. Mech*, 19(1):e201900425, 2019.

[69] D.R.Q. Pacheco and O. Steinbach. An ultra-weak finite element method for the pressure Poisson equation. *In preparation*, 2021.

[70] C. Bertoglio, R. Nuñez, F. Galarce, D. Nordsletten, and A. Osses. Relative pressure estimation from velocity measurements in blood flows: State-of-the-art and new approaches. *Int. J. Numer. Methods Biomed. Eng.*, 34(2):e2925, 2018.

[71] J. Liu. Open and traction boundary conditions for the incompressible Navier–Stokes equations. *J. Comput. Phys.*, 228(19):7250–7267, 2009.

[72] H. Johnston and J.-G. Liu. Accurate, stable and efficient Navier–Stokes solvers based on explicit treatment of the pressure term. *J. Comput. Phys.*, 199(1):221–259, 2004.

[73] D. Boffi, F. Brezzi, and M. Fortin. *Mixed finite element methods and applications*, volume 44. Springer, Berlin and Heidelberg, 2013.

[74] J. Petera and J.F.T. Pittman. Isoparametric Hermite elements. *Int. J. Numer. Methods Eng.*, 37(20):3489–3519, 1994.

[75] P. Fischer, J. Mergheim, and P. Steinmann. On the C^1 continuous discretization of non-linear gradient elasticity: A comparison of NEM and FEM based on Bernstein-Bézier patches. *Int. J. Numer. Methods Eng.*, 82(10):1282–1307, 2010.

[76] V. Domínguez and F.-J. Sayas. Algorithm 884: A simple Matlab implementation of the Argyris element. *ACM Trans. Math. Softw.*, 35(2):1–11, 2008.

[77] O. Amili, D. Schiavazzi, S. Moen, B. Jagadeesan, P.-F. Van de Moortele, and F. Coletti. Hemodynamics in a giant intracranial aneurysm characterized by in vitro 4D flow MRI. *PLoS One*, 13(1):e0188323, 2018.

[78] D.E. Schiavazzi, A. Nemes, S. Schmitter, and F. Coletti. The effect of velocity filtering in pressure estimation. *Exp. Fluids*, 58(5):50, 2017.

[79] D.R.Q. Pacheco, R. Schussnig, O. Steinbach, and T.-P. Fries. A global residual-based stabilization for equal-order finite element approximations of incompressible flows. *Int. J. Numer. Methods Eng.*, 122(8):2075–2094, 2021.

[80] R. Schussnig, D.R.Q. Pacheco, and T.-P. Fries. Robust stabilised finite element solvers for generalised Newtonian fluid flows. *J. Comput. Phys.*, 442(C):110436, 2021.

[81] D.R.Q. Pacheco and O. Steinbach. On an initial higher-order pressure convergence in stabilized finite element discretizations of the Stokes system. *In preparation*, 2021.

[82] E. Burman and P. Hansbo. Edge stabilization for the generalized Stokes problem: A continuous interior penalty method. *Comput. Methods Appl. Mech. Eng.*, 195 (19-22):2393–2410, 2006.

[83] T.-P. Fries and H.G. Matthies. A stabilized and coupled meshfree/meshbased method for the incompressible Navier–Stokes equations–Part II: Coupling. *Comput. Methods Appl. Mech. Eng.*, 195(44-47):6191–6204, 2006.

[84] J.-J. Droux and T.J.R. Hughes. A boundary integral modification of the Galerkin least squares formulation for the Stokes problem. *Comput. Methods Appl. Mech. Eng.*, 113(1-2):173–182, 1994.

[85] K. E. Jansen, S. S Collis, C. Whiting, and F. Shaki. A better consistency for low-order stabilized finite element methods. *Comput. Methods Appl. Mech. Eng.*, 174 (1-2):153–170, 1999.

[86] F. Brezzi and J. Douglas Jr. Stabilized mixed methods for the Stokes problem. *Numer. Math.*, 53(1-2):225–235, 1988.

[87] J. Douglas Jr. and J. Wang. An absolutely stabilized finite element method for the Stokes problem. *Math. Comput.*, 52(186):495, 1989.

[88] P. Bochev and M. Gunzburger. An absolutely stable pressure-Poisson stabilized finite element method for the Stokes equations. *SIAM J. Numer. Anal.*, 42(3):1189–1207, 2004.

[89] J. Hinz, J. Helmig, M. Möller, and S. Elgeti. Boundary-conforming finite element methods for twin-screw extruders using spline-based parameterization techniques. *Comput. Methods Appl. Mech. Eng.*, 361:112740, 2020.

[90] R. Codina and J. Blasco. A finite element formulation for the Stokes problem allowing equal velocity-pressure interpolation. *Comput. Methods Appl. Mech. Eng.*, 143(3-4):373–391, 1997.

[91] R. Codina and J. Blasco. Analysis of a pressure-stabilized finite element approximation of the stationary Navier-Stokes equations. *Numer. Math.*, 87(1):59–81, 2000.

[92] R. Codina, J. Blasco, G.C. Buscaglia, and A. Huerta. Implementation of a stabilized finite element formulation for the incompressible Navier-Stokes equations based on a pressure gradient projection. *Int. J. Numer. Meth. Fluids*, 37(4):419–444, 2001.

[93] R. Becker and M. Braack. A finite element pressure gradient stabilization for the Stokes equations based on local projections. *Calcolo*, 38(4):173–199, 2001.

[94] M. Braack and G. Lube. Finite elements with local projection stabilization for incompressible flow problems. *Journal of Computational Mathematics*, 27:116–147, 2009.

[95] E. Burman, M.A. Fernández, and P. Hansbo. Continuous interior penalty finite element method for Oseen's equations. *SIAM J. Numer. Anal.*, 44(3):1248–1274, 2006.

[96] L.P. Franca and S.L. Frey. Stabilized finite element methods: II. The incompressible Navier-Stokes equations. *Comput. Methods Appl. Mech. Eng.*, 99(2-3):209–233, 1992.

[97] L.P. Franca and T.J.R. Hughes. Two classes of mixed finite element methods. *Comput. Methods Appl. Mech. Eng.*, 69(1):89–129, 1988.

[98] M. Olshanskii, G. Lube, T. Heister, and J. Löwe. Grad–div stabilization and subgrid pressure models for the incompressible Navier–Stokes equations. *Comput. Methods Appl. Mech. Eng.*, 198(49-52):3975–3988, 2009.

[99] R. Hartmann. Higher-order and adaptive discontinuous Galerkin methods with shock-capturing applied to transonic turbulent delta wing flow. *Int. J. Numer. Meth. Fluids*, 72(8):883–894, 2013.

[100] L.P. Franca, T.J.R. Hughes, and R. Stenberg. Stabilized finite element methods. In M.D. Gunzburger and R.A. Nicolaides, editors, *Incompressible computational fluid dynamics: trends and advances.*, pages 87–107. Cambridge University Press, 1993.

[101] V. John, P. Knobloch, and U. Wilbrandt. Finite element pressure stabilizations for incompressible flow problems. In T. Bodnár, G. Galdi, and Š. Nečasová, editors, *Fluids Under Pressure. Advances in Mathematical Fluid Mechanics.*, pages 483–573. Birkhäuser, 2020.

[102] J.-G. Liu, J. Liu, and R.L. Pego. Error estimates for finite-element Navier-Stokes solvers without standard Inf-Sup conditions. *Chin. Ann. Math. Ser. B*, 30(6):743–768, 2009.

[103] J.-G. Liu, J. Liu, and R.L. Pego. Stable and accurate pressure approximation for unsteady incompressible viscous flow. *J. Comput. Phys.*, 229(9):3428–3453, 2010.

[104] D. Shirokoff and R.R. Rosales. An efficient method for the incompressible Navier–Stokes equations on irregular domains with no-slip boundary conditions, high order up to the boundary. *J. Comput. Phys.*, 230(23):8619–8646, 2011.

[105] J. Jia and J. Liu. Stable and spectrally accurate schemes for the Navier–Stokes equations. *SIAM J. Sci. Comput.*, 33(5):2421–2439, 2011.

[106] Z. Sheng, M. Thiriet, and F. Hecht. A high-order scheme for the incompressible Navier-Stokes equations with open boundary condition. *Int. J. Numer. Meth. Fluids*, 73(1):58–73, 2013.

[107] H. Johnston, C. Wang, and J.-G. Liu. A local pressure boundary condition spectral collocation scheme for the three-dimensional Navier–Stokes equations. *J. Sci. Comput.*, 60(3):612–626, 2014.

[108] L. Li. A split-step finite-element method for incompressible Navier-Stokes equations with high-order accuracy up-to the boundary. *J. Comput. Phys.*, 408:109274, 2020.

[109] R.R. Rosales, B. Seibold, D. Shirokoff, and D. Zhou. High-order finite element methods for a pressure Poisson equation reformulation of the Navier–Stokes equations with electric boundary conditions. *Comput. Methods Appl. Mech. Eng.*, 373: 113451, 2021.

[110] J.G. Heywood and R. Rannacher. Finite element approximation of the nonstationary Navier–Stokes problem. I. Regularity of solutions and second-order error estimates for spatial discretization. *SIAM J. Numer. Anal.*, 19(2):275–311, 1982.

[111] R.L. Sani, J. Shen, O. Pironneau, and P.M. Gresho. Pressure boundary condition for the time-dependent incompressible Navier–Stokes equations. *Int. J. Numer. Meth. Fluids*, 50(6):673–682, 2006.

[112] V. John, P. Knobloch, and U. Wilbrandt. Finite element pressure stabilizations for incompressible flow problems. In T. Bodnár, G. Galdi, and Š. Nečasová, editors, *Fluids Under Pressure. Advances in Mathematical Fluid Mechanics.*, pages 483–573. Birkhäuser, 2020.

[113] P.D. Weidman. Flows induced by the surface motions of a cylindrical sheet. *J. Eng. Math.*, 68(3-4):355–372, 2010.

[114] L.I.G. Kovasznay. Laminar flow behind a two-dimensional grid. *Math. Proc. Camb. Philos. Soc.*, 44(1):58–62, 1948.

[115] S. Groß and A. Reusken. An extended pressure finite element space for two-phase incompressible flows with surface tension. *J. Comput. Phys.*, 224(1):40–58, 2007.

[116] H. Eichel, L. Tobiska, and H. Xie. Supercloseness and superconvergence of stabilized low-order finite element discretizations of the Stokes Problem. *Math. Comput.*, 80(274):697–697, 2011.

[117] A. Cioncolini and D. Boffi. The MINI mixed finite element for the Stokes problem: An experimental investigation. *Comput. Math. Appl.*, 77(9):2432–2446, 2019.

[118] O. Steinbach. A note on initial higher-order convergence results for boundary element methods with approximated boundary conditions. *Numer. Methods Partial Differ. Equ.*, 16(6):581–588, 2000.

[119] L.J.P. Timmermans, P.D. Minev, and F.N. Van de Vosse. An approximate projection scheme for incompressible flow using spectral elements. *Int. J. Numer. Meth. Fluids*, 22(7):673–688, 1996.

[120] J.L. Guermond, P. Minev, and J. Shen. Error analysis of pressure-correction schemes for the time-dependent Stokes equations with open boundary conditions. *SIAM J. Numer. Anal.*, 43(1):239–258, 2005.

[121] A. Poux, S. Glockner, and M. Azaïez. Improvements on open and traction boundary conditions for Navier–Stokes time-splitting methods. *J. Comput. Phys.*, 230(10): 4011–4027, 2011.

[122] J.L. Guermond, P. Minev, and Jie Shen. An overview of projection methods for incompressible flows. *Comput. Methods Appl. Mech. Eng.*, 195(44):6011–6045, 2006.

[123] J. Deteix and D. Yakoubi. Improving the pressure accuracy in a projection scheme for incompressible fluids with variable viscosity. *Appl. Math. Lett.*, 79:111–117, 2018.

[124] L. Plasman, J. Deteix, and D. Yakoubi. A projection scheme for Navier-Stokes with variable viscosity and natural boundary condition. *Int. J. Numer. Meth. Fluids*, pages 1–21, 2020.

[125] J. Deteix and D. Yakoubi. Shear rate projection schemes for non-Newtonian fluids. *Comput. Methods Appl. Mech. Eng.*, 354:620–636, 2019.

[126] D.R.Q. Pacheco, R. Schussnig, and T.-P. Fries. An efficient split-step framework for non-Newtonian incompressible flow problems with consistent pressure boundary conditions. *Comput. Methods Appl. Mech. Eng.*, 382:113888, 2021.

[127] F. Meng, J.W. Banks, W.D. Henshaw, and D.W. Schwendeman. Fourth-order accurate fractional-step IMEX schemes for the incompressible Navier–Stokes equations on moving overlapping grids. *Comput. Methods Appl. Mech. Eng.*, 366:113040, 2020.

[128] E. Hairer, S.P. Nørsett, and G. Wanner. *Solving Ordinary Difference Equations 1 - Nonstiff problems*. Springer, 1993.

[129] H.W. Choi and A.I. Barakat. Numerical study of the impact of non-Newtonian blood behavior on flow over a two-dimensional backward facing step. *Biorheology*, 42(6): 493–509, 2005.

[130] M. Behr. Stabilized space-time finite element formulations for free-surface flows. *Int. J. Numer. Methods Eng.*, 17(11):813–819, 2001.

[131] M. Behr, D. Arora, O. M. Coronado, and M. Pasquali. Models and finite element techniques for blood flow simulation. *Int. J. Comput. Fluid Dyn.*, 20(3-4):175–181, 2006.

[132] L. Pauli and M. Behr. On stabilized space-time FEM for anisotropic meshes: Incompressible Navier-Stokes equations and applications to blood flow in medical devices. *Int. J. Numer. Meth. Fluids*, 85(3):189–209, 2017.

[133] J.J.W. van der Vegt and J.J. Sudirham. A space–time discontinuous Galerkin method for the time-dependent Oseen equations. *Appl. Numer. Math.*, 58(12):1892–1917, 2008.

[134] M. Neumüller and O. Steinbach. Refinement of flexible space-time finite element meshes and discontinuous Galerkin methods. *Comput. Vis. Sci.*, 14(5):189–205, 2011.

[135] S. Rhebergen, B. Cockburn, and J.J.W. van der Vegt. A space–time discontinuous Galerkin method for the incompressible Navier–Stokes equations. *J. Comput. Phys.*, 233:339–358, 2013.

[136] D.R.Q. Pacheco and O. Steinbach. Space-time Taylor–Hood elements for incompressible flows. *Computer Meth. Materials Sci.*, 19:64–69, 2019.

[137] D.R.Q. Pacheco and O. Steinbach. Space-time finite element tearing and interconnecting domain decomposition methods. In *Lect. Notes Comput. Sci. Eng.*, page accepted. Springer, 2021.

[138] D.R.Q. Pacheco and O. Steinbach. A stable space-time finite element method for the Stokes system. *In preparation*, 2021.

[139] M. Danwitz, V. Karyofylli, N. Hosters, and M. Behr. Simplex space–time meshes in compressible flow simulations. *Int. J. Numer. Meth. Fluids*, 91(1):29–48, 2019.

[140] O. Steinbach. Space-time finite element methods for parabolic problems. *Comput. Methods Appl. Math.*, 15(4):551–566, 2015.

[141] S. Mittal and T.E. Tezduyar. Notes on the stabilized space-time finite-element formulation of unsteady incompressible flows. *Comput. Phys. Commun.*, 73(1-3):93–112, 1992.

[142] S. Badia and M. Olm. Space-time balancing domain decomposition. *SIAM J. Sci. Comput.*, 39(2):C194–C213, 2017.

[143] S. Ali Hassan, C. Japhet, and M. Vohralík. A posteriori stopping criteria for space-time domain decomposition for the heat equation in mixed formulations. *Electron. Trans. Numer. Anal.*, 49:151–181, 2018.

[144] G. Singh and M.F. Wheeler. A space–time domain decomposition approach using enhanced velocity mixed finite element method. *J. Comput. Phys.*, 374:893–911, 2018.

[145] N. Chamakuri. Parallel and space-time adaptivity for the numerical simulation of cardiac action potentials. *Appl. Math. Comput.*, 353:406–417, 2019.

[146] D. Gilliocq-Hirtz and Z. Belhachmi. A space-time parallel method for the optic flow estimation in large displacements and varying illumination case. *Int. J. Numer. Anal. Model.*, 1(16):116–138, 2019.

[147] Y. Takahashi, K. Fujiwara, T. Iwashita, and H. Nakashima. Parallel finite-element method based on space–time domain decomposition for magnetic field analysis of electric machines. *IEEE Trans. Magn.*, 55(6):1–4, 2019.

[148] C. Farhat and F.-X. Roux. A method of finite element tearing and interconnecting and its parallel solution algorithm. *Int. J. Numer. Methods Eng.*, 32(6):1205–1227, 1991.

[149] M. Beneš, T. Krejčí, and J. Kruis. A FETI-based mixed explicit–implicit multi-time-step method for parabolic problems. *J. Comput. Appl. Math.*, 333:247–265, 2018.

[150] C. Pechstein. *Finite and boundary element tearing and interconnecting solvers for multi-scale problems*, volume 90 of *Lect. Notes Comput. Sci. Eng.* Springer, Berlin, 2013.

[151] C. Calgaro and J. Laminie. On the domain decomposition method for the generalized Stokes problem with continuous pressure. *Numer. Methods Partial Differ. Equ.*, 16(1):84–106, 2000.

[152] Y. Saad and M.H. Schultz. GMRES: a generalized minimal residual algorithm for solving nonsymmetric linear systems. *SIAM J. Sci. Comput.*, 7(3):856–869, 1986.

[153] A. Toselli. FETI domain decomposition methods for scalar advection–diffusion problems. *Comput. Methods Appl. Mech. Eng.*, 190(43-44):5759–5776, 2001.

[154] R. Kučera, T. Kozubek, A. Markopoulos, J. Haslinger, and L. Mocek. Projected Krylov methods for solving non-symmetric two-by-two block linear systems arising from fictitious domain formulations. *Adv. Electr. Electron. Eng.*, 12(2), 2014.

[155] B. Vereecke, H. Bavestrello, and D. Dureisseix. An extension of the FETI domain decomposition method for incompressible and nearly incompressible problems. *Comput. Methods Appl. Mech. Eng.*, 192(31-32):3409–3429, 2003.

[156] A. Klawonn and O.B. Widlund. A domain decomposition method with Lagrange multipliers and inexact solvers for linear elasticity. *SIAM J. Sci. Comput.*, 22(4): 1199–1219, 2000.

[157] C. Farhat and M. Géradin. On the general solution by a direct method of a large-scale singular system of linear equations: application to the analysis of floating structures. *Int. J. Numer. Methods Eng.*, 41(4):675–696, 1998.

[158] M. James. The generalised inverse. *Math. Gaz.*, 62(420):109, 1978.

[159] G. Strang. The fundamental theorem of linear algebra. *Am. Math. Mon.*, 100(9): 848, 1993.

[160] G. Of and O. Steinbach. The all-floating boundary element tearing and interconnecting method. *J. Numer. Math.*, 17(4):277–298, 2009.

[161] C.M. Augustin, G.A. Holzapfel, and O. Steinbach. Classical and all-floating FETI methods for the simulation of arterial tissues. *Int. J. Numer. Methods Eng.*, 99(4): 290–312, 2014.

[162] G. Golub and W. Kahan. Calculating the singular values and pseudo-inverse of a matrix. *SIAM J. Numer. Anal.*, 2(2):205–224, 1965.

[163] R. Kučera, T. Kozubek, and A. Markopoulos. On large-scale generalized inverses in solving two-by-two block linear systems. *Linear Algebra Appl.*, 438(7):3011–3029, 2013.

[164] O. Steinbach and M. Zank. A stabilized space–time finite element method for the wave equation. In *Lect. Notes Comput. Sci. Eng.*, pages 341–370. Springer, 2019.

[165] M. Siebert and P. Fodor. Newtonian and non-Newtonian blood flow over a backward-facing step – a case study. In *Proceedings of the COMSOL Conference*, 2009.

[166] E. Burman, P. Hansbo, and M.G. Larson. Cut Bogner-Fox-Schmit elements for plates. *Adv. Model. Simul.*, 7(1):27, 2020.

[167] A. Hansbo and P. Hansbo. An unfitted finite element method, based on Nitsche's method, for elliptic interface problems. *Comput. Methods Appl. Mech. Eng.*, 191 (47-48):5537–5552, 2002.

[168] F. Gazzolad. A note on the evolution Navier-Stokes equations with a pressure-dependent viscosity. *Z. Angew. Math. Phys.*, 48(5):760, 1997.

[169] J. Hron, J. Málek, and K.R. Rajagopal. Simple flows of fluids with pressure–dependent viscosities. *Proc. Math. Phys. Eng. Sci.*, 457(2011):1603–1622, 2001.

[170] J.-L. Guermond and L. Quartapelle. A projection FEM for variable density incompressible flows. *J. Comput. Phys.*, 165(1):167–188, 2000.

[171] J.-L. Guermond and A. Salgado. A splitting method for incompressible flows with variable density based on a pressure Poisson equation. *J. Comput. Phys.*, 228(8): 2834–2846, 2009.

Monographic Series TU Graz

Computation in Engineering and Science

Vol. 1 Steffen Alvermann
Effective Viscoelastic Behavior of Cellular Auxetic Materials
2008
ISBN 978-3-902465-92-4

Vol. 2 Sendy Fransiscus Tantono
The Mechanical Behaviour of a Soilbag under Vertical Compression
2008
ISBN 978-3-902465-97-9

Vol. 3 Thomas Rüberg
Non-conforming FEM/BEM Coupling in Time Domain
2008
ISBN 978-3-902465-98-6

Vol. 4 Dimitrios E. Kiousis
Biomechanical and Computational Modeling of Atherosclerotic Arteries
2008
ISBN 978-3-85125-023-7

Vol. 5 Lars Kielhorn
A Time-Domain Symmetric Galerkin BEM for Viscoelastodynamics
2009
ISBN 978-3-85125-042-8

Vol. 6 Gerhard Unger
Analysis of Boundary Element Methods for Laplacian Eigenvalue Problems
2009
ISBN 978-3-85125-081-7

Monographic Series TU Graz

Computation in Engineering and Science

Vol. 7 Gerhard Sommer

Mechanical Properties of Healthy and Diseased Human Arteries
2010
ISBN 978-3-85125-111-1

Vol. 8 Mathias Nenning

Infinite Elements for Elasto- and Poroelastodynamics
2010
ISBN 978-3-85125-130-2

Vol. 9 Thanh Xuan Phan

Boundary Element Methods for Boundary Control Problems
2011
ISBN 978-3-85125-149-4

Vol. 10 Loris Nagler

Simulation of Sound Transmission through Poroelastic Plate-like Structures
2011
ISBN 978-3-85125-153-1

Vol. 11 Markus Windisch

Boundary Element Tearing and Interconnecting Methods for Acoustic and Electromagnetic Scattering
2011
ISBN 978-3-85125-152-4

Vol. 12 Christian Walchshofer

Analysis of the Dynamics at the Base of a Lifted Strongly Buoyant Jet Flame Using Direct Numerical Simulation
2011
ISBN 978-3-85125-185-2

Monographic Series TU Graz

Computation in Engineering and Science

Vol. 13 Matthias Messner

Fast Boundary Element Methods in Acoustics
2012
ISBN 978-3-85125-202-6

Vol. 14 Peter Urthaler

Analysis of Boundary Element Methods for Wave Propagation in Porous Media
2012
ISBN 978-3-85125-216-3

Vol. 15 Peng Li

Boundary Element Method for Wave Propagation in Partially Saturated Poroelastic Continua
2012
ISBN 978-3-85125-236-1

Vol. 16 Andreas Jörg Schriefl

Quantification of Collagen Fiber Morphologies in Human Arterial Walls
2013
ISBN 978-3-85125-238-5

Vol. 17 Thomas S. E. Eriksson

Cardiovascular Mechanics
2013
ISBN 978-3-85125-277-4

Vol. 18 Jianhua Tong

Biomechanics of Abdominal Aortic Aneurysms
2013
ISBN 978-3-85125-279-8

Monographic Series TU Graz

Computation in Engineering and Science

Vol. 19 Jonathan Rohleder

Titchmarsh–Weyl Theory and Inverse Problems for Elliptic Differential Operators
2013
ISBN 978-3-85125-283-5

Vol. 20 Martin Neumüller

Space-Time Methods
2013
ISBN 978-3-85125-290-3

Vol. 21 Michael J. Unterberger

Microstructurally-Motivated Constitutive Modeling of Cross-Linked Filamentous Actin Networks
2013
ISBN 978-3-85125-303-0

Vol. 22 Vladimir Lotoreichik

Singular Values and Trace Formulae for Resolvent Power Differences of Self-Adjoint Elliptic Operators
2013
ISBN 978-3-85125-304-7

Vol. 23 Michael Meßner

A Fast Multipole Galerkin Boundary Element Method for the Transient Heat Equation
2014
ISBN 978-3-85125-350-4

Vol. 24 Lorenz Johannes John

Optimal Boundary Control in Energy Spaces
2014
ISBN 978-3-85125-373-3

Monographic Series TU Graz

Computation in Engineering and Science

Vol. 25 Hannah Weisbecker

Softening and Damage Behavior of Human Arteries
2014
ISBN 978-3-85125-370-2

Vol. 26 Bernhard Kager

Efficient Convolution Quadrature based Boundary Element Formulation for Time-Domain Elastodynamics
2015
ISBN 978-3-85125-382-5

Vol. 27 Christoph M. Augustin

Classical and All-floating FETI Methods with Applications to Biomechanical Models
2015
ISBN 978-3-85125-418-1

Vol. 28 Elias Karabelas

Space-Time Discontinuous Galerkin Methods for Cardiac Electromechanics
2016
ISBN 978-3-85125-461-7

Vol. 29 Thomas Traub

A Kernel Interpolation Based Fast Multipole Method for Elastodynamic Problems
2016
ISBN 978-3-85125-465-5

Vol. 30 Matthias Gsell

Mortar Domain Decomposition Methods for Quasilinear Problems and Applications
2017
ISBN 978-3-85125-522-5

Monographic Series TU Graz

Computation in Engineering and Science

Vol. 31 Christian Kühn

Schrödinger operators and singular infinite rank perturbations
2017
ISBN 978-3-85125-551-5

Vol. 32 Michael H. Gfrerer

Vibro-Acoustic Simulation of Poroelastic Shell Structures
2018
ISBN 978-3-85125-573-7

Vol. 33 Markus Holzmann

Spectral Analysis of Transmission and Boundary Value Problems for Dirac Operators
2018
ISBN 978-3-85125-642-0

Vol. 34 Osman Gültekin

Computational Inelasticity of Fibrous Biological Tissues with a Focus on Viscoelasticity, Damage and Rupture
2019
ISBN 978-3-85125-655-0

Vol. 35 Justyna Anna Niestrawska

Experimental and Computational Analyses of Pathological Soft Tissues – Towards a Better Understanding of the Pathogenesis of AAA
2019
ISBN 978-3-85125-678-9

Monographic Series TU Graz

Computation in Engineering and Science

Vol. 36 Marco Zank

Inf-Sup Stable Space-Time Methods for Time-Dependent Partial Differential Equations
2020
ISBN 978-3-85125-721-2

Vol. 37 Christoph Irrenfried

Convective turbulent near wall heat transfer at high Prandtl numbers
2020
ISBN 978-3-85125-724-3

Vol. 38 Christopher Albert

Hamiltonian Theory of Resonant Transport Regimes in Tokamaks with Perturbed Axisymmetry
2020
ISBN 978-3-85125-746-5

Vol. 39 Daniel Christopher Haspinger

Material Modeling and Simulation of Phenomena at the Nano, Micro and Macro Levels in Fibrous Soft Tissues of the Cardiovascular System
2021
ISBN 978-3-85125-802-8

Vol. 40 Markus Alfons Geith

Percutaneous Coronary Intervention
2021
ISBN 978-3-85125-801-1

Monographic Series TU Graz

Computation in Engineering and Science

Vol. 41 Dominik Pölz

Space-Time Boundary Elements for Retarded Potential Integral Equations
2021
ISBN 978-3-85125-811-0

Vol. 42 Douglas Ramalho Queiroz Pacheco

Stable and stabilised finite element methods for incompressible flows of generalised Newtonian fluids
2021
ISBN 978-3-85125-856-1